Review | Open Access

Energy Z

Qu *et al. Energy Z* **2026**, *2*, 200014 **DOI:**10.20517/energyz.2026.13

Research progress, challenges and opportunities in all-inorganic perovskite photovoltaics

Yangjie Qu[1], Ke Gao[1], Qiliang Zhu[2], Lidong Xing[1], Yihao Cui[1], Jiong Li[3,*], Minghao Liu[1], Haoran Lou[1], Keyou Yan[2,*], Chenghao Duan[1,*]

Keywords:
All-inorganic perovskite, photothermal stability, tandem devices, additive modification, solar cells

Citation: Qu, Y.; Gao, K.; Zhu, Q.; Xing, L.; Cui, Y.; Li, J.; Liu, M.; Lou, H.; Yan, K.; Duan, C. Research progress, challenges and opportunities in all-inorganic perovskite photovoltaics. *Energy Z* **2026**, *2*, 200014. https://dx.doi.org/10.20517/energyz.2026.13

Received: 3 Apr 2026
First Decision: 29 Apr 2026
Revised: 14 May 2026
Accepted: 16 Jun 2026
Published: 2 Jul 2026

Academic Editor:
Yuping Wu
Copy Editor:
Ting-Ting Hu
Production Editor:
Ting-Ting Hu

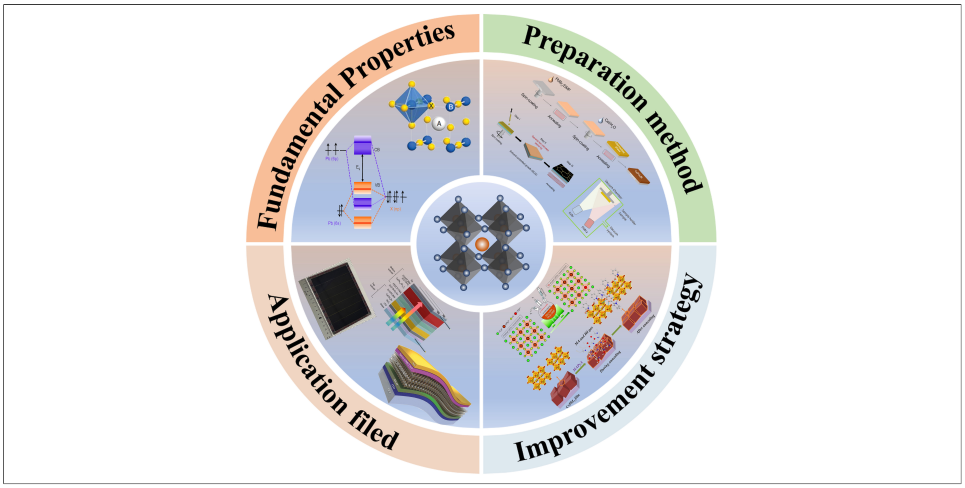

Abstract

The presence of organic components renders organic-inorganic hybrid perovskites highly susceptible to degradation under continuous light irradiation and high-temperature conditions, severely restricting their large-scale practical application in photovoltaic fields. By contrast, all-inorganic perovskites have emerged as highly promising candidate materials for next-generation photovoltaic technologies thanks to their excellent photothermal stability and favorable optoelectronic properties. This review comprehensively summarizes the intrinsic structural characteristics and optoelectronic properties of inorganic perovskites, and details prevalent inorganic perovskite film fabrication routes, including spin-coating, vacuum evaporation deposition, and other methods, alongside their respective advantages and application scenarios. On this basis, it focuses on the latest research progress in performance optimization strategies for

[1]State Key Laboratory of Green Chemical Synthesis and Conversion, College of New Energy and Intelligent Manufacturing, Henan University, Zhengzhou 450000, Henan, China.
[2]School of Environment and Energy, State Key Lab of Luminescent Materials and Devices, Guangdong Provincial Key Laboratory of Solid Wastes Pollution Control and Recycling, South China University of Technology, Guangzhou 510640, Guangdong, China.
[3]School of Material and Chemical Engineering, Zhengzhou University of Light Industry, Zhengzhou 450002, Henan, China.

***Correspondence to:** Prof. Chenghao Duan, State Key Laboratory of Green Chemical Synthesis and Conversion, College of New Energy and Intelligent Manufacturing, Henan University, Zhengzhou 450000, Henan, China. E-mail: chduan2025@henu.edu.cn; Prof. Keyou Yan, School of Environment and Energy, State Key Lab of Luminescent Materials and Devices, Guangdong Provincial Key Laboratory of Solid Wastes Pollution Control and Recycling, South China University of Technology, Guangzhou 510640, Guangdong, China. E-mail: kyyan@scut.edu.cn; Dr. Jiong Li, School of Material and Chemical Engineering, Zhengzhou University of Light Industry, Zhengzhou 450002, Henan, China. E-mail: 2024050@zzuli.edu.cn

inorganic perovskite films through compositional optimization, annealing processing, anti-solvent engineering, post-treatment optimization, and additive modification. Additionally, recent advances and milestones in inorganic perovskites for large-area modules, tandem devices, and flexible perovskite solar cells are reviewed. Finally, it systematically discusses the key bottlenecks hindering the commercialization of inorganic perovskite solar cells and prospects their future development directions and application opportunities.

INTRODUCTION

Perovskite solar cells (PSCs) have witnessed significant breakthroughs, with power conversion efficiency (PCE) soaring from 3.8% in 2009 to 27.3% at present, rapidly closing the efficiency gap with conventional crystalline silicon (c-Si) solar cells[1,2]. The superior photovoltaic properties of perovskite materials, such as a high light absorption coefficient, tunable bandgap, long carrier diffusion length, and low exciton binding energy, are key to achieving high efficiency[3-6]. State-of-the-art high-efficiency PSCs are dominantly constructed from organic-inorganic hybrid perovskites with organic methylammonium (MA^+) and formamidinium (FA^+) cations[7-9]. However, organic components cause the hybrid perovskite to exhibit inherent instability, prone to decomposition and volatilization under continuous illumination and high-temperature operation conditions[10-12]. For instance, the $MAPbI_3$ perovskite undergoes irreversible degradation above 85 °C, a temperature routinely encountered during the practical operation of commercial photovoltaic devices[13]. Meanwhile, $FAPbI_3$ perovskite suffers from severe thermal decomposition at 145 °C[14]. Apart from thermal stress, prolonged light exposure triggers irreversible decomposition and harmful ion migration, thereby accelerating the degradation of hybrid perovskites[15,16]. Such unsatisfactory photothermal stability has become a major obstacle to the commercial development of large-scale PSC modules.

Replacing organic cations with inorganic counterparts (such as Cs^+) yields inorganic perovskite solar cells (IPSCs) with markedly improved photothermal stability, a promising route to enhancing the long-term stability of PSCs[17-19]. More importantly, $CsPbX_3$ perovskites feature a relatively wide bandgap (WBG) ranging from 1.73 to 2.30 eV, enabling corresponding devices to deliver higher open-circuit voltage (V_{oc}) and rendering them ideal top subcell candidates for tandem solar cells (TSCs)[20,21]. Nevertheless, the photoactive black cubic phase $CsPbI_3$ is thermodynamically stable only above 300 °C, and spontaneously transforms into non-photoactive yellow δ-phase below 180 °C[22,23]. Meanwhile, ambient moisture further accelerates this unfavorable phase transition[24].

Two mainstream strategies have been developed to address the intrinsic phase instability of $CsPbI_3$. The first strategy focuses on constructing mixed-halide perovskites via partial I^- substitution with Br^-[25]. This approach moderately mitigates moisture-induced phase separation and suppresses the transformation into δ-phase, thereby improving phase stability[26]. However, the low solubility of Br-containing precursors compromises the uniformity and compactness of perovskite films[27]. Besides, Br^- incorporation significantly widens the bandgap, narrows the light-harvesting spectrum, and reduces device short-circuit current density (J_{sc})[28,29]. The second approach relies on rational additive and solvent engineering to precisely regulate perovskite crystallization kinetics and crystal-phase stability. Extensive research corroborates that introducing specific additives, such as hydrogen lead iodide ($HPbI_3$) or dimethylammonium iodide (DMAI), into perovskite precursor solution enables controlling the crystallization rate and stabilizes photoactive tetragonal (β-phase) and orthorhombic (γ-phase) $CsPbI_3$[30,31]. Other alternative approaches, including metal cation doping and multifunctional interfacial passivation, also efficiently stabilize the black-phase perovskite and achieve excellent photoelectric performance under ambient low-temperature conditions[32-34]. To date, the IPSCs have reached the highest efficiency of 22.49% [Figure 1], lagging far behind hybrid perovskite counterparts[31,35-42].

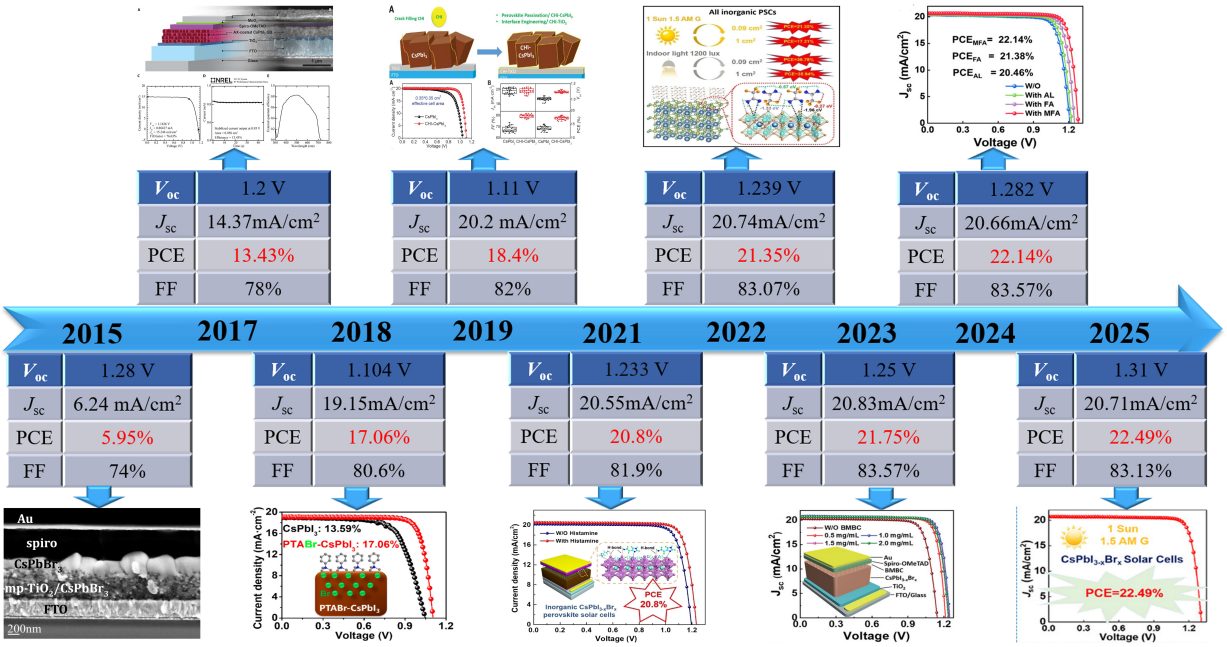

Figure 1. A schematic diagram summarizing the development process of IPSCs. Reproduced with permission. From left to right, this figure is quoted with permission from Ref.[31,35-42], Reprinted from Ref.[35] under the CC BY 4.0 license; Reproduced with permission[36], Copyright © 2017 American Association for the Advancement of Science; Reproduced with permission[37], Copyright © 2018 American Chemical Society; Reproduced with permission[31], Copyright © 2019 American Association for the Advancement of Science; Reproduced with permission[38], Copyright © 2021 Wiley-VCH; Reproduced with permission[39], Copyright © 2023 Wiley-VCH; Reproduced with permission[40], Copyright © 2023 Wiley-VCH; Reproduced with permission[41], Copyright © 2024 Wiley-VCH; Reproduced with permission[42], Copyright © 2025 Wiley-VCH. IPSCs: Inorganic perovskite solar cells; PCE: power conversion efficiency; J_{sc}: short-circuit current density, V_{oc}: open-circuit voltage; FF: fill factor.

This review summarizes recent research progress in IPSC development. We first introduce fundamental crystal structures and photoelectric characteristics of inorganic perovskites, outline available film preparation methods, and evaluate advanced approaches to enhance film quality and crystallinity. Focusing on the controllable fabrication of high-performance inorganic perovskite films, we systematically discuss effective modification strategies and representative applications in compositional optimization, anti-solvent engineering, annealing processing, post-treatment, and additive modification. We further examine the application prospects and developmental potential of IPSCs in large-area modules, TSC, and flexible devices. Furthermore, we systematically analyze the critical bottlenecks currently limiting the performance and commercialization of IPSCs. This review aims to systematically summarize existing achievements, unresolved technical obstacles, and future research orientations, providing theoretical guidance to enhance the competitiveness of IPSCs in the next-generation photovoltaic technologies.

FUNDAMENTAL PROPERTIES OF INORGANIC PEROVSKITES

Crystal structure

Similar to hybrid perovskites, inorganic perovskites follow the general crystal structure formula ABX_3. The monovalent cation A (such as Cs^+) occupies the corner position of the cubic lattice, the divalent metal cation B (such as Pb^{2+}) resides at the unit cell center, and the halide anion X (such as I^-, Br^-) is located at the face centers of the unit cell [Figure 2A]. This orderly arrangement constitutes a corner-sharing octahedral framework with $[BX_6]^{4-}$ as the basic structural unit, thereby yielding a three-dimensional (3D) perovskite crystal structure[43].

The geometric stability and structural feasibility of ABX_3-type perovskites can be quantitatively evaluated using two key parameters: the octahedral factor (μ) and Goldschmidt tolerance factor (t)[44,45]. The ionic radii of A (R_A), B (R_B), and X (R_X) determine μ and t, and the corresponding calculation equations are as follows[46]:

$$t = \frac{(R_A + R_X)}{\sqrt{2}\,(R_B + R_X)} \tag{1}$$

$$\mu = \frac{R_B}{R_X} \tag{2}$$

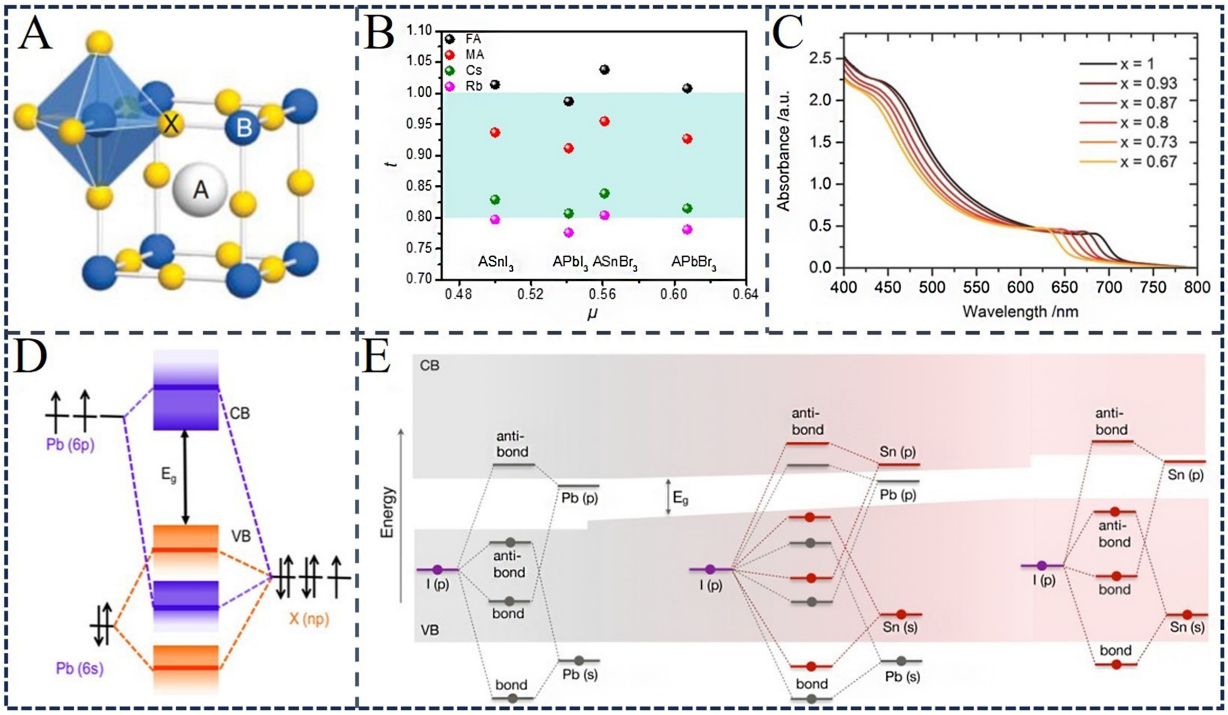

Figure 2. (A) 3D inorganic crystal structure with ABX_3 formula; (B) The calculated *t* and μ factor values for halide perovskites; (C) Optical absorption spectra of $CsPbI_xBr_{3-x}$ at different iodine concentrations. This figure is quoted with permission from Ref.[54], Copyright © 2016 Wiley-VCH; (D) The schematic diagram of bonding and antibonding orbitals in $APbX_3$ illustrates the formation of the valence band and conduction band. This figure is quoted with permission from Ref.[57], Copyright © 2016 American Chemical Society; (E) Schematic diagram of bandgap bowing effect in $CsPb_{1-x}Sn_xI_3$. The shaded area represents the valence band and conduction band, while the thick lines illustrate the molecular orbital picture of the electronic energy bands in the Sn-Pb alloy. This figure is quoted with permission from Ref.[60], Copyright © 2018 American Chemical Society.

Studies have demonstrated that a stable 3D cubic perovskite structure requires strict geometric criteria[47,48]: the *t* should lie between 0.8 and 1.0, and the μ between 0.4 and 0.9. If $t < 0.8$, the $[BX_6]^{4-}$ octahedron becomes distorted and the cubic structure collapses. When *t* 1.0, the crystal will transform into a hexagonal crystal system. For the μ parameter, values below 0.4 prevent the formation of stable octahedral units[47]. Since both parameters must be satisfied simultaneously, only limited cation-halide combinations yield a stable 3D cubic perovskite [Figure 2B]. As illustrated in Figure 2B, the instability of the black phase $CsPbI_3$ arises because its *t* value lies marginally outside the stable window. The relatively small Cs^+ cation inadequately supports the $[PbI_6]^{4-}$ octahedral framework, causing severe lattice distortion and thermodynamic instability[48].

To overcome this critical stability issue, introducing Br^- with smaller ionic radii to partially replace I^- in $CsPbI_3$ can precisely tune *t* and μ into the favorable stable range, thereby stabilizing the $[PbI_6]^{4-}$ octahedral framework[49]. Notably, although $CsPbI_{3-x}Br_x$ can retain the photoactive perovskite phase at room temperature, it remains prone to non-perovskite phase transformation in humid environments[50]. In parallel, additive engineering effectively suppresses phase transitions and stabilizes the cubic phase over the long term by precisely modulating the distortion degree of the $[PbI_6]^{4-}$ octahedron. Furthermore, introducing a small amount of Sn^{2+} to replace Pb^{2+} can also effectively stabilize the black phase $CsPbI_3$ and inhibit its

transformation to the inactive yellow phase[51]. However, excessive Sn^{2+} doping (content > 40%) degrades material stability due to the susceptibility of Sn^{2+} to oxidation into Sn^{4+}, accompanied by lattice mismatch and phase separation[52].

From crystallographic and microscopic mechanistic analyses, the lattice constant (LC) of $CsPbI_{3-x}Br_x$ decreases monotonically with increasing Br^- content[43,53]. This trend stems from the variation in the average Pb–X bond length. Given the smaller ionic radius of Br^- (1.82 Å) relative to I^- (2.06 Å), the Pb–Br bond (3.04-3.16 Å) is inherently shorter than the Pb–I bond (3.19-3.25 Å) within the $[PbI_{6-x}Br_x]^{4-}$ octahedron. The reduction in LC suppresses intracrystalline structural relaxation and increases the formation energy of secondary phases, thereby strengthening material stability. From a thermodynamic perspective, the $CsPbI_{3-x}Br_x$ system exhibits a negative formation enthalpy, confirming its intrinsic thermodynamic stability[43]. This feature arises from strong Coulombic interactions within the perovskite lattice. Br^- substitution for I^- generates shorter and stronger Pb–Br bonds, which substantially enhance electrostatic interactions between halide and metal cations in the $[PbX_6]^{4-}$ framework[53]. Accordingly, Br^- doping represents an effective dual strategy for simultaneously improving the structural and thermodynamic stability of $CsPbI_{3-x}Br_x$ perovskites.

Electronic properties

Beyond crystal structure, $CsPbI_{3-x}Br_x$ perovskites exhibit distinctive electronic properties. With increasing Br^- doping, the bandgap of $CsPbI_{3-x}Br_x$ increases monotonically, accompanied by a pronounced blueshift of the optical absorption edge [Figure 2C][54,55]. This tunable bandgap behavior arises from differences in halogen electronegativity. In the $CsPbI_3$ lattice, the electronic structure is governed by Coulombic interactions within Pb–I bonds and between adjacent iodide ions. Partial substitution of I^- by the more electronegative Br^- triggers directional charge transfer between halide anions and Pb cations, which modulates overall Coulomb energy, electronic transport characteristics, and bandgap[56].

From the perspective of orbital contributions, the band structure of $CsPbI_{3-x}Br_x$ follows a well-defined compositional dependence [Figure 2D][57]. Cs^+ exerts only a weak influence on the valence and conduction band electron distributions, and thus plays a limited role in bandgap modulation. Its primary function is to serve as a charge-compensating center that maintains lattice charge neutrality and structural stability. In both $CsPbI_3$ and $CsPbBr_3$, the conduction band minimum (CBM) is dominated by Pb 6*p* orbitals, with negligible contributions from halide *s* orbitals[53]. The valence band maximum (VBM) originates from strong hybridization between Pb 6*s* and halide *p* orbitals (I 5*p* for $CsPbI_3$, Br 4*p* for $CsPbBr_3$). This hybridization scheme is preserved in mixed-halide systems but exhibits a notable compositional substitution effect. With increasing Br content, the I 5*p* orbital contribution to the VBM is gradually replaced by Br 4*p* orbitals, and the halide s orbital contribution to the CBM is similarly substituted, ultimately leading to the movement of the CBM energy level towards higher energy states. This mechanism confirms that B–X bonds serve as the core structural unit governing the perovskite band-edge structure of perovskite. Such orbital hybridization enhances electronic coupling between B-site metals and halides, facilitates *p*-*p* optical transitions, and ultimately determines the Fermi level and bandgap magnitude.

Accordingly, partial replacement of Pb^{2+} with Sn^{2+} also enables effective bandgap modulation in inorganic perovskites. Unlike Br doping, the bandgap of inorganic perovskites first decreases and then increases as Sn^{2+} content increases. This is mainly due to the bowing effect of the bandgap[58,59]. As shown in Figure 2E, the band edge binding of pure $CsSnI_3$ is weaker than that of pure $CsPbI_3$, resulting in a difference in the absolute band edge position (band offset). This is mainly because the binding energy of Sn *s* and *p* atomic orbitals is weaker than the corresponding Pb states. The VBM of $CsPb_{1-x}Sn_xI_3$ comes from the interaction of Sn *s* and I *p* orbitals, while the CBM comes from Pb *p* and I *p* orbitals[60,61]. Therefore, the bandgap of $CsPb_{1-x}Sn_xI_3$ is smaller than that of pure $CsSnI_3$ and $CsPbI_3$. Beyond this dominant chemical effect, lattice strain also

imposes a minor impact. Variations in alloy composition alter the LC and induce local lattice relaxation, which further shifts the band-edge positions[62]. However, to fully elucidate the photoelectric properties of perovskite materials at the atomic scale, further comprehensive studies that combine theoretical calculations and experimental characterizations of their electronic structures are still needed.

Optical properties

Efficient photon capture capability is a core prerequisite for the industrial application of perovskite materials in photovoltaics. The optical absorption coefficient and refractive index are two key indicators that characterize their optical properties. Although quantitative experimental data on the absorption coefficients of inorganic perovskites remain limited, existing quantum-efficiency measurements and active-layer thicknesses in high-performance IPSCs indicate values that are comparable to those of hybrid perovskites. Inorganic perovskite materials exhibit an absorption coefficient peak exceeding 10^4 cm^{-1} above the bandgap energy[63]. This strong absorption enables ultrathin absorbing layers (≤ 1 μm) to maintain exceptional photon-harvesting efficiency, supporting the development of lightweight and flexible device architectures[64,65]. Additionally, the optical absorption performance of inorganic perovskites can be further optimized through elemental doping strategies. For example, In-doped inorganic perovskites exhibit improved light absorption in the wavelength range of 400 to 700 nm, thereby boosting the photoelectric performance of the corresponding devices[66,67]. Singh *et al.* further confirmed that inorganic perovskites can achieve full coverage of the visible spectrum via precise bandgap modulation, making them promising candidates for light-absorbing layers[68].

Beyond the absorption coefficient, the refractive index $n(\omega)$ is another fundamental parameter characterizing the optical properties of the inorganic perovskite. Researchers have found that the refractive index of perovskite reaches 2.46 at 435 nm, a feature that effectively reduces front-surface reflection loss of the active layer[68]. Therefore, inorganic perovskites are suitable as an effective anti-reflection coating for TSCs. Notably, the refractive index $n(\omega)$ of $CsPbI_{3-x}Br_x$ shows a clear correlation with Br^- doping content. This phenomenon originates from changes in crystal dielectric properties driven by variations in halide ionic radii[69].

PREPARATION METHODS OF INORGANIC PEROVSKITE FILMS

The preparation of a perovskite layer with high crystallinity, large grain size, uniform and compact morphology is a key prerequisite for fabricating high-performance devices. The properties of inorganic perovskite films are strongly dependent on their preparation methods. Currently, several promising preparation techniques, such as spin-coating, vacuum evaporation deposition, spray-assisted deposition, hot-air-assisted deposition, and slot-die coating, have been employed to deposit inorganic perovskite films[70-80].

Spin-coating method

Solution processing represents the mainstream technical route for scalable fabrication of PSCs. Featuring low cost, high efficiency, excellent compatibility with large-area coating and roll-to-roll (R2R) manufacturing, this method is highly amenable to industrial implementation. At the laboratory scale, spin-coating remains the dominant method for depositing inorganic perovskite films, which can be divided into one- and two-step processes[81-83]. The one-step spin-coating method enables efficient and convenient preparation of $CsPbI_{3-x}Br_x$ films owing to its simple operation and minimal equipment requirements. Typically, CsX and PbX_2 precursors are dissolved in dimethyl sulfoxide (DMSO), deposited via spin-coating, and subsequently annealed at elevated temperatures to eliminate residual solvent and promote crystallization [Figure 3A][19,84]. Given the distinct differences in solubility and crystallization kinetics among $CsPbX_3$ series precursors, rational solvent engineering is indispensable. For instance, $CsPbI_3$ can be fabricated using dimethylformamide (DMF), whereas $CsPbI_2Br$ requires high-boiling-point solvents such as DMSO to achieve high-quality films via the one-step deposition[71,81].

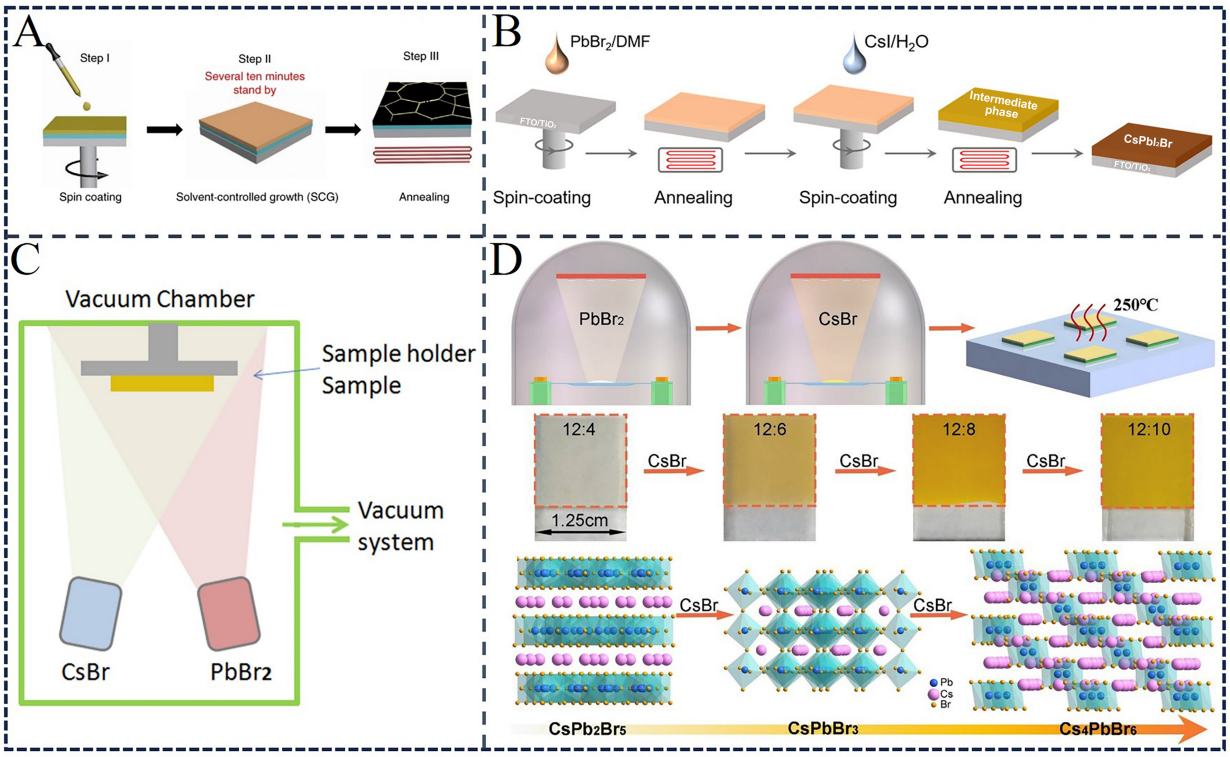

Figure 3. The preparation method of inorganic perovskite films. (A) One-step spin-coating method. Reprinted from Ref.[19] under the CC BY 4.0 license; (B) Two-step spin-coating method. This figure is quoted with permission from Ref.[87], Copyright © 2022 Wiley-VCH; (C) Schematic illustration of vacuum dual-source thermal co-evaporation to deposit $CsPbBr_3$ films. This figure is quoted with permission from Ref.[74], Copyright © 2018 Elsevier; (D) Sequential evaporation technique to prepare $CsPbBr_3$ perovskites. This figure is quoted with permission from Ref.[95]; Copyright © 2019 Elsevier.

Unlike $CsPbI_3$, Br-rich perovskites, including $CsPbIBr_2$ and $CsPbBr_3$, suffer from limitations arising from the poor solubility and weak coordination capacity of CsBr and $PbBr_2$ precursors[85,86]. Consequently, high-quality films of these compositions are mostly prepared via two-step deposition. As illustrated in Figure 3B, the two-step process involves first spin-coating a Pb-based precursor (such as $PbBr_2$, PbI_2) onto the substrate, and thermal annealing to form a dense PbX_2 template layer. In the subsequent step, a Cs-containing precursor solution (such as CsI, CsBr) is cast onto the PbX_2 film, followed by a second annealing step to complete the conversion to perovskite[87]. The morphology and crystallinity of the intermediate PbX_2 layer directly determine the quality of the final perovskite film. Meanwhile, the low solubility of CsBr and uncontrolled crystallization easily induce undesirable secondary phases, including Pb-rich $CsPb_2Br_5$ and Cs-rich Cs_4PbBr_6, which severely degrade device performance[63].

Vacuum evaporation deposition

Due to the low solubility of inorganic Cs salts (such as CsBr and CsI), traditional solution processing methods often yield inorganic perovskite films with poor morphology, incomplete surface coverage, and high surface defect density. To address these limitations, evaporation-based deposition techniques have been widely adopted to prepare inorganic perovskite films with diverse elemental compositions.

Vacuum evaporation deposition is typically performed under solvent-free vacuum conditions and serves as an effective strategy for depositing poorly soluble materials. Figure 3C presents a schematic diagram of the evaporation process employing multiple evaporation sources[74]. Among various vacuum deposition methods, the dual-source co-evaporation is the most widely used configuration, in which inorganic precursors CsX and PbX_2 evaporate simultaneously from two independent sources. A set of key experimental

parameters strongly govern the resulting film quality, including the precursor evaporation rate, substrate temperature, as well as annealing duration and temperature[88-90]. The stoichiometry of inorganic perovskite films is primarily controlled by regulating the precursor deposition rate, enabling precise tuning of the elemental composition and thickness of the perovskite layer[91].

Additionally, single- and triple-source vacuum deposition systems have also been developed. For instance, Li *et al*. prepared $CsPbBr_3$ films via vacuum deposition by mixing CsBr and $PbBr_2$ precursors in a single evaporation source[92]. Nevertheless, the significant difference in melting points between $PbBr_2$ and CsBr makes it challenging to accurately control their molar ratio on the substrate[93]. He *et al.* introduced a third inorganic precursor source (CsCl) into a conventional dual-source co-evaporation system, enabling flexible modulation of Cs-Pb-Br-Cl compositions. This triple-source strategy facilitates the formation of the 0D $Cs_4Pb(Br/Cl)_6$ phase, which effectively passivates defects and suppresses non-radiative recombination[94].

A sequential vacuum evaporation deposition method has also been developed to fabricate $CsPbBr_3$ films with improved morphology and reduced defect density[95]. In this approach, $PbBr_2$ is first evaporated onto the substrate, followed by successive deposition of CsBr films with varying thickness ratios. Adjusting this thickness ratio triggers phase evolution from Pb-rich $CsPb_2Br_5$ to stoichiometric $CsPbBr_3$, and eventually to Cs-rich Cs_4PbBr_6 [Figure 3D]. The optimized $CsPbBr_3$ films exhibit a compact and uniform morphology featuring large grains and a vertically oriented monolayer structure. This favorable microstructure originates from the homogeneous reaction between CsBr and $PbBr_2$ during deposition. Besides $CsPbI_{3-x}Br_x$ perovskites, vacuum evaporation is also applicable to other inorganic perovskite systems. It is well documented that Sn^{2+} is chemically unstable under ambient conditions and prone to oxidation into Sn^{4+}. Vacuum evaporation provides an effective approach for preparing Sn-based inorganic perovskites because its ultrahigh vacuum environment effectively inhibits oxidation. Abbasli *et al.* verified that vacuum deposition can well preserve Sn^{2+} valence states during the growth of Sn-based perovskite films[96].

Compared with solution processing, evaporation deposition technology possesses distinct merits, including excellent film uniformity, complete removal of residual organic solvents, and high reproducibility. In particular, it can produce inorganic perovskite films with superior morphology and full surface coverage, which is conducive to enhancing device performance[97,98]. However, this technique still has inherent drawbacks, such as complicated operation, high costs, and long processing time, restricting the large-scale commercial deployment of vacuum evaporation[99,100].

Other methods

In addition, several alternative techniques for fabricating inorganic perovskite films have been developed to overcome the limitations of spin-coating and vacuum evaporation deposition methods. Mist deposition has been demonstrated to produce fully covered $CsPbBr_3$ films, as shown in Figure 4A. During deposition, tiny and uniform droplets impinge on the substrate, where rapid solvent evaporation triggers instantaneous nucleation. Subsequent droplet attachment to pre-formed crystals drives continuous grain growth, ultimately forming a fully covered and dense film[101].

Vapor-assisted deposition integrates spin-coating (first step) with thermal vacuum deposition (second step), endowing the process with precise control and excellent reproducibility [Figure 4B]. Liu *et al.* employed this method to fabricate $CsPbIBr_2$ films with high phase purity and large grain sizes. The resultant IPSCs achieved a V_{oc} of up to 1.289 V, which is attributed to reduced charge recombination[102]. This technique has also been applied to fabricate $CsPbBr_3$ perovskite films. Precise modulation of the CsBr deposition thickness in the secondary vacuum step allows accurate regulation of the phase evolution from $CsPb_2Br_5$ to $CsPbBr_3$ and further to Cs_4PbBr_6, yielding high-quality $CsPbBr_3$ films[103].

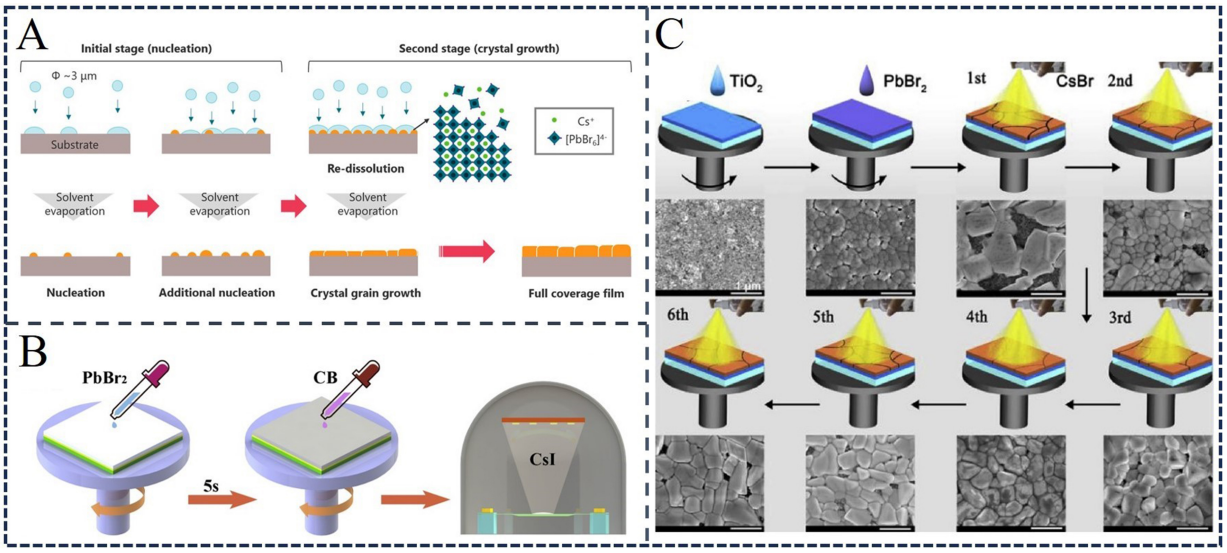

Figure 4. (A) Schematic diagram of the fabrication of $CsPbBr_3$ film by the mist deposition method. This figure is quoted with permission from Ref.[101], Copyright © 2020 American Chemical Society; (B) Schematic diagram of the vapor-assisted deposition of $CsPbIBr_2$ film. This figure is quoted with permission from Ref.[102], Copyright © 2020 Elsevier; (C) Schematic diagram of Spray-assisted preparation of inorganic perovskite, along with top-view scanning electron microscope images of different films. This figure is quoted with permission from Ref.[104], Copyright © 2018 Elsevier.

Spray-assisted deposition has also been reported for $CsPbBr_3$ film preparation. First, a $PbBr_2$ layer is spin-coated, followed by CsBr deposition on $PbBr_2$ through repeated spray cycles [Figure 4C]. Optimizing the number of CsBr spray cycles enables the complete phase transformation from $PbBr_2$-rich $CsPb_2Br_5$ to $CsPbBr_3$ and further to Cs_4PbBr_6. The obtained $CsPbBr_3$ films exhibit high phase purity and fewer grain boundaries, which facilitate efficient hole extraction and enhance device performance[104].

IMPROVE THE QUALITY OF INORGANIC PEROVSKITE FILMS

The quality of inorganic perovskite films directly determines the performance of the corresponding photovoltaic devices. The precursor composition, solvent species, additive engineering, and annealing process greatly influence the quality of the inorganic perovskite films.

Precursor components

X-site doping

$CsPbI_3$ is recognized as one of the most promising candidates among inorganic perovskite series, owing to its favorable bandgap of approximately 1.73 eV[36,81]. However, its photoactive phase readily converts to the yellow δ-phase at room temperature. Such phase instability severely limits the long-term operational stability of $CsPbI_3$-based IPSCs under ambient conditions. To address this challenge, partial substitution of I^- with Br^- ($CsPbI_{3-x}Br_x$) has been verified as an effective strategy[49,50]. Notably, Br^- doping also lowers the phase transition temperature from the β-phase to the cubic phase, a significant advantage for practical applications. Nasstrom *et al.* prepared a series of $CsPbI_{3-x}Br_x$ perovskites via inkjet printing. The research results show that replacing the larger I^- with the smaller Br^- reduces the formation temperature of the α-phase perovskite and inhibits the octahedral distortion during the cooling process. With increasing Br^- content, the required crystallization temperature drops sharply from above 300 °C for $CsPbI_3$ to 230 °C for $CsPbI_2Br$ and 160 °C for $CsPbIBr_2$[105]. Reduced phase transition temperatures endow the inorganic perovskite phase with superior thermodynamic stability at room temperature, thereby fundamentally enhances the environmental stability of the $CsPbI_{3-x}Br_x$ perovskite.

Introducing Cl^- into the $CsPbI_{3-x}Br_x$ perovskite lattice can markedly improve crystallinity and crystallographic orientation, thereby mitigating defect-related trap states. The structural improvements effectively prolong the charge carrier lifetime, inhibit non-radiative recombination, and ultimately enhance the photovoltaic performance of the perovskite film. Ye *et al.* improved the crystallinity of $CsPbI_{3-x}Br_x$ perovskite films and inhibited charge recombination by adding a small amount of $PbCl_2$ into the precursor solution[106]. Meanwhile, the $PbCl_2$ additive can enhance the phase stability of $CsPbI_{3-x}Br_x$ perovskite. When stored in ambient air (40% relative humidity) for 120 h, the film with $PbCl_2$ retained the black phase, whereas the control film degraded within 24 h. Consequently, the optimized $CsPbI_{3-x}Br_x$ IPSCs exhibited excellent performance, with a V_{oc} of up to 1.25 V and an efficiency of 18.64%[106].

Apart from halide doping, non-halide and pseudohalide anions such as acetate ions (Ac^-) and SCN^- have emerged as effective regulators of $CsPbX_3$ crystal structure and phase stability[107]. Strong coordination between Pb^{2+} and these anions optimizes perovskite crystallinity and photoelectric properties, thereby improving the corresponding device performance. Zhao *et al.* reported that partial substitution of I^- with Ac^- modifies the morphology, electronic properties, and band structure of $CsPbI_2Br$ films[108]. Compared with the pristine $CsPbI_2Br$ film, the $CsPbI_{2-x}Br(Ac)_x$ film exhibits a porous and nanoparticle-rich surface morphology, which favors α-phase stabilization and accelerates charge separation and extraction[108]. Meanwhile, Ac^- doping gives rise to structural distortion that diminishes Pb–X orbital overlap, broadens the bandgap and modulates the electronic structure. Interestingly, the $CsPbI_{2-x}Br(Ac)_x$ IPSCs achieved an efficiency of 15.56% and a V_{oc} of 1.30 V without compromising the photocurrent density[108].

Similarly, SCN^- doping exhibits comparable structural modulation capability, which arises from the strong Pb–N and Pb–S interactions within the perovskite lattice. Lou *et al.* further demonstrated that SCN^- incorporation introduces lattice disorder in inorganic $CsPbBr_3$ nanocrystals, leading to lattice expansion and bandgap increase[109]. Zhang *et al.* demonstrated that the incorporation of SCN^- into mixed halide perovskites promotes crystallization and reduces grain boundaries[110]. Furthermore, a small amount of SCN^- can occupy iodine vacancies in the perovskite lattice. The resulting steric hindrance restricts halide ion migration, thus boosting structural integrity and device operational durability[110].

A-site doping

In the $CsPbX_3$ perovskite structure, the ionic radius of Cs^+ is relatively small, lying at the lower limit for maintaining a stable cubic phase. This inherent structural characteristic triggers lattice distortion and compromises phase stability. Although smaller cations (such as Rb^+) are usually considered to exacerbate lattice deformation, experimental results confirm that the partial substitution of Cs^+ with Rb^+ effectively improves phase stability[111]. Such unexpected stability enhancement stems from stronger electrostatic coupling between small Rb^+ and the halide framework. The resulting slight reduction in the Pb–X–Pb bond angle facilitates the formation of a more compact and lower-energy lattice configuration, inherently impeding the transition toward undesirable non-perovskite phases[111].

Apart from Rb^+, incorporation of other small-radius alkali metal ions, including Li^+, Na^+, and K^+, also causes lattice contraction and reinforces bonding interactions within the $[PbX_6]^{4-}$ octahedral framework, significantly improving the phase stability of inorganic perovskites at room temperature[112]. Park and colleagues introduced K^+ as a partial substitute for Cs^+ in the $CsPbI_2Br$ lattice. By optimizing the doping concentration, the $Cs_{0.925}K_{0.075}PbI_2Br$ IPSCs yielded a champion PCE of 10.0% and exhibited prolonged operational stability under ambient conditions[112]. Notably, alkali metal cation doping effectively regulates the crystallization kinetics of perovskite films, raising the energy barrier for homogeneous nucleation while lowering the barrier for ion attachment onto existing grain surfaces.

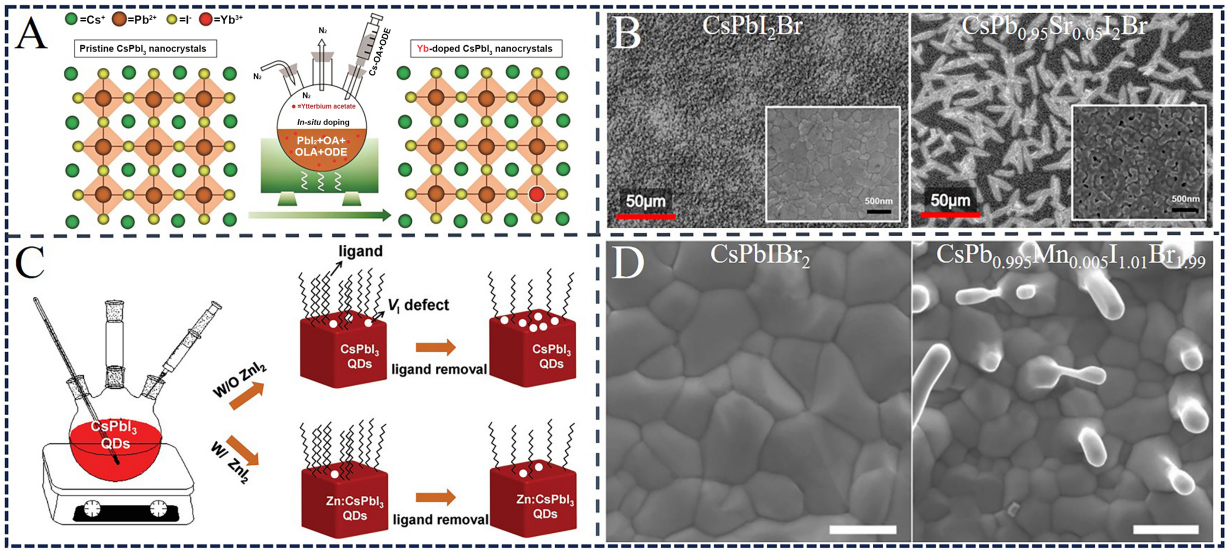

Figure 5. (A) Schematic diagram of *in situ* Yb-doped preparation of $CsPbI_3$ QDs. This figure is quoted with permission from Ref.[114], Copyright © 2020 The Royal Society of Chemistry; (B) SEM images of $CsPbI_2Br$ and $CsPb_{0.95}Sr_{0.05}I_2Br$ film. This figure is quoted with permission from Ref.[119], Copyright © 2017 American Chemical Society; (C) Schematic illustration of iodine defect state control of $CsPbI_3$ QDs by ZnI_2. This figure is quoted with permission from Ref.[124], Copyright © 2020 Wiley-VCH; (D) The SEM images of $CsPbIBr_2$ and $CsPb_{0.995}Mn_{0.005}I_{1.01}Br_{1.99}$ films. All the scale bars are 1 μm. This figure is quoted with permission from Ref.[125], Copyright © 2018 Wiley-VCH. QDs: Quantum dots; SEM: scanning electron microscopy.

B-site doping

In perovskite lattices, the B-site is primarily occupied by Pb^{2+}. Substitution of Pb^{2+} with smaller metal ions can increase the *t* and enhance structural stability. Meanwhile, dopant ions must maintain the μ within an optimal window to preserve the intact corner-sharing $[BX_6]^{4-}$ octahedral network. To date, various metal ions (including divalent, multivalent, and rare-earth metals) have been successfully applied for B-site substitution[113].

Lanthanide element doping has been widely validated as an effective approach to stabilize inorganic perovskite lattices. Shi *et al.* reported that incorporating Yb^{3+} with a smaller ionic radius can increase the *t* factor of the inorganic perovskite lattice, thereby enhancing the structural stability [Figure 5A]. In addition, Yb^{3+} can effectively reduce defects and trap states derived from surface and lattice vacancies, which helps to improve the photoluminescence quantum yield, material crystallinity, thermal stability, and carrier transport of $CsPbI_3$ quantum dots (QDs). Consequently, the device based on optimally Yb-doped $CsPbI_3$ QD achieved an efficiency of 13.12% and exhibited significantly improved storage stability under ambient conditions[114]. Similarly, Eu^{2+} doping enhances the long-term stability of $CsPbBr_3$ IPSCs because the LC of the perovskite crystal gradually decreases with increasing Eu^{2+} content, resulting in lattice contraction. Eu^{2+} substitution also promotes ordered crystal growth and reduces defect density, leading to smoother perovskite film morphology[115]. Compared with the control device, the Eu-doped devices showed improved efficiency owing to extended carrier lifetime and the inhibition of charge recombination[115].

Alkaline earth metal cations (Mg^{2+}, Ca^{2+}, Sr^{2+}, and Ba^{2+}) have also been incorporated into $CsPbX_3$ films to modulate crystallization and energy level structure[116]. The ionic radius difference between Pb^{2+} (1.190 Å) and these divalent cations (such as Mg^{2+}: 0.720 Å, Ca^{2+}: 1.000 Å, Sr^{2+}: 1.118 Å, Ba^{2+}: 1.350 Å) induces lattice strain, resulting in either lattice contraction or expansion depending on the dopant type. Ba^{2+} doping boosted the efficiencies of $CsPbIBr_2$ and $CsPbI_2Br$ devices to 10.51% and 14.85%, respectively, outperforming the pristine counterparts (8.4% and 12.43%). These improvements stemmed from optimized lattice structure and reduced

defect density in the doped perovskite films[78]. Likewise, optimizing Ca^{2+} content enabled a champion $CsPbI_3$ device with a PCE of 13.5%, and the encapsulated Ca-doped device exhibited superior ambient stability compared with the control sample. Nevertheless, excessive Ca^{2+} incorporation widens the bandgap and induces surface segregation during crystallization. The formed CaO layer effectively passivates surface defects, yet an overly thick layer will impede charge transport[117]. Comparable phenomena are also observed in Sr-doped $CsPbI_2Br$ films. Sr^{2+} tends to accumulate at the film surface, forming a thin SrO layer that diminishes the surface defect density[118]. As observed in the scanning electron microscopy (SEM) image [Figure 5B], Sr^{2+} doping generates distinctive snowflake-like microstructures, whose density increases with rising Sr^{2+} concentration. Meanwhile, X-ray diffraction patterns revealed that the bare $CsPbI_3$ film degrades rapidly under ambient exposure, whereas no diffraction peaks corresponding to degraded phases are detected in the Sr-doped film. By tuning the Sr^{2+} doping concentration, the $CsPb_{0.98}Sr_{0.02}I_2Br$ device delivered a PCE of 11.3%, far exceeding the 6.6% of the undoped device[119].

As a congener of Pb, substitution of Pb^{2+} with Sn^{2+} in inorganic perovskites is a promising strategy to reduce material toxicity, modulate bandgap, and enhance light-harvesting capability. Given the comparable ionic radii and analogous chemical properties between Sn^{2+} and Pb^{2+}, this substitution causes negligible lattice distortion, ensuring structural compatibility. Low-concentration Sn^{2+} doping can also increase carrier mobility, reduce defect density, and stabilize the photoactive perovskite phase[120,121]. For instance, $CsPb_{0.9}Sn_{0.1}IBr_2$ IPSC achieved a PCE of 11.33%, which is substantially higher than the 8.25% of the pristine $CsPbIBr_2$ device[122]. In addition, Sn-doped IPSCs exhibited excellent long-term stability and heat/moisture resistance[122]. In contrast, high-concentration Sn^{2+} doping tends to accelerate the crystallization rate of inorganic perovskites and aggravates Sn^{2+} oxidation, ultimately degrading device efficiency[20].

Other divalent transition metal ions with smaller ionic radii (Mn^{2+}, Ni^{2+}, Cu^{2+}, and Zn^{2+}) can also induce perovskite lattice contraction, which in turn enhances phase stability and boosts the formation energy[123]. Zhang *et al.* successfully synthesized Zn-doped $CsPbI_3$ QDs using ZnI_2 as the dopant to provide both Zn^{2+} and I^-. The Zn^{2+} increases the formation energy and *t* of the QDs, thereby reinforcing lattice stability. Meanwhile, the I^- from the ZnI_2 inhibits the formation of iodine vacancy defects during the $CsPbI_3$ film preparation process, effectively suppressing the charge recombination [Figure 5C]. The Zn-doped $CsPb_{0.9}Zn_{0.1}I_3$ QD devices achieved an outstanding efficiency of 16.07%, remarkably outperforming the 13.98% efficiency of the control device[124]. Liang *et al.* synthesized $CsPb_{1-x}Mn_xI_{1+2x}Br_{2-2x}$ perovskite at room temperature with MnI_2 as the dopant. As Mn^{2+} concentration increases, the bandgap of $CsPb_{1-x}Mn_xI_{1+2x}Br_{2-2x}$ decreases from 1.89 to 1.75 eV. Mn^{2+} doping also induces vertical branched structures on the perovskite surface. Such morphology enlarges the contact area between the perovskite and the carbon electrode, promoting electron transfer across the interface [Figure 5D]. Therefore, Mn-doped IPSC delivers improved photoelectric performance and excellent stability[125].

Solvent components

Solvent engineering of precursor solutions is a core strategy for fabricating inorganic $CsPbI_{3-x}Br_x$ perovskite films, as it directly controls precursor solubility, thin-film growth dynamics, and final photovoltaic performance. Rational solvent selection plays an indispensable role in enhancing the solubility of inorganic perovskite precursors[126-128]. Featuring high polarity and strong coordination with metal cations, DMSO is commonly blended with DMF as a cosolvent to selectively improve the solubility of Br-containing precursors. Using this strategy, the solubility of $CsPbI_2Br$ can reach 1.2 M, thereby producing films with a thickness exceeding 500 nm[129].

Nevertheless, DMSO content exceeding 40% triggers adverse effects, such as reduced grain size and pinhole formation across the perovskite layer. These defects originate from the strong coordination between DMSO and Pb^{2+}, which slows down crystallization kinetics and disturbs homogeneous grain evolution, underscoring

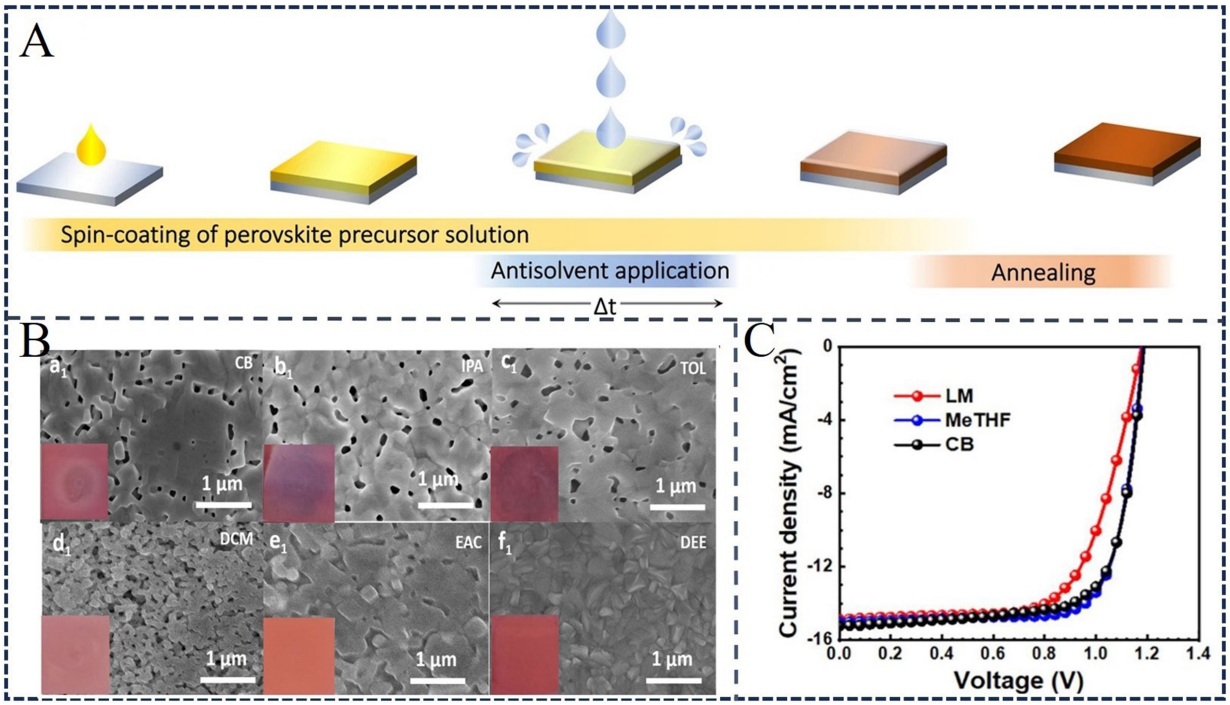

Figure 6. (A) A schematic diagram of the process for preparing the perovskite layer by adding the anti-solvent. Reprinted from Ref.[132] under the CC BY 4.0 license; (B) SEM images of the $CsPbIBr_2$ films with different antisolvents: (b1) CB; (b2) IPA; (b3) TOL; (b4) DCM; (b5) EAC; and (b6) DEE. This figure is quoted with permission from Ref.[139], Copyright © 2019 American Chemical Society; (C) *J-V* curves of the devices with different antisolvents. This figure is quoted with permission from Ref.[140], Copyright © 2021 Elsevier. CB: Chlorobenzene; DCM: dichloromethane; DEE: diethyl ether; EAC: ethyl acetate; IPA: isopropyl alcohol; SEM: scanning electron microscopy; TOL: toluene; LM: (R)-(+)-limonene; MeTHF: 2-methyltetrahydrofuran.

the necessity of optimizing solvent ratios. The one-step deposition of $CsPbI_{3-x}Br_x$ films is highly susceptible to solvent evaporation behavior. In particular, precursor solutions containing DMSO feature slow crystallization, frequently resulting in non-uniform films. To overcome this limitation, incorporating low-boiling-point alcohols to form DMSO-alcohol cosolvent mixtures has proven effective for accelerating solvent removal and regulating crystallization behavior. Wang *et al.* used low-boiling-point alcohols to form an azeotropic DMSO-alcohol mixture with a low boiling point, which can volatilize rapidly and thoroughly, thereby accelerating the crystallization of the $CsPbIBr_2$ film. By conducting thermal treatment at the optimal temperature, high-quality $CsPbIBr_2$ films with pinhole-free morphology, high crystallinity, large grain size, and preferred crystal orientation were successfully prepared using the DMSO-methanol system. The obtained IPSCs exhibited excellent long-term stability and a PCE of up to 11.49%[130].

Anti-solvent engineering

Anti-solvents are indispensable for the solution-based fabrication of inorganic perovskite films by promoting heterogeneous nucleation. Their working principle involves facilitating rapid supersaturation during the spin-coating process, thereby expediting perovskite crystal nucleation[131]. This phenomenon arises from the decreased solubility of perovskite precursors upon anti-solvent addition, coupled with the rapid removal of the primary solvent from the precursor solution. Several critical parameters govern the quality of as-prepared perovskite films, such as anti-solvent type, dosage, dripping timing, and dripping rate. A schematic of the anti-solvent treatment process during perovskite film fabrication is shown in Figure 6A[132]. An ideal anti-solvent should possess good miscibility with the primary processing solvent to enable effective solvent removal, yet remain chemically inert toward perovskite precursors so that the perovskite lattice remains intact.

Since Jeon *et al.* first employed toluene (TOL) as an anti-solvent for perovskite film preparation in 2014, numerous alternative anti-solvents, including chlorobenzene (CB), ethyl acetate (EA), and diethyl ether (DE), have been extensively investigated to evaluate their influences on the crystallinity and surface morphology of perovskite films, as well as device performance[133-137]. CB stands as the most widely adopted anti-solvent, primarily because it effectively accelerates the crystallization of perovskite precursors[136,138]. Nevertheless, its high boiling point (132 °C) and low volatility induce internal stress during annealing, ultimately resulting in film cracking. In contrast, isopropyl alcohol (IPA) features a low boiling point and weak coordination, making it conducive to tuning the crystallization rate. Yet IPA exhibits relatively high solubility for perovskite precursors, potentially etching newly formed grains and compromising the microstructural integrity of the perovskite layer.

To overcome the above drawbacks, Song and co-workers systematically investigated six typical anti-solvents [including CB, IPA, dichloromethane (DCM), TOL, EA, and 1,2-dimethoxyethane (DEE)] for controlling the crystallization behavior of perovskite films. As illustrated in Figure 6B, the surface morphologies of $CsPbIBr_2$ films fabricated with these anti-solvents were characterized. Compared with the sample without anti-solvent treatment, all six anti-solvents greatly enhanced film coverage and suppressed pore formation. In particular, the film prepared with DEE exhibited the optimal morphology, featuring a smooth, pinhole-free surface and densely packed grains. Moreover, DEE-treated films exhibited improved crystallographic orientation[139]. These results demonstrate that proper anti-solvent selection facilitates favorable grain alignment and enables the formation of highly pure and well-crystallized $CsPbIBr_2$ films.

It is noteworthy that toxic aromatic hydrocarbon derivatives such as CB, TOL, and dichlorobenzene (DCB) are widely used as anti-solvents for fabricating perovskite films. These toxic solvents pose serious environmental and biological risks. Worse, the anti-solvent-assisted crystallization approach generally requires a large amount of solvent. Even for small lab-scale devices (2 cm^2 × 2 cm^2), the anti-solvent consumption exceeds 0.1 mL per sample[140]. These issues greatly hinder the large-scale industrialization of perovskite modules using toxic solvents. Therefore, developing low-toxicity anti-solvents for high-performance IPSCs continues to be a critical and ongoing challenge.

To address this challenge, Park *et al.* proposed an innovative green solvent engineering strategy, demonstrating the feasibility of utilizing (R)-(+)-limonene (LM) and 2-methyltetrahydrofuran (MeTHF) as eco-friendly anti-solvents for high-quality perovskite film preparation. As illustrated in Figure 6C, the IPSCs fabricated with these green anti-solvents achieved comparable or even superior optoelectronic performance compared with devices prepared with conventional CB, while offering distinct environmental advantages[140]. Additionally, the Luther team discovered that the green anti-solvent methyl formate (MeOAc) can form a unique complex with CsI. Such CsI-based complexes exert a stronger modulation effect on nucleation than PbI_2-DMSO complexes, demonstrating the vital role of the A-site cation in crystallization kinetics. Using this solvent engineering method, the corresponding IPSCs attained a PCE of 14.4%[141].

Annealing process

Perovskite crystallization involves sequential nucleation and grain growth. Controlling these two stages accurately is critical for optimizing film morphology. Among various fabrication procedures, thermal annealing serves as a direct and vital strategy to manipulate the crystallization kinetics of perovskite films. Key annealing variables, including temperature, dwelling time, and treatment method, strongly govern solvent removal, nucleation dynamics, and subsequent grain evolution.

Conventional one-step spin-coating often yields inorganic perovskite layers with undesirable morphology, such as incomplete coverage and poor interfacial contact. These defects mainly arise from rapid DMSO volatilization during high-temperature annealing, which leads to fast nucleation and grain formation. PbI_2

-DMSO and $PbBr_2$-DMSO as intermediate adducts can effectively slow down nucleation kinetics and facilitate the growth of compact $CsPbI_2Br$ films via well-controlled crystallization[48]. Additionally, tuning the DMF/DMSO volume ratio promotes the formation of a CsI-PbX_2-DMSO intermediate phase during the spin-coating process. This reduces the annealing temperature to 100 °C while precisely regulating the crystal growth to yield high-performance $CsPbI_2Br$ films.

Moreover, pre-annealing solvent removal strategies have been explored to optimize intermediate-phase transformation during perovskite crystallization. When $CsPbI_{3-x}Br_x$ precursor films undergo short-duration aging (several minutes) inside a nitrogen-filled glovebox after spin-coating, residual DMSO can volatilize slowly and mildly[142]. This procedure avoids the violent solvent evaporation and rapid crystallization caused by high-temperature annealing, thus restraining irregular grain growth and severe agglomeration. Consequently, the post-annealed films feature a dense, pinhole-free structure composed of large, uniform crystallites.

Numerous studies have confirmed that advanced annealing protocols can substantially improve the crystallization of mixed-halide perovskite films. Chen and co-workers developed a gradient thermal annealing (GTA) strategy to simultaneously modulate DMSO evaporation and the crystallization pathway of $CsPbI_2Br$[143]. The GTA procedure comprises three consecutive treatments at 50 °C for 1 min, followed by 100 °C for 1 min, and finally 160 °C for 10 min. This staged annealing allows *in situ* monitoring of crystallization and morphological evolution, while the gradual temperature rise decelerates DMSO volatilization. Such regulated solvent elimination suppresses abrupt heterogeneous nucleation, minimizes defective intermediates, and favors the oriented growth of pure α-phase $CsPbI_2Br$. Importantly, the α-phase $CsPbI_2Br$ remains stable up to 280 °C, revealing outstanding thermal stability. These results confirm that rational temperature ramping and holding periods, combined with optimized solvent removal, are essential for maximizing the crystallinity and phase stability of $CsPbI_{3-x}Br_x$ perovskite films.

Mali and colleagues proposed a dynamic hot-air (DHA) annealing technique to engineer the crystallization environment of $CsPbIBr_2$ films[78]. In contrast to conventional static annealing, DHA enables real-time modulation of the temperature distribution and ambient atmosphere throughout crystal formation[79]. This dynamic regulation modulates the nucleation and growth kinetics of perovskite domains and yields films with uniform grain size distribution. Consequently, the DHA approach produces compact α-phase $CsPbIBr_2$ films with excellent crystallinity and structural uniformity. Additionally, this method has also been applied to fabricate 1 cm^2 × 1 cm^2 devices, yielding an efficiency of 15.36%. These results confirm the strong potential of DHA for optimizing crystallization and promoting the implementation of high-performance large-area IPSCs[79].

Sanchez and co-workers adopted pulsed infrared flash evaporation annealing to induce crystallization of $CsPbI_{3-x}Br_x$ films. This approach favors the formation of dense perovskite nuclei, while prolonged annealing pulses further drive crystal coarsening, ultimately yielding compact and pinhole-free inorganic $CsPbI_{3-x}Br_x$ layers. According to the study, the corresponding devices maintained 90% of their initial efficiency after thermal aging at 200 °C for 1 h[138]. These findings prove that delicate annealing control is a reliable approach to fabricating high-performance large-area IPSCs.

Post-processing strategy

The fabrication of $CsPbI_{3-x}Br_x$ films inevitably introduces abundant surface defects, which severely deteriorate device performance. Furthermore, deep-level trap states at the surface and continuous halide ion migration during film growth trigger severe non-radiative recombination losses, thus limiting photovoltaic efficiency. Post-treatment strategies typically involve depositing functional overlayers onto inorganic perovskite surface.

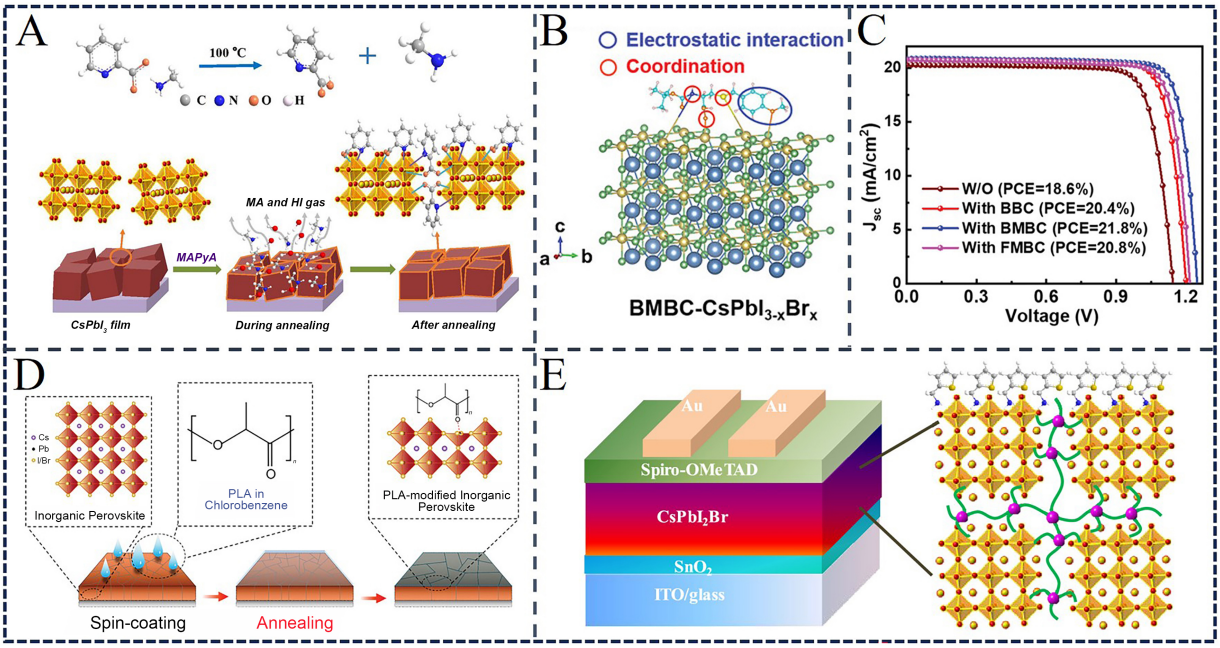

Figure 7. (A) Diagram of the degradation process for MAPyA under 100 °C and MAPyA treatment of $CsPbI_3$ films. This figure is quoted with permission from Ref.[146], Copyright © 2020 American Chemical Society; (B) Theoretical models for the interaction between undercoordinated Pb^{2+} and BMBC; (C) *J-V* curves of $CsPbI_{3-x}Br_x$ IPSCs with different post-treatment methods in the reverse scan under simulated AM1.5 sunlight. (B and C) are quoted with permission from Ref.[40], Copyright © 2023 Wiley-VCH; (D) Illustration of PLA modification for preparing inorganic perovskite. This figure is quoted with permission from Ref.[147], Copyright © 2023 Wiley-VCH; (E) Schematic illustration of the device and the Th-NI treatment of the $CsPbI_2Br$ film. This figure is quoted with permission from Ref.[151], Copyright © 2020 American Chemical Society. BMBC: Boc-S-4-methoxy-benzyl-L-cysteine; BBC: Boc-S-benzyl-L-cysteine; FMBC: N-Fmoc-S-4-methoxy-benzyl-L-cysteine; HI: hydrogen iodide; IPSCs: inorganic perovskite solar cells; ITO: indium tin oxide; MA: methylamine; MAPyA: methylammonium pyridine-2-carboxylate; PCE: power conversion efficiency; PLA: poly(lactic acid).

These strategies aim to passivate surface defects, optimize energy level alignment, suppress non-radiative recombination, and enhance charge transport, thereby boosting the performance of IPSCs. Common passivation agents include Lewis bases, halide salts, organic cationic salts, and organic molecules.

Lewis base molecules possess electron-donating atoms (N, O, S) or functional groups such as carboxylic acid group (-COOH), which can donate lone-pair electrons to fill halide vacancies and form coordination bonds with Pb^{2+} within the inorganic perovskite lattice. This binding behavior efficiently passivates surface trap states and reduces interfacial charge recombination[144]. Chung *et al.* post-treated $CsPbI_2Br$ films with carboxyl-functionalized polythiophene polymers [3-(4-carboxylbutyl) thiophene-2,5-diyl] (P3CT). This treatment repaired and stabilized surface defects in the perovskite films, suppressing non-radiative recombination and promoting charge transport[145]. Fu *et al.* utilized methylammonium pyridine-2-carboxylate (MAPyA) to post-treat perovskite films to stabilize $CsPbI_3$ films. As depicted in Figure 7A, MAPyA decomposes at 100 °C into volatile methylamine (MA) and pyridine-2-carboxylate (PyA^-) anions. The released MA vapor penetrates into the perovskite film to eliminate pinholes and improve uniformity, while PyA^- anchors onto film surfaces and grain boundaries via coordination and ionic interactions. These synergistic effects inhibit phase transformation and reinforce the environmental stability of the $CsPbI_3$ film. Consequently, inverted $CsPbI_3$-based IPSCs achieved an optimal efficiency of 16.67%[146].

A variety of organic molecules, such as Boc-S-benzyl-L-cysteine (BBC), N-Fmoc-S-4-methoxy-benzyl-L-cysteine (FMBC), and Boc-S-4-methoxy-benzyl-L-cysteine (BMBC), feature multiple functional moieties, including NH groups, carbonyl (C=O) groups, and S atoms. These functional groups serve as abundant binding sites to passivate surface and interface vacancies in perovskite films. Zhang *et al.* carried out

post-treatment of perovskite films using BMBC. The methoxy group (-OCH_3) forms a p-π conjugated system with the benzene ring, which increases the electron density of the aromatic ring and strengthens π-π interactions with undercoordinated Pb^{2+} [Figure 7B][40]. Additionally, the *tert*-butyl group in the Boc- moiety inhibits undesirable aggregation at the perovskite/hole transport layer (HTL) interface via steric hindrance. This guarantees uniform BMBC coverage on the film surface and simultaneously constructs a hydrophobic layer, thereby improving the environmental stability of the device. Therefore, $CsPbI_{3-x}Br_x$ IPSCs modified with BMBC attained an efficiency of 21.8% [Figure 7C][40]. Ding and co-workers employed poly(lactic acid) (PLA) as a post-treatment agent to boost the performance of IPSCs [Figure 7D][147]. The C=O group in PLA strongly interacts with uncoordinated Pb^{2+}, effectively passivating surface defects. Meanwhile, PLA modification induces secondary grain growth and enlarges perovskite grain size. After PLA post-treatment, the $CsPbI_{2.25}Br_{0.75}$ IPSC exhibits suppressed non-radiative recombination and reduced energy loss[147].

For halide salt post-treatment, halide exchange occurs spontaneously, eliminating halide vacancies during film processing. Wang *et al.* proposed a post-treatment method using choline iodide dissolved in IPA to modify β-phase $CsPbI_3$ films. Choline iodide distributes uniformly over the perovskite surface, where I^- ions occupy halide vacancies and choline cations anchor at grain boundaries. Moreover, the solution infiltrates and repairs tiny pinholes and cracks within the perovskite layer, greatly enhancing film compactness and reducing interfacial defects. This modification prolongs carrier lifetime and optimizes the energy-level alignment between β-phase $CsPbI_3$ and charge transport layers, thereby promoting charge extraction and minimizing recombination losses. Consequently, the target IPSCs exhibited outstanding reproducibility and ambient stability, delivering a champion PCE of 18.4%[31]. Similarly, Yoon *et al.* used octylammonium iodide (OAI) to surface-passivate β-phase CsPbI3, further boosting device efficiency to 20.37%[148].

Surface functionalization with bulky organic cations or long-chain ligands represents a widely applicable post-treatment route, forming a robust protective capping layer on the perovskite surface. Such layers can efficiently passivate surface defects, optimize energy-level alignment and charge extraction, as well as improve resistance against moisture and thermal stress. As a typical example, phenethylammonium iodide (PEAI) is frequently applied as a surface modifier for $CsPbI_3$ films, creating a passivating capping layer that suppresses defects and markedly enhances the phase stability of α-phase $CsPbI_3$. Consequently, the corresponding IPSCs delivered outstanding fabrication reproducibility and an optimal efficiency of 13.5%[149].

The Tang team utilized S-benzylisothiourea hydrochloride (SBTCl) to improve and stabilize the surface of $CsPbIBr_2$ perovskite films[150]. The N and S heteroatoms in SBTCl supply multiple chelating sites to bind uncoordinated Pb^{2+}, delivering efficient surface passivation. Meanwhile, halide exchange between I^- and Cl^- takes place and induces lattice contraction, forming a continuous Cl gradient doping profile from the surface toward the film bulk. Therefore, the SBTCl-based $CsPbIBr_2$ IPSCs without HTL delivered a notable PCE of 10.56% with a V_{oc} of 1.327 V. The intrinsic hydrophobicity of SBTCl also creates a moisture-proof barrier that blocks moisture invasion and enhances device stability[150]. Fu *et al.* applied 2-thiophenemethylammonium iodide (Th-NI) as a post-treatment modifier for $CsPbI_2Br$ films to realize defect passivation. The thiophenemethylammonium (Th-N^+) cations establish strong electrostatic and coordinative interactions on the perovskite surface, forming a dense protective layer that can inhibit surface recombination and improve perovskite film stability [Figure 7E]. This modification enabled $CsPbI_2Br$ IPSCs to achieve a PCE of 15.58% and a V_{oc} of 1.286 V[151].

Wang *et al.* used *N*, *N*, *N*-trimethyl-1-dodecanaminium bromide (DTABr) dissolved in IPA solution for post-treatment of $CsPbI_3$ perovskite films, promoting secondary grain growth and compensating intrinsic defects[152]. During the annealing process, Br^- penetrates the entire perovskite film to passivate uncoordinated Pb^{2+} and drive partial I^-/Br^- substitution. In contrast, N, N, N-trimethyl-1-dodecanaminium (DTA^+) cations

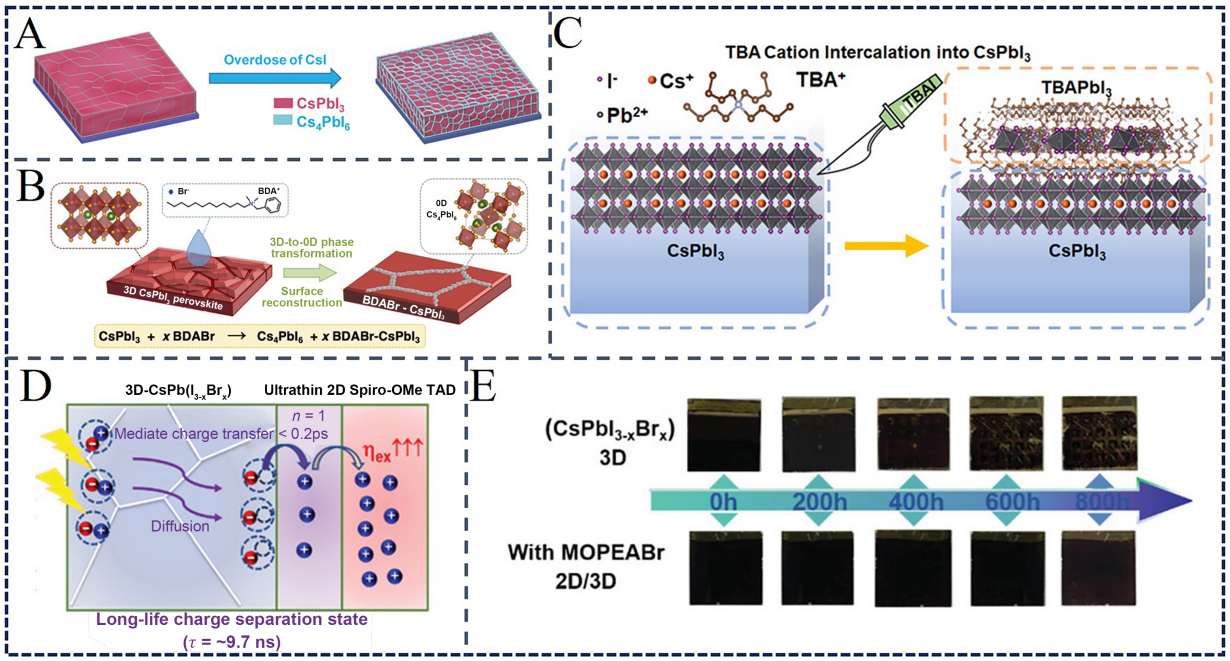

Figure 8. (A) Schematic diagram of the structure of $Cs_{1+x}PbI_{3+x}$ film. This figure is quoted with permission from Ref.[153], Copyright © 2019 Wiley-VCH; (B) Schematic diagram of the phase transition and surface reconstruction of $CsPbI_3$ thin film caused by BDA^+. This figure is quoted with permission from Ref.[154], Copyright © 2023 Elsevier; (C) Schematic diagram illustrating the repair process of $CsPbI_3$ perovskite achieved through TBA^+ cation intercalation. This figure is quoted with permission from Ref.[155], Copyright © 2021 Wiley-VCH; (D) Schematic diagram of photo-induced charge transfer in MOPEABr-treated IPSCs; (E) The environmental stability of different perovskite films. (D and E) are quoted with permission from Ref.[158], Copyright © 2021 Wiley-VCH. BDA^+: Butane-1,4-diammonium; BDABr: butane-1,4-diammonium bromide; IPSCs: inorganic perovskite solar cells; MOPEABr: 2-(4-methoxyphenyl)ethylammonium bromide; TBA^+: tetrabutylammonium; TBAI: tetrabutylammonium iodide; BDA^+: benzyldodecyldimethylammonium; BDABr: benzyldodecyldimethylammonium bromide; MOPEABr: 4-methoxyphenethylammonium bromide.

almost accumulate at the film surface to compensate for Cs^+ vacancies, further repairing the film surface and grain boundary defects. Consequently, the target $CsPbI_3$ devices achieved an excellent efficiency of 20.04% alongside outstanding long-term stability[152]. Likewise, phenyltrimethylammonium bromide (PTABr) can induce a gradient Br doping and passivate surface defects, allowing $CsPbI_3$ devices to reach an efficiency of 17.06%[37].

Low-dimensional perovskites exhibit superior structural stability relative to conventional 3D $CsPbX_3$ frameworks and can serve as a protective barrier that inhibits undesirable phase transitions and material degradation[129]. Accordingly, low-dimensional engineering has been established to passivate surface defects and improve the performance of $CsPbX_3$-based devices. For instance, fine-tuning the stoichiometry of CsI/PbI_2 precursor enables the *in situ* formation of a 0D Cs_4PbI_6/3D $CsPbI_3$ heterostructure surrounding the 3D perovskite lattice. As shown in Figure 8A, the 0D Cs_4PbI_6 phase functions as a passivating shell, effectively stabilizing the photoactive black phase $CsPbI_3$[153]. Similarly, Chen *et al.* achieved a 3D-to-0D phase transformation and surface reconstruction in the $CsPbI_3$ film by introducing the functional benzyldodecyldimethylammonium bromide (BDABr). Owing to steric hindrance, bulky benzyldodecyldimethylammonium (BDA^+) cations cannot be incorporated into the 3D $CsPbI_3$ lattice, and they preferentially induce the formation of a 0D Cs_4PbI_6 phase solely at the grain boundaries of the 3D matrix [Figure 8B]. This grain-boundary-localized 0D phase efficiently passivates Cs-related defects and strengthens the structural robustness of the perovskite film. As a result, the optimized $CsPbI_3$ devices delivered a champion PCE of 20.63%[154].

One-dimensional (1D)/3D composite structures possess dual functions of suppressing defects and reinforcing stability. Tetrabutylammonium iodide (TBAI) was employed for post-treatment to passivate surface defects of $CsPbI_3$ films. Unlike smaller cations [such as dimethylammonium (DMA^+)], the larger tetrabutylammonium (TBA^+) cation is sterically restricted from entering the 3D $CsPbI_3$ lattice, preventing the formation of mixed-cation perovskites. Instead, partial TBA^+ ions anchor on the film surface and form a 1D $TBAPbI_3$ perovskite overlayer [Figure 8C]. The 1D perovskite layer serves as a passivating and protective layer, effectively reducing surface defects and optimizing energy level alignment between $CsPbI_3$ and charge-transport layers. As a consequence, TBAI-treated devices achieved an efficiency of 17.6%[155].

Additionally, two-dimensional (2D)/3D heterostructures have emerged as a promising strategy to enhance the performance of IPSCs. This strategy generally employs long-chain organic components to achieve defect passivation and enhance moisture resistance[156]. With large molecular sizes, these organic moieties cannot integrate into the 3D perovskite framework and tend to form low-dimensional overlayers. Zhang *et al.* established a 2D $EDAPbI_4$-based modification method to stabilize α-phase $CsPbI_3$ films. The terminal NH_3^+ moieties in EDA^{2+} strongly interact with the $CsPbI_3$ lattice, effectively suppressing the formation of the δ-phase. The obtained α-phase $CsPbI_3$ films display exceptional phase stability at ambient temperature and maintain their structural integrity even after thermal annealing at 100 °C for one week[157].

Zhang *et al.* used 4-methoxyphenethylammonium bromide (MOPEABr) in IPA solution to perform post-treatment on $CsPbI_{2.85}Br_{0.15}$ films, successfully constructing a 2D $(MOPEA)_2Pb(Br_xI_{4-x})$/3D $CsPbI_{3-y}Br_y$ heterostructure[158]. The benzene ring of MOPEABr interacts strongly with residual PbI_2 at grain boundaries, which efficiently reduces defect density and prolongs carrier lifetime. As shown in Figure 8D, the as-formed 2D/3D heterostructure facilitates carrier transport, accelerates charge transport dynamics, and improves hole extraction. The target devices delivered a champion efficiency of 20.31% and enhanced environmental stability [Figure 8E][158].

Additive strategy

Introducing functional additives during film fabrication is critical for boosting the phase stability of inorganic perovskite films. Additive engineering generally entails adding functional compounds to the precursor solution to modulate crystallization behavior, optimize the film microstructure, and passivate intrinsic defects, ultimately yielding high-quality inorganic perovskite films[159,160]. Common additives for the active layer include molten salts, ionic liquids, organic small molecules, polymers, ammonium salts, and long-chain organic salts[37,161-165].

As a representative additive, DMAI effectively enhances the film quality and phase stability of black-phase $CsPbI_3$[166]. In the initial stage, DMA^+ ions interact with uncoordinated Pb^{2+} sites and halide vacancies on the film surface and at grain boundaries, thereby forming two intermediate phases ($DMAPbI_3$ and Cs_4PbI_6). During the annealing process, a mixed (DMA, Cs)PbI_3 perovskite phase is generated, and its structure depends on the DMAI concentration[166]. This intermediate phase subsequently decomposes along with DMAI volatilization to form pure $CsPbI_3$[167,168]. This structural transformation involves ion migration and cation exchange. Upon decomposition, Cs_4PbI_6 releases Cs^+ and I^- ions, which penetrate into $DMAPbI_3$ domains and drive the substitution of DMA^+ by Cs^+, eventually forming pure $CsPbI_3$[169]. DMAI gradually volatilizes as the temperature rises. Nevertheless, incomplete removal of residual DMAI tends to create voids and microcracks within films.

To address this issue, Yu *et al.* established a vacuum-assisted thermal annealing (VATA) approach to efficiently remove DMAI vapor before $CsPbI_3$ crystallization [Figure 9A]. Annealing at 1 mbar for only 4 min enabled complete conversion into black α-phase $CsPbI_3$. This treatment proceeds much faster than

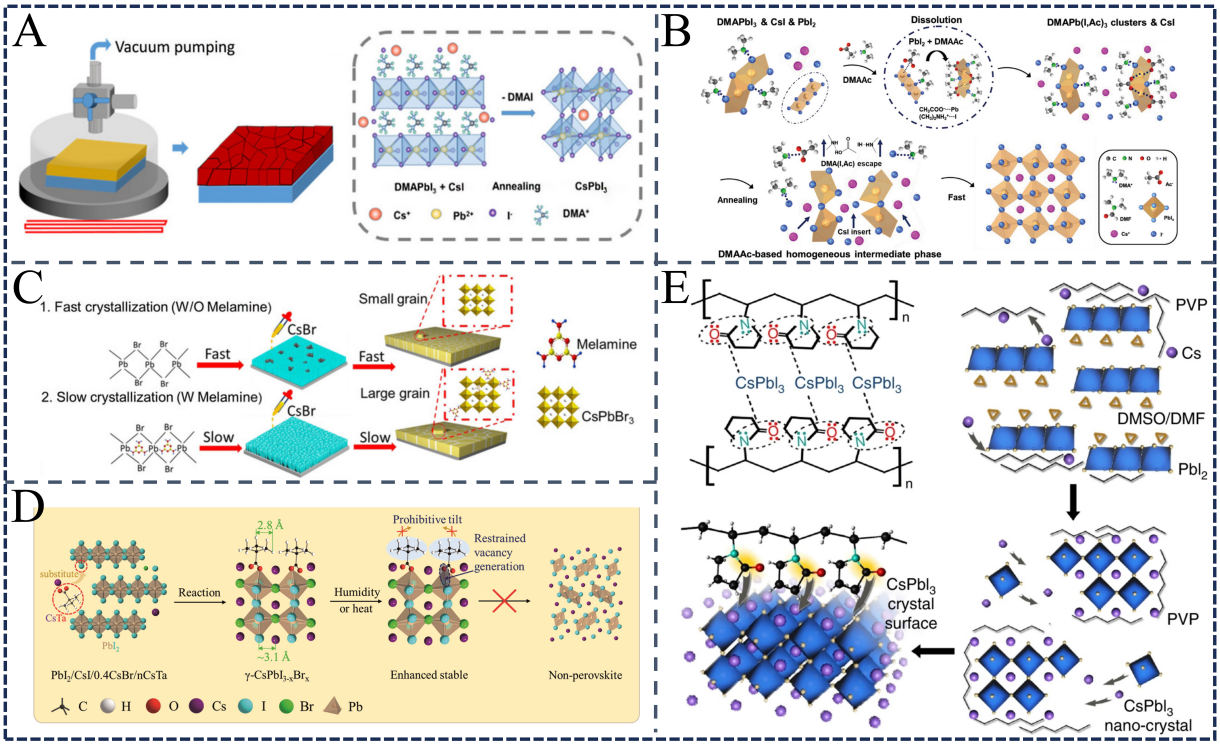

Figure 9. (A) Schematic diagram of the VATA technique for $CsPbI_3$-type perovskite films. This figure is quoted with permission from Ref.[170], Copyright 2022 © Wiley-VCH; (B) A schematic diagram illustrating the evolution process of the crystal structure from the $CsPbI_3$-DMAAc precursor solution to γ-phase $CsPbI_3$, along with the possible chemical interactions and intermediate structures. This figure is quoted with permission from Ref.[169], Copyright © 2022 Wiley-VCH; (C) Schematic diagram showing the formation of perovskite with and without melamine additive. This figure is quoted with permission from Ref.[177], Copyright © 2020 Wiley-VCH; (D) Schematic diagram illustrating the mechanism by which the incorporation of CsTa enhances the stability of the PbI_2-prepared $CsPbI_{2.84}Br_{0.16}$. This figure is quoted with permission from Ref.[179], Copyright © 2021 The Royal Society of Chemistry; (E) The stability mechanism of the cubic phase induced by PVP. Reprinted from Ref.[33] under the CC BY 4.0 license. DMA^+: Dimethylammonium; DMAAc: dimethylammonium acetate; DMF: N,N-dimethylformamide; DMAI: dimethylammonium iodide; DMSO: dimethyl sulfoxide; PVP: poly(vinyl pyrrolidone); VATA: vacuum-assisted thermal annealing.

conventional annealing under identical temperatures. The corresponding IPSCs delivered a PCE of 20.06%, markedly exceeding the control device (17.26%)[170]. In another related work, Cui *et al.* used dimethylacetamide acetate (DMAAc) to suppress the formation of segregated Cs_4PbI_6 during film growth. Ac^- anions coordinate with Pb^{2+} and block I^- incorporation into the Pb(I, Ac) network, thus inhibiting Cs_4PbI_6 formation. Only the uniform $DMAPbI_3$ intermediate phase was observed. This approach eliminates multi-step phase conversion and improves elemental homogeneity. Subsequent heating yielded the stable $DMAPb(I, Ac)_3$ intermediate. Coordination between Ac^- anions and DMA^+ cation increases steric hindrance, accelerates intermediate decomposition, and facilitates the growth of high-quality $CsPbI_3$ films [Figure 9B]. Using this route, the resulting PSC achieved a PCE of 21.14% at a V_{oc} of 1.25 V[169].

Iodine hydride (HI) additive has been widely investigated to improve the performance of $CsPbI_3$ films[171,172]. Adding a trace amount of HI into the perovskite precursor solution facilitates the formation of $HPbI_{3+x}$ intermediate, which enables the synthesis of the black-phase $CsPbI_3$ at low temperatures. To address the solubility challenges of Cs-based precursors, CsAc and $HPbX_3$ are added to the precursor system. The strong synergistic interactions between these components and Pb^{2+} facilitate the growth of smooth, high-quality $CsPbX_3$ perovskite films under relatively mild thermal conditions[129]. Meanwhile, Wang *et al.* successfully fabricated slightly distorted α-phase $CsPbI_3$ films by combining HI and PEAI additives, and the films exhibited enhanced film quality and structural stability[173].

Further investigations have revealed an intrinsic correlation between HI- and DMAI-based modification strategies[174]. In precursor solutions containing DMF, HI inevitably reacts with DMF to generate DMA^+ cations. In contrast to earlier hypotheses, mixing PbI_2 with HI in DMF solution does not yield the proposed $HPbI_3$ species; instead, DMAI and $DMAPbI_3$ are formed as major intermediates. Accordingly, perovskite films prepared with HI or $HPbI_3$ additives are not purely $CsPbI_3$ perovskite, but rather $Cs_{1-x}DMA_xPbI_3$ components. These materials display structural and optoelectronic properties similar to black γ-phase $CsPbI_3$, while DMA^+ incorporation optimizes the electronic structure and enhances charge-transport capability[30,169].

Yang *et al.* used ammonium formate molten salt (AFMS), a low-temperature decomposable additive, to modify the crystallization of $CsPbI_3$ films. AFMS decomposes and completely volatilizes during annealing at relatively low temperatures, thereby eliminating residual impurities. Additionally, the transient liquid phase alters the reaction pathway from the solid state to the liquid state, lowers reaction energy barriers, and enables mild annealing conditions. Therefore, $CsPbI_3$ films with higher crystallinity and larger grain sizes were obtained, and the PCE of the corresponding devices was 21.85%[175].

In terms of molecular additives, organic molecules containing heteroatoms (such as N, O, and S) or specific functional groups (such as $-NH_2$ or -COOH) can interact with the precursor solutions[176-178]. Such electron-rich moieties form strong coordination bonds with undercoordinated Pb^{2+} sites, enabling fine-tuning of crystallization dynamics, efficient defect passivation, and enhanced film stability. For example, introducing phenylthiourea (PTU) forms the PTU-Pb-Br(I) intermediate phase, which reduces the nucleation rate and regulates crystal growth of $CsPbIBr_2$ perovskite. Meanwhile, PTU forms stable chelates with Pb^{2+} via its C=S and $-NH_2$ groups, passivating halide vacancies[176]. Similarly, 1,3,5-triazine-2,4,6-triamine (melamine) cross-links Pb^{2+} through its triazine ring and multiple $-NH_2$ groups, retarding crystallization and producing high-quality $CsPbIBr_2$ films [Figure 9C][177].

Multifunctional organic salt additives exhibit strong interfacial interactions with inorganic perovskites and hold great potential for improving film quality and device performance. Such additives can tailor band structure, regulate crystal growth, passivate defects, and improve film uniformity. Zhao *et al.* employed cesium trimethylacetate (CsTa) as an additive to prepare high-performance $CsPbI_{2.84}Br_{0.16}$ films. The steric hindrance of Ta^- suppresses tilting of the $[PbI_6]^{4-}$ octahedra and prevents the phase transition from corner-sharing perovskite to the edge-sharing non-perovskite structure [Figure 9D]. Meanwhile, the reduction in crystallite size after adding CsTa is beneficial for phase stability, due to the decrease in the surface Gibbs free energy of the perovskite crystal. Furthermore, the Ta^- anions stably occupy halide sites and increase the formation energy of halide vacancies from 0.816 to 1.217 eV. The corresponding IPSCs achieved a maximum efficiency of 16.59% with outstanding ambient stability[179]. In another work, Zhang *et al.* achieved the low-temperature preparation of efficient and stable γ-phase $CsPbI_3$ PSCs by introducing long-chain $EDAI_2$ and optimizing $PbAc_2$ content in the precursor solution. $EDAI_2$ acts as an intermediate to facilitate γ-phase $CsPbI_3$ formation, while the excess $PbAc_2$ can further stabilize the γ-phase $CsPbI_3$ perovskite. The optimized devices demonstrated an efficiency of 16.6% and excellent room-temperature stability[180].

Owing to their ability to modulate film growth via steric hindrance and surface defect passivation, polymeric organic compounds are also widely adopted as effective additives in inorganic perovskite precursor solutions. Their bulky molecular architecture facilitates the decomposition of intermediate phases and the formation of high-quality perovskite frameworks. Incorporating a small quantity of poly(ethylene oxide) (PEO) into the perovskite precursor results in uniform and pinhole-free $CsPbBr_3$:PEO films. Optimizing the PEO-to-precursor mass ratio is crucial for maximizing photovoltaic performance, since PEO limits excessive precursor migration, encourages homogeneous nucleation, and lowers surface roughness[181]. In addition, Li

et al. reported a surface passivation strategy using polymer poly(vinylpyrrolidone) (PVP) to prepare cubic $CsPbI_3$ with ultra-long stability. As shown in Figure 9E, PVP comprises long alkyl chains and acylamino moieties, in which the lone-pair electrons on N and O atoms form coordinate bonds with Cs^+ in the perovskite lattice. During crystal growth, $CsPbI_3$ nanocrystals nucleate and anchor onto the PVP chains, maintaining good dispersion and structural stability through steric hindrance and electrostatic interactions. The acylamino moieties in PVP elevate the electron density at the $CsPbI_3$ surface, which lowers surface energy and helps stabilize the cubic phase of $CsPbI_3$. The $CsPbI_3$ IPSCs based on PVP achieved the highest PCE of 10.74% and exhibited excellent heat and humidity stability[33].

APPLICATION OF IPSCS

Owing to their tunable bandgap, exceptional thermal and chemical robustness, outstanding optoelectronic properties, and solution-processability, inorganic perovskites have found extensive utilization across diverse research and technological fields[182]. Such materials are widely employed in heterojunction solar cells, photodetectors, light-emitting diodes, photocatalysis, amplified spontaneous emission, and other optoelectronic devices[183-191]. In particular, recent breakthroughs in IPSCs have positioned them as a highly competitive candidate for next-generation photovoltaics, with their application scenarios continuing to expand rapidly.

Large-scale IPSCs

Although laboratory-scale IPSCs have achieved relatively high efficiency (over 22%), substantial challenges remain in translating laboratory preparation techniques into large-scale production[42]. As depicted in Figure 10A, multiple deposition methods have been developed for large-area IPSC manufacturing, including spin-coating, slot-die coating, spray coating, drop coating, vacuum evaporation, and other approaches[63,192-197]. Vacuum evaporation can produce high-quality perovskite films, yet it relies on vacuum environments and thus incurs high costs, intensive energy consumption, and low throughput. These intrinsic limitations severely hinder its large-scale manufacturing[63,74]. In this section, we review recent advances in solution-processed large-area IPSCs.

Spin-coating is a widely adopted mainstream approach for lab-scale IPSC preparation, favored for its cost-effectiveness, simple operation, and easy implementation. Nevertheless, key parameters, including film thickness, solvent evaporation kinetics, annealing duration, and heating temperature, strongly affect the crystallinity and morphological uniformity of resultant perovskite films. To overcome the limitations of scalable manufacturing, extensive research has focused on optimizing conventional solution-processing techniques, enabling uniform, high-performance films to be deposited on large-area substrates. Mai and co-workers tuned the LUMO energy level of C60 by incorporating TPFPB, generating a Lewis acid adduct that promotes electron injection and suppresses charge recombination[198]. Further modification with $LiClO_4$ improves electron mobility and electrical conductivity, markedly mitigating device hysteresis. Leveraging these strategies, a large-area module was successfully constructed via quasi-curved heating [Figure 10B], delivering an efficiency of 12.19% over an active area of 10.92 cm^2[198].

Chen *et al.* used N-methyl-2-pyrrolidone (NMP) to pre-coordinate PbI_2 and form PbI_2·NMP complexes *in situ*. The as-prepared complexes were then added to the HI-containing precursor solution to form high-quality α-phase $CsPbI_3$ films[199]. Meanwhile, 1,4,7,10,13,16-hexaoxacyclooctadecane ether (crown ether) was employed to inhibit moisture ingress and passivate surface defects. The outer methylene ($-CH_2$) structure of crown ether can prevent moisture erosion, while its inner cavity binds tightly to surface Cs^+ ions for effective defect passivation [Figure 10C]. With this integrated strategy, large-area modules with an effective area of 8 cm^2 achieved a PCE of over 11.87%. Moreover, this process is also compatible with blade coating. The same-area $CsPbI_3$ perovskite module fabricated via blade coating exhibited an efficiency of 10.73%, further confirming the universality of this strategy for scalable deposition[199].

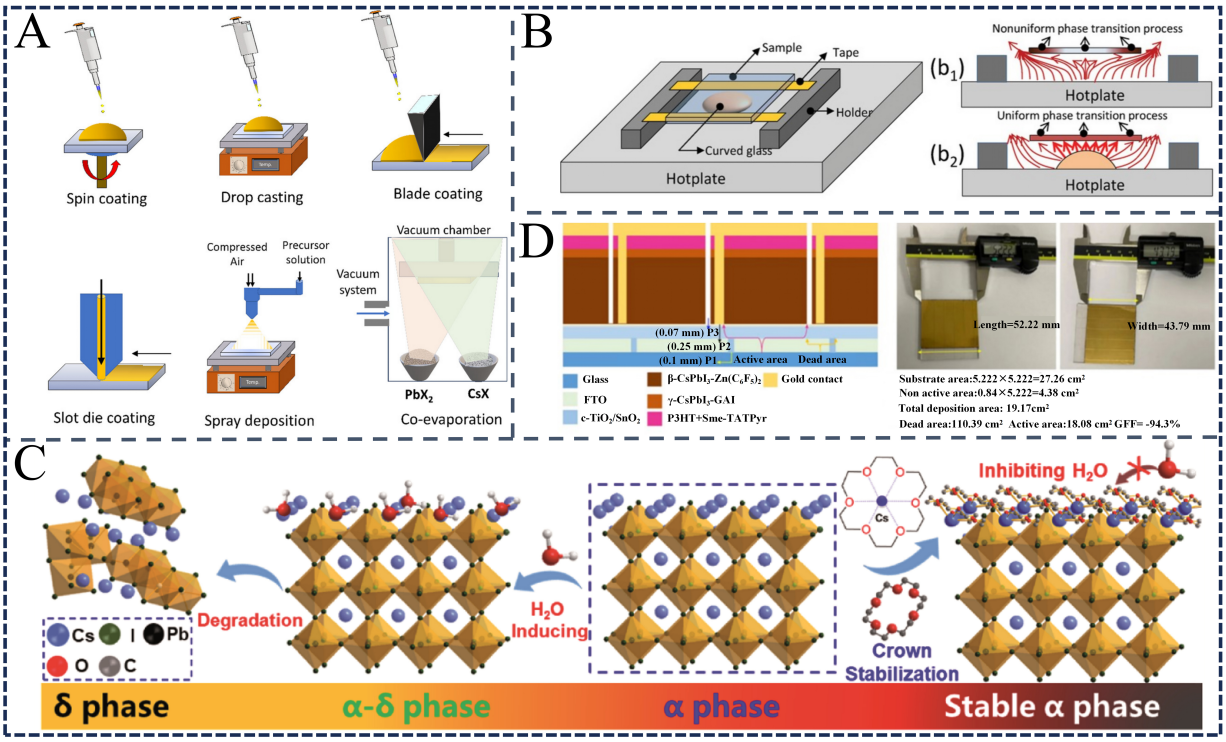

Figure 10. (A) A schematic diagram of a deposition method for large areas (≥ 1 cm^2 × 1 cm^2) inorganic devices. Reprinted from Ref.[63] under the CC BY 4.0 license; (B) A schematic diagram of preparing $CsPbI_2Br$ films on large-sized substrates using the quasi-curved heating method. This figure is quoted with permission from Ref.[198], Copyright © 2020 Wiley-VCH; (C) Schematic diagram of crown passivation on the surface of α-phase $CsPbI_3$ and comparison with the phase transformation from α-phase $CsPbI_3$ to δ-phase $CsPbI_3$. This figure is quoted with permission from Ref.[199], Copyright © 2020 The Royal Society of Chemistry; (D) The left figure shows the schematic structure of the inorganic perovskite micro-module based on $CsPbI_3$-$Zn(C_6F_5)_2$/γ-$CsPbI_3$-GAI, and the right figure is a photo of the module. This figure is quoted with permission from Ref.[200], Copyright © 2023 Springer Nature. GAI: Guanidine iodide.

Mali *et al.* have developed methylammonium iodide (MAI)-assisted β-phase $CsPbI_3$ and guanidine iodide (GAI)-assisted γ-phase $CsPbI_3$ to prepare IPSCs, which were obtained via hot air treatment and three-source thermal evaporation deposition, respectively. DMAI and $Zn(C_6F_5)_2$ were added to the precursor solution as additives for improving the crystallinity and phase stability of β-phase $CsPbI_3$. Co-evaporated GAI optimizes film morphology, optoelectronic characteristics, and long-term device stability during the formation process of γ-phase $CsPbI_3$. The structural schematic and photograph of the heterojunction micro-module are shown in Figure 10D. The heterojunction formed using these modified materials exhibits suppressed charge recombination and improved charge separation and transport, leading to effective enhancement in overall device performance. The optimized module, with an area of 18.08 cm^2, obtained a PCE of 18.43%, demonstrating great potential for large-scale application[200].

As a simple and scalable film fabrication method, drop-coating is plagued by the well-known coffee ring effect. This phenomenon arises from uneven solvent evaporation rates between the droplet edge and center, leading to inhomogeneous solute distribution and poor film quality[201]. To address this problem, vacuum-assisted (VA) technology has been adopted to improve the quality of inorganic perovskite films[202,203]. The VA process accelerates solvent evaporation by lowering chamber pressure, enabling precise control over film crystallization and morphology. Zhang *et al.* compared thermal-assisted (TA) and VA drop-coating processes, revealing that reduced pressure narrows the evaporation rate difference between the droplet edge

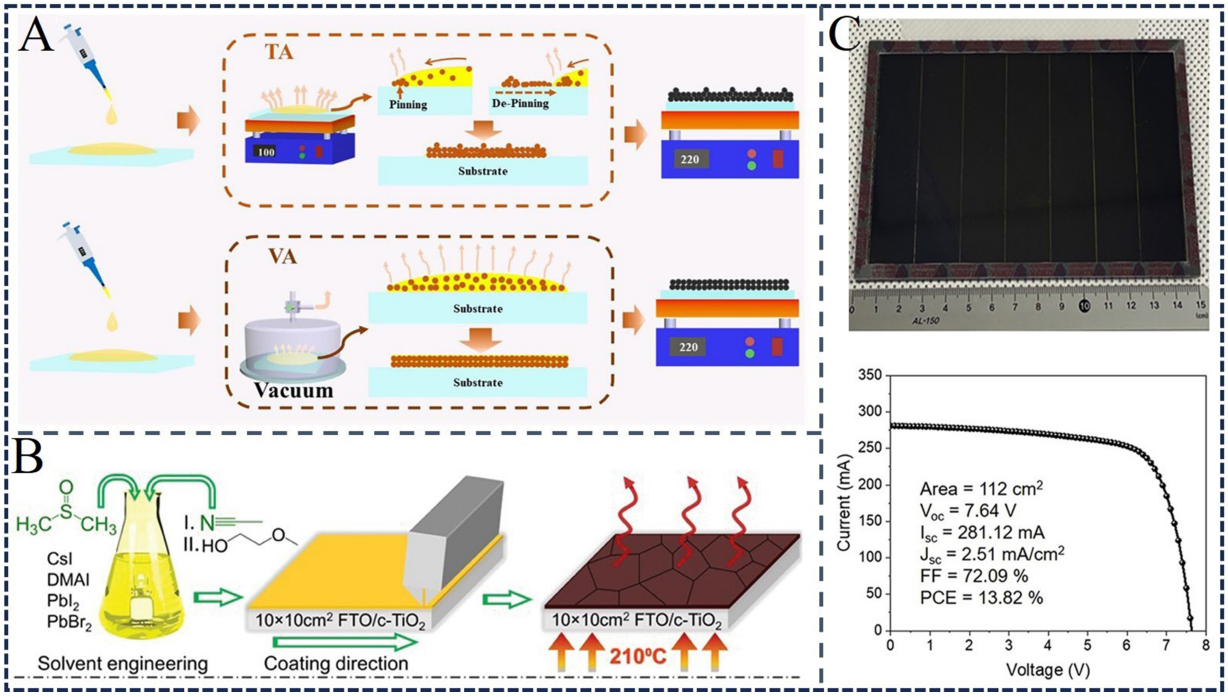

Figure 11. (A) Schematic diagram of the TA and VA methods. This figure is quoted with permission from Ref.[202], Copyright © 2023 Elsevier; (B) Schematic diagram of the development of eco-friendly inorganic perovskite inks through solvent and colloid engineering technology for large-scale IPSCs. This figure is quoted with permission from Ref.[80], Copyright © 2022 Wiley-VCH; (C) Photograph and *J-V* curve of a graded $CsPbI_{3-x}Br_x$ IPSC module. This figure is quoted with permission from Ref.[205], Copyright © 2021 Elsevier. DMAI: Dimethylammonium iodide; FF: fill factor; FTO: fluorine-doped tin oxide; IPSCs: inorganic perovskite solar cells; PCE: power conversion efficiency; TA: thermal annealing; VA: vacuum annealing.

and center, thereby suppressing the coffee ring effect and enhancing film uniformity [Figure 11A]. Using the VA strategy, they fabricated high-quality 5 cm^2 × 5 cm^2 $CsPbI_3$ IPSCs with an efficiency exceeding 16%[202].

As a commonly used scalable technique for fabricating IPSCs, blade coating has been widely applied in related research. Tan *et al.* used benzyltrimethylammonium bromide (BTABr) as an additive to successfully deposit $CsPbI_{3-x}Br_x$ films through low-temperature blade-coating. The resulting 12 cm^2 module achieved a high efficiency of 16.60%[204]. Nevertheless, blade-coating has inherent drawbacks, including poor compatibility with rigid substrates and limited patterning capability. The drawbacks restrict its large-scale production and versatile device design. Accordingly, slot-die coating has emerged as a favorable alternative, supporting both batch and high-throughput R2R production while enabling precise scalable deposition. Abate *et al.* developed a green-solvent approach for slot-die-coated $CsPbI_{2.77}Br_{0.23}$ films, using high-vapor-pressure, low-coordination acetonitrile (ACN) and 2-methoxyethanol (2-ME) combined with DMSO [Figure 11B]. Solvent composition strongly influences film crystallinity and morphology. At an optimal volume ratio, the 2.5 cm^2 × 2 cm^2 device and 10 cm^2 × 10 cm^2 module containing six subcells reached PCE of 16.03% and 8.07%, respectively[80].

Spray-coating is another prevalent low-temperature solution processing method for fabricating large-area high-quality films[76]. Heo *et al.* adopted this technique to prepare $CsPbI_2Br$ perovskite modules. Sequential spray deposition of $CsPbI_3$ atop pre-formed $CsPbI_2Br$ film constructs a gradient $CsPbI_{3-x}Br_x$ structure, which promotes charge transport and mitigates charge recombination. As a result, the 112 cm^2 perovskite module achieved a PCE of 13.82% [Figure 11C][205]. Likewise, continuous spray coating was applied to fabricate high-performance $CsPbI_3$ IPSCs. A $Ti_3C_2T_x$ MXene (OMXene)-$CsPbI_3$ composite layer was formed through sequentially spraying $CsPbI_3$ precursor solution and pre-oxidized OMXene, which establishes an electric field

and acts as an effective moisture barrier. The optimized 25 cm^2 OMXene-$CsPbI_3$ module reached a 14.64% PCE and exhibited excellent long-term operational stability[206].

TSCs

The relatively WBG of Pb-based inorganic perovskites limits their light absorption range and yields low photocurrent density, which restricts the efficiency improvement of single-junction devices. TSCs overcome this bottleneck via spectral splitting and rational bandgap engineering to maximize efficiency.

In such stacked structures, the WBG top cell captures short-wavelength and high-energy photons, while the bottom cell adopts narrow bandgap (NBG) materials to absorb long-wavelength and low-energy photons. This complementary spectral absorption reduces thermalization and optical transmission losses, thereby enabling more efficient utilization of the solar spectrum. TSCs are generally divided into two-terminal (2T) and four-terminal (4T) structures. Compared with 4T devices, the 2T TSCs feature simpler fabrication procedures, lower manufacturing costs, and minimized parasitic absorption and reflection losses. Thus, they are highly promising for efficient and scalable photovoltaic applications[207]. Currently, TSCs can be classified into four categories based on the choice of top and bottom subcell materials.

Inorganic perovskite/GaAs TSCs

All-inorganic perovskite/GaAs TSCs exhibit great potential for aerospace applications. Wang *et al*. conducted simulations and optimizations for 4T and 2T inorganic $CsPbIBr_2$/GaAs TSCs. By optimizing the thickness of each functional layer and introducing anti-reflective coatings to reduce reflection and parasitic absorption, a remarkable PCE level of up to 30.67% was achieved based on 2T $CsPbIBr_2$/GaAs TSCs under AM 1.5G illumination. Additionally, the efficiency of the 2T TSC reached 27.23% under AM 0 conditions[208].

All-perovskite TSCs

Compared with WBG hybrid perovskites, inorganic $CsPbI_{3-x}Br_x$ perovskite possesses excellent photothermal stability, making it an ideal candidate as the top cell of all-perovskite TSCs. By integrating perovskite absorbers with different bandgaps, TSCs exhibit a theoretical efficiency up to 46%, far exceeding the Shockley-Queisser limit for single-junction PSCs (33.7%)[62]. Li *et al.* constructed a 2T TSC composed of a WBG inorganic $CsPbI_{3-x}Br_x$ top subcell and an NBG hybrid $FA_{0.7}MA_{0.3}Pb_{0.5}Sn_{0.5}I_3$ bottom subcell, yielding an efficiency of 25.6% [Figure 12A][209]. Our group reported that introducing the antioxidant additive dicyandiamide (DCD) suppresses Sn^{2+} oxidation and regulates the crystallization of $CsPb_{1-x}Sn_xI_2Br$ films. Meanwhile, we coupled the $CsPb_{0.6}Sn_{0.4}I_2Br$ (1.54 eV) subcell with the ITO/NiO_x/$CsPbI_2Br$ (1.92 eV)/$Ti_{0.9}Sn_{0.1}O_2$/IZO/MgF_2 transparent device to construct a 4T all-inorganic perovskite TSC. The 4T device achieved an efficiency of 19.61%, representing the first report on 4T all-inorganic perovskite TSC[62]. Similarly, Sun and colleagues developed a 4T TSC comprising an NBG $CsPb_{0.5}Sn_{0.5}I_{2.7}Br_{0.3}$ (1.39 eV) bottom cell and a semi-transparent WBG (1.98 eV) $CsPbI_{1.5}Br_{1.5}$ top cell [Figure 12B], which achieved a PCE up to 18% and a V_{oc} of 2.13 V. Benefiting from the high output voltage, such TSCs are promising power sources for solar-driven water splitting to prepare hydrogen and oxygen[210].

Recently, our group employed the ligand evolution strategy of *p*-toluenesulfonyl hydrazide (PTSH) to improve the performance of the NBG $CsPb_{0.4}Sn_{0.6}I_3$ (1.31 eV) subcells [Figure 12C]. During low-temperature treatment, PTSH coordinates with Pb^{2+}/Sn^{2+} ions to regulate perovskite crystallization kinetics. At the subsequent high-temperature annealing stage, PTSH acts as a reducing agent to convert oxidized Sn^{4+} to Sn^{2+}, while the generated *p*-toluenesulfonic acid efficiently passivates film defects. By integrating the $CsPb_{0.4}Sn_{0.6}I_3$ subcells with the 1.92 eV $CsPbI_2Br$ subcell, we successfully prepared the first 2T all-inorganic TSC with an efficiency exceeding 22.5% (certified efficiency 21.923%), outperforming previously reported single-junction

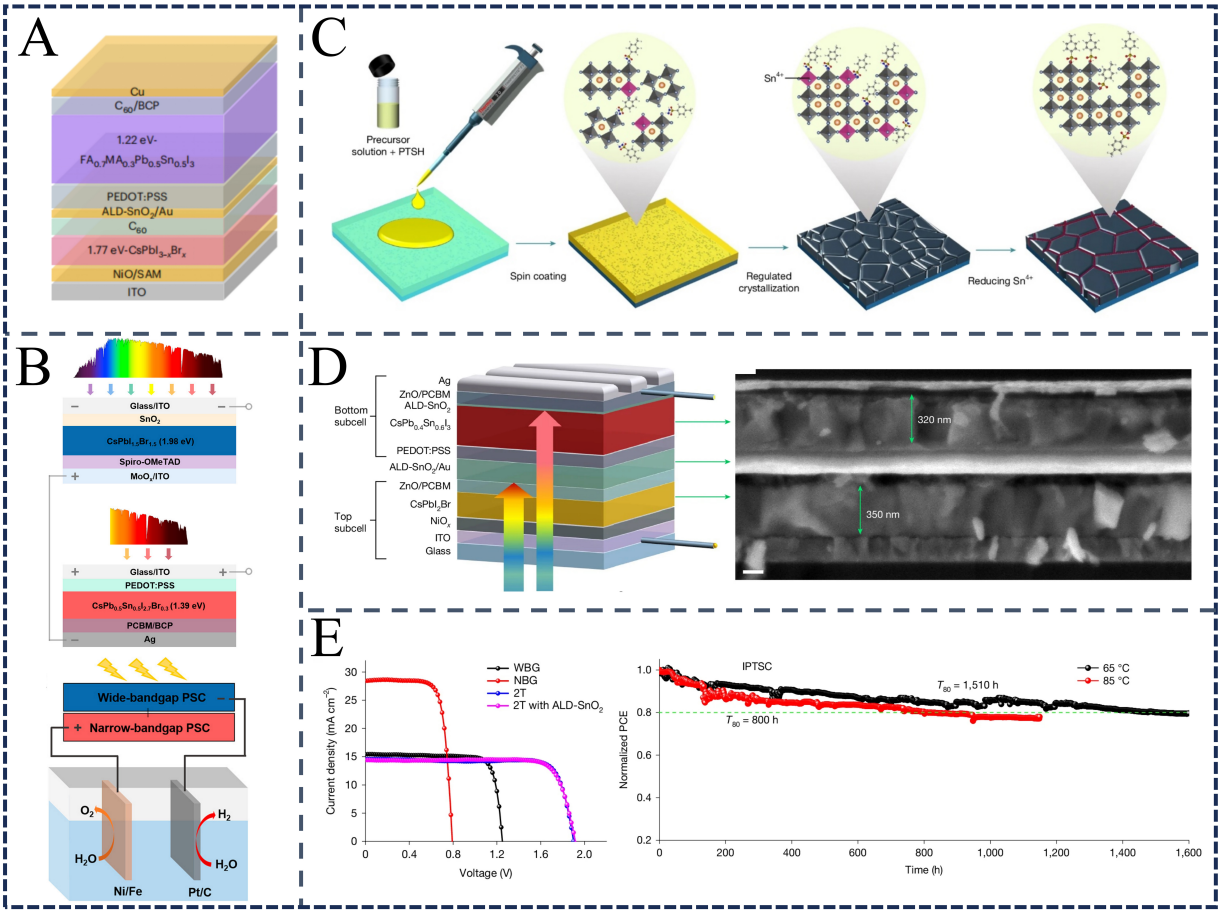

Figure 12. (A) Schematic structure of $FA_{0.7}MA_{0.3}Pb_{0.5}Sn_{0.5}I_3/CsPbI_{3-x}Br_x$ all-perovskite TSCs. This figure is quoted with permission from Ref.[209], Copyright © 2023 Springer Nature; (B) The schematic diagram of the Integrated 4T inorganic perovskite TSC and the solar water splitting system driven by the integrated 4T inorganic perovskite TSC. This figure is quoted with permission from Ref.[210], Copyright © 2022 American Chemical Society; (C) Schematic diagram of ligand evolution strategy; (D) 2T inorganic perovskite TSC structure diagram; (E) *J-V* curve and stability of 2T inorganic perovskite TSC. (C-E) are quoted with permission from Ref.[20], Copyright © 2025 Springer Nature. 2T: Two-terminal; 4T: four-terminal; ALD: atomic layer deposition; BCP: bathocuproine; FA: formamidinium; ITO: indium tin oxide; MA: methylammonium; NBG: narrow-bandgap; PCBM: phenyl-C61-butyric acid methyl ester; PEDOT:PSS: poly(3,4-ethylenedioxythiophene):poly(styrene sulfonate); PCE: power conversion efficiency; PSC: perovskite solar cell; PTSH: *p*-toluenesulfonyl hydrazide; SAM: self-assembled monolayer; TSCs: tandem solar cells; WBG: wide-bandgap.

IPSCs [Figure 12D and E]. Additionally, the 2T TSCs exhibited excellent photothermal stability. Under maximum power point tracking, the device could still maintain 80% of its original efficiency at 65 °C for 1,510 h and 85 °C for 800 h [Figure 12E][20].

Inorganic perovskite/organic TSCs

Wang *et al.* employed a $CsPbI_2Br$ cell as the top subcell to construct inorganic perovskite/organic TSCs, yielding an efficiency of 21.1%[211]. In a parallel strategy, undoped low-cost poly[(thiophene)-alt-(6,7-difluoro-2-(2-selenedodecyl)quinoxaline)] (PTQ10) was applied as both the top HTL and the interconnection layer. TSCs integrating organic subcells (PM6:Y6 or D18:Y6) with $CsPbI_2Br$ subcells delivered an efficiency of 21.4%[25]. Lang *et al.* proposed a surface reconstruction strategy driven by ionic liquids, which used dimethylammonium acetate (DMAAc) to induce the formation of the $DMAPb(I_2Br)_{1-x}Ac_{3x}$ intermediate phase on the surface of $CsPbI_2Br$. After *in situ* recrystallization induced by annealing, high-quality perovskite films were obtained. This approach optimizes surface morphology, eliminates ionic defects, and tailors interfacial energy level alignment, thereby greatly improving the efficiency and stability of

perovskite/organic TSCs. The optimized devices achieved a maximum PCE of 24.20%[212]. Han *et al.* synthesized acid-modified Mg-doped SnO_2 QDs to regulate the bottom interface contact of WBG $CsPbI_2Br$ IPSCs. The single-junction $CsPbI_2Br$ device achieved a PCE of 19.2% and a V_{oc} of 1.44 V. In addition, the perovskite/organic TSC prepared in combination with PM6:BTP-eC9:TCB organic subcells achieved an efficiency of 25.9% (certified efficiency of 25.1%)[213]. Meanwhile, this group further introduced the polymer acceptor PY-IT into the PM6:BTP-eC9 system to regulate the morphology of the blend film, converting isolated acceptor clusters into ordered aggregates, thereby increasing the PCE of the organic single-junction device from 17.97% to 19.60%. The TSC prepared by combining the $CsPbI_2Br$ perovskite subcell achieved an efficiency of 26.07%[214].

Inorganic perovskite/silicon-type TSCs

C-Si solar cells dominate the photovoltaic market, with a bandgap width of 1.12 eV, which effectively absorbs sunlight across the 300 to 1,200 nm wavelength range. The laboratory maximum PCE of silicon cells has reached 27.6%, approaching its theoretical limit of 29.4%[215]. The perovskite/silicon TSC combines the advantages of both technologies and is expected to achieve higher conversion efficiency, showing enormous application potential[216].

Wang *et al.* introduced IPSCs into the silicon-based tandem architecture for the first time in 2022. They adopted the NiI_2/IPA solution to passivate defects in $CsPbI_{3-x}Br_x$ films, effectively reducing trap states and stabilizing the crystal structure. Thereby, the $CsPbI_{3-x}Br_x$/silicon TSC achieved an efficiency of 22.95%[217]. The team further used 2-amino-5-bromobenzenamine (ABA) for post-treatment of perovskite films. This material fills halide vacancies and suppresses the formation of Pb^0 defects, thereby significantly reducing non-radiative recombination and ion migration, and enhancing charge extraction. Ultimately, the efficiency of the inverted $CsPbI_{2.85}Br_{0.15}$ IPSCs and the corresponding TSC based on c-Si reached 20.38% and 25.31%, respectively. This work also represents the first demonstration of inverted IPSCs integrated into silicon-based TSCs[218].

Due to the excellent photothermal stability of inorganic perovskites, research on their application in tandem devices has grown rapidly. In particular, the recent advancements in defect passivation, interface modification, and inverted device design have laid a solid foundation for driving breakthroughs in this research field.

Flexible IPSCs

Flexible perovskite photovoltaic devices have garnered considerable attention owing to their superior mechanical compliance, light weight, compatibility with curved surfaces, and portability. Flexible devices can be mass-produced via R2R processing, rendering them highly promising for next-generation photovoltaic applications. However, commonly used polyimide flexible substrates have a maximum service temperature below 250 °C, making low-temperature deposition techniques indispensable. Rapid progress in low-temperature fabrication of high-quality inorganic perovskite films has paved the way for the realization of flexible IPSCs[219].

Compared with $CsPbI_3$ perovskite, α-phase $CsPbI_2Br$ films can be fabricated at lower temperatures while retaining excellent phase stability, rendering them ideal light-absorbing layers for flexible devices. Rao and co-workers reported a DMSO-coordination-assisted route to prepare $CsPbI_2Br$ perovskite films at room temperature[220]. A simple room-temperature solvent annealing [room-temperature solvent annealing (RTSA)] process enables controllable removal of high-boiling-point DMSO, thereby obtaining highly uniform and pinhole-free $CsPbI_2Br$ perovskite films [Figure 13A]. After secondary annealing at the optimal temperature of 120 °C, the resultant flexible PSCs achieved a PCE of up to 7.3%[220].

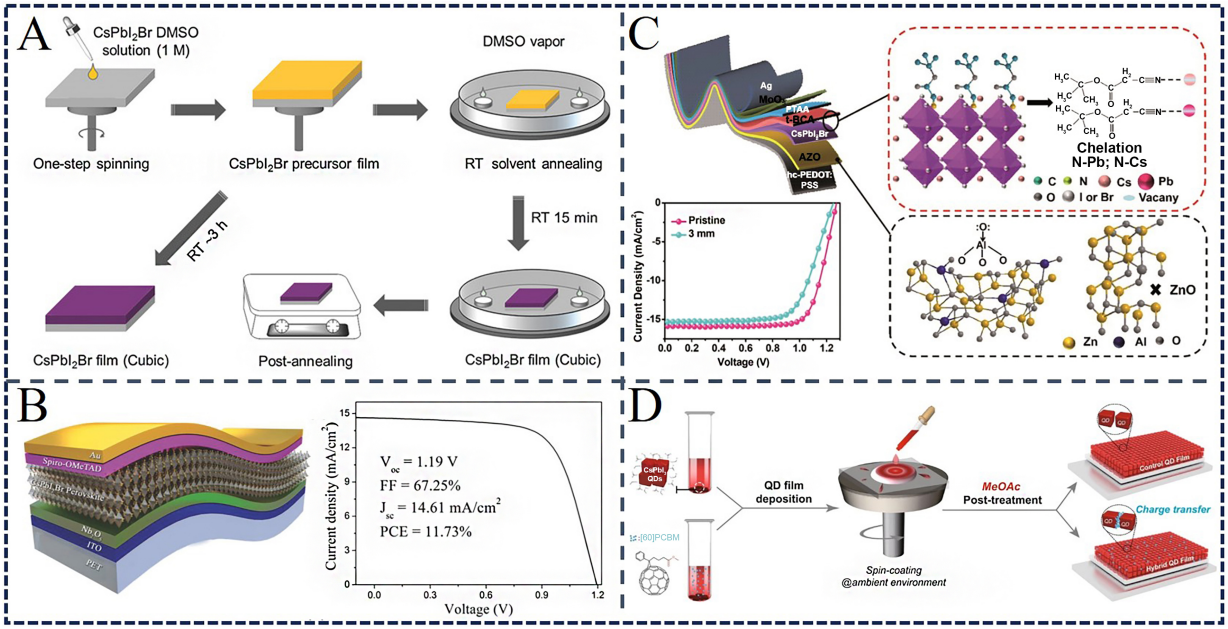

Figure 13. (A) Schematic diagrams of the process flow for preparing $CsPbI_2Br$ films using RTSA and direct thermal annealing. This figure is quoted with permission from Ref.[220], Copyright © 2018 Wiley-VCH; (B) Schematic diagram and *J-V* curve of flexible $CsPbI_2Br$ IPSC. Reprinted from Ref.[221] under the CC BY 4.0 license; (C) Schematic diagram of the interaction between t-BCA and perovskite, as well as ball-and-stick models of AZO and ZnO. The *J-V* curves of the flexible IPSC before and after 1,000 bending cycles (bending radius of 3 millimeters). This figure is quoted with permission from Ref.[223], Copyright © 2020 The Royal Society of Chemistry; (D) Schematic diagram of the preparation principles of original, controlled, and mixed $CsPbI_3$ quantum dot films. Reprinted from Ref.[224] under the CC BY 4.0 license. AZO: Aluminum-doped zinc oxide; BCA: cyanoacetate; DMSO: dimethyl sulfoxide; FF: fill factor; IPSC: inorganic perovskite solar cell; MeOAc: methyl acetate; PCBM: phenyl-C61-butyric acid methyl ester; PCE: power conversion efficiency; PET: polyethylene terephthalate; QD: quantum dot; RT: room temperature; RTSA: room-temperature solvent annealing; t-BCA: tert-butyl cyanoacetate.

Jiang *et al.* utilized a low-temperature DMSO-adduct-promoted process (DAPP) to fabricate high-performance $CsPbI_2Br$ films. At 60 °C, PbX_2 reacts with DMSO to form PbI_2·DMSO and $PbBr_2$·DMSO adducts, which suppress fast precursor reactions and moderate crystallization kinetics. Replacing commercial PbI_2 and $PbBr_2$ with the as-prepared DMSO adducts enables low-temperature (120 °C) preparation of dense, pinhole-free $CsPbI_2Br$ perovskite films with high crystallinity and stability. Therefore, flexible $CsPbI_2Br$ IPSCs based on the DAPP strategy delivered a PCE of 11.73%, as shown in Figure 13B[221]. Liu *et al.* used NMP as the precursor solvent and prepared flexible $CsPbI_2Br$ IPSCs with an efficiency of 6.05% at room temperature. However, the flexible device retained only approximately 80% of its initial efficiency after 200 bending cycles[222].

Yang *et al.* fabricated low-temperature processed flexible $CsPbI_2Br$ PSCs by employing aluminum-doped zinc oxide (AZO) as the electron transport layer (ETL) and tert-butyl cyanate (*t*-BCA) as the passivation layer. The thickness-insensitive AZO layer effectively improves perovskite film quality and enhances device fabrication reproducibility. The cyano groups of *t*-BCA form coordinate bonds with uncoordinated Pb^{2+} and Cs^+ ions, which efficiently passivate trap states and suppress charge recombination within the $CsPbI_2Br$ film [Figure 13C]. The champion flexible device delivered a promising efficiency of 15.08%. Moreover, these devices also exhibit outstanding stability under various aging conditions. Even after 1,000 bending cycles at a curvature radius of 3 mm, the device still preserved 85% of its initial performance [Figure 13C][223].

Hu *et al.* developed a hybrid interfacial architecture (HIA) by introducing phenyl-C61-butyric acid methyl ester (PCBM) into the $CsPbI_3$ QD layer, as described in Figure 13D. PCBM binds to uncoordinated Pb^{2+} on the QD surface through functional carboxyl groups and forms an exciton transport cascade between the

$CsPbI_3$ QD layer and the SnO_2 ETL. This structure facilitates efficient charge transfer and accelerates photon dissociation at the QD/ETL interface. Through this HIA strategy, the efficiency of the fabricated flexible QD solar cells reached 12.3%. Further studies on the mechanical properties of two representative films, namely $CsPbI_3$ QD films and $CsPbI_2Br$ films, revealed that the QD films possess superior mechanical durability. The inherent nanoscale grain boundaries and flexible surface ligands in low-dimensional QD materials facilitate the release of internal film stress[224].

Yao and co-workers introduced a heterogeneous CaF_2 nanocrystal seed-induced approach to improve the crystallization quality of flexible $CsPbI_{2.81}Br_{0.19}$ perovskite films[225]. The strong lattice matching between CaF_2 nanoparticles and the perovskite lattice reduces the nucleation Gibbs free energy, promoting the low-temperature formation of stable γ-phase $CsPbI_{2.81}Br_{0.19}$. This approach produces high-quality, defect-free, and stable perovskite films. The optimized flexible IPSCs delivered a PCE of 15.03% and exceptional mechanical robustness. After 60,000 bending cycles at a 5 mm curvature radius, the flexible IPSCs could retain 98.1% of their original efficiency[225].

CHALLENGES AND OPPORTUNITIES

Although IPSCs have achieved tremendous progress in recent years, several critical bottlenecks still hinder their practical application and commercialization. The main challenges involve insufficient phase stability, high defect density, moderate device performance, and limitations in scalable fabrication. Overcoming these bottlenecks is essential to fully unlock the application potential of inorganic perovskites for next-generation photovoltaic technologies.

Phase separation

Br^- doping is known to boost the phase stability of $CsPbI_{3-x}Br_x$. Nevertheless, mixed-halide inorganic perovskites are less thermodynamically stable than previously thought, and the phase separation behavior and optical properties of such materials remain controversial. Rachel and co-workers systematically investigated the photostability of $CsPbI_{3-x}Br_x$ across the full Br composition range (x = 0-3) using photoluminescence spectroscopy[226]. Stable photoluminescence signals were observed for samples with $0 \leq x \leq 1$, whereas a distinct spectral redshift occurred for $1 < x < 3$. These findings suggest a wider composition window with suppressed phase separation in inorganic perovskites. In contrast, other studies reported stable photoluminescence only within the narrow range of $0.6 < x < 1.2$. Draguta *et al*. found that $CsPbI_{1.5}Br_{1.5}$ films exhibited a photoluminescence peak shift from 637 to 687 nm following 100 s of illumination at 60 $mW \cdot cm^{-2}$, confirming the occurrence of phase separation[227].

In halide perovskites, ion migration is remarkably faster at grain boundaries than within the bulk, which are dominant channels for halide ion migration and subsequent phase segregation. To mitigate halide phase segregation, multiple strategies have been explored, among which three mainstream approaches exhibit strong efficacy in suppressing phase separation of $CsPbI_{3-x}Br_x$ perovskites: compositional engineering for perovskite lattice stabilization[228-230]; grain boundary reduction via crystallization optimization[231]; and defect passivation to eliminate ion vacancies, thereby strongly suppressing phase separation[232-234]. Fundamentally, these strategies increase the activation energy for halide ion migration, alleviate lattice distortion and electron-phonon interactions, and reduce defect traps within the perovskite layer.

The partial substitution of Pb^{2+} with Sn^{2+} has been verified as an efficient approach to suppress phase separation in inorganic perovskites[235,236]. Li and co-workers demonstrated that the photoluminescence peak position of $CsPb_{0.75}Sn_{0.25}IBr_2$ remained unchanged after 15 min of continuous light illumination, whereas the photoluminescence peak of the pristine $CsPbIBr_2$ film showed an obvious redshift under identical test conditions. This result confirms that Sn^{2+} alloying effectively improves the phase stability of $CsPbI_{3-x}Br_x$

perovskites[237]. The stability improvement arises from distinct bonding characteristics of Sn-halide bonds versus Pb-halide bonds, which more effectively suppress halide segregation in Pb-Sn binary inorganic perovskite systems.

Recently, our research revealed that excessive Sn^{2+} doping (x > 0.5) triggers severe photothermal-induced phase separation in $CsPb_{1-x}Sn_xI_3$ perovskite films, accompanied by the formation of Pb-rich secondary phases[52]. This degradation primarily arises from the deteriorated film quality caused by excess Sn^{2+} doping, as well as light-triggered film decomposition, spontaneous ion migration, and phase separation of inorganic perovskite films. We used guanidine acetic acid as a ligand additive to regulate the crystallization kinetics of the inorganic perovskite film, thereby significantly improving its morphological quality. The additive constructs a robust crystal framework stabilized by ionic bonding and hydrogen bonding with perovskite components, which substantially reinforces the intrinsic stability of the corresponding films[52].

Efficiency bottleneck

Efficient solar spectral matching is a prerequisite for sufficient light harvesting of all-inorganic perovskites. For high-performance single-junction solar cells, the theoretical optimal bandgap corresponding to the Shockley-Queisser limit is approximately 1.34 eV[238]. However, most existing inorganic perovskite compositions deviate from this ideal bandgap range, leading to inadequate photon absorption and thus restricting the enhancement of J_{sc}.

Specifically, $CsPbBr_3$ possesses a bandgap of around 2.30 eV, restricting its absorption to the short-wavelength UV-visible region below 540 nm and yielding extremely low photon utilization in the 540-800 nm range, which typically limits J_{sc} to below 10 $mA{\cdot}cm^{-2}$[239]. α-phase $CsPbI_3$ exhibits a bandgap of ~1.73 eV, extending absorption to 715 nm. However, it spontaneously transforms into thermodynamically stable δ-phase at ambient conditions, and fails to efficiently capture near-infrared light beyond 700 nm[22-24]. While $CsSnI_3$ features a NBG (~1.30 eV) that covers the near-infrared up to 950 nm, it undergoes severe photo-oxidation degradation. Meanwhile, its NBG results in a low V_{oc}, posing significant challenges to the overall photovoltaic efficiency trade-off[240]. Apart from the bandgap limitation, inorganic perovskites exhibit strong ionic bonding, which can lead to uneven crystallization during film preparation and generate abundant crystal defects (such as vacancies and grain boundaries). These defects accelerate photogenerated carrier recombination and weaken the kinetics of carrier separation and transport. Collectively, these factors result in inferior efficiency of IPSCs compared with organic-inorganic hybrid PSCs.

By halogen substitution or bimetallic cation alloying, the bandgap of inorganic perovskites can be precisely tuned in the range of 1.27-2.3 eV. This implies that inorganic perovskites can be used to construct all-inorganic perovskite TSCs, thereby breaking the efficiency bottleneck[20]. For example, our group has successfully fabricated a 2T all-inorganic perovskite TSC with an efficiency of 22.54%, confirming its promising potential[20]. Despite the efficiency of hybrid perovskite TSCs exceeding 30% at present, these devices suffer from poor operational stability and photothermal aging stability. The core degradation mechanisms are summarized as follows: (1) WBG hybrid perovskite subcells are susceptible to photothermal-triggered phase separation; (2) Sn^{2+} in NBG perovskites is easily oxidized to Sn^{4+}; (3) Organic components of hybrid perovskites decompose rapidly under high temperature conditions; (4) Ion migration leads to irreversible perovskite decomposition. Accordingly, reported hybrid perovskite TSCs are merely evaluated via room-temperature photostability tests. In contrast, the 2T all-inorganic perovskite TSCs exhibit excellent photothermal stability, suggesting that constructing 2T all-inorganic perovskite TSCs is a feasible strategy to synchronously improve device efficiency and address long-term stability bottlenecks[20].

However, all-inorganic perovskite TSCs still face numerous scientific and technical challenges to achieve high efficiency and long-term stability. WBG inorganic perovskite subcells suffer from severe V_{oc} loss, which directly restricts the improvement of the PCE of tandem devices. Meanwhile, NBG inorganic perovskites are plagued by rapid crystallization kinetics, poor process controllability, easy oxidation of Sn^{2+} to Sn^{4+}, and high intrinsic trap density, which severely limit the performance ceiling of TSCs[52]. In addition, the photothermal aging mechanism of inorganic perovskite TSCs is more intricate, governed by the synergistic effects of interfaces, bulk phases, and interlayer coupling of WBG and NBG subcells.

Large-scale film fabrication

At present, high-quality all-inorganic perovskite films are predominantly limited to small-area laboratory samples (< 1 cm^2), whereas scalable manufacturing techniques (such as blade-coating, spray-coating, slot-die coating) are still immature. Such large-scale methods often cause uneven film thickness, component segregation, and increased defect density, resulting in poor batch-to-batch reproducibility and hindering industrial translation of IPSCs.

Blade-coating stands out as a promising large-scale manufacturing technology, yet it demands precise regulation of precursor ink rheological properties and substrate uniformity. Heo and colleagues reported that during blade-coating deposition of $CsPbI_{3-x}Br_x$ films, inadequate control of ink viscosity (below 500 cP) generates numerous pinholes and over 20% film thickness deviation[205]. After adding 0.5 wt% polyethylene glycol (PEG) to tune the ink viscosity to 1,000 cP and optimizing the blade-coating speed to 5 cm/s, uniform perovskite films with thickness deviation below 5% were obtained on 10 cm^2 × 10 cm^2 substrates. Nevertheless, the corresponding efficiency of large-area modules is still about 20% lower than that of small-area devices, primarily due to accelerated solvent evaporation at the edges, which triggers undesirable component segregation in large-area films.

Furthermore, the fabrication of large-scale inorganic perovskite films under ambient conditions is extremely susceptible to temperature, humidity, and other environmental factors, leading to inferior crystallinity, increased surface roughness, facile phase transition, and poor uniformity, thereby degrading device performance. Atmospheric moisture reacts with perovskite precursors to generate hydrated intermediates, which distort the stoichiometric ratio and disrupt the normal crystallization pathway, thereby favoring the formation of the yellow δ-phase rather than the desired α-phase. Meanwhile, oxygen in the air can oxidize metal cations within the perovskite lattice (such as Sn^{2+} oxidized into Sn^{4+}), inducing material degradation and lowering both film quality and operational stability. Wang *et al.* innovatively proposed a synergistic *in situ* hydrolysis polymerization strategy, using two organic silane molecules [3,3,3-(trifluoropropyl)trichlorosilane (TFCS) and (3-2-aminoethylamino)propyltrimethoxysilane (AEMS)] to treat the $CsPbI_3$ film surface. This strategy enables the preparation of high-performance inverted IPSCs under 45%-60% high-humidity ambient conditions. Based on this strategy, an IPSC with an efficiency of up to 20.09% was successfully produced under 45% ambient humidity[241].

Inorganic perovskites possess photothermal stability and negligible thermal volatility, endowing them with unique merits for extreme-scenario applications such as in aerospace. Although inorganic perovskite TSCs can improve photovoltaic efficiency, the research progress of multi-junction tandem architectures lags far behind that of single-junction IPSCs. Most studies to date have concentrated on hybrid tandem configurations, while all-inorganic perovskite TSCs still confront key scientific and technical challenges, including poor film processability, intrinsic phase instability, and mismatched subcell current density. Through advances in additive engineering, solvent system optimization, interface engineering, and fabrication techniques, targeted optimization of film deposition and intrinsic stability is expected to systematically boost the optoelectronic performance of both single-junction and tandem IPSCs.

Meanwhile, the research on all-inorganic perovskite photovoltaic technology in terms of long-term durability and large-scale manufacturing still lags behind that of hybrid perovskite devices. Encapsulation technology serves as a key strategy to reinforce device longevity by effectively preventing moisture and oxygen penetration. However, current investigations insufficiently address the correlations among encapsulation material systems, fabrication processes, and the long-term stability of IPSCs. Therefore, conducting in-depth research on the intrinsic mechanisms of encapsulation materials and processes, and developing new non-destructive encapsulation materials, is of vital importance for enhancing the stability and environmental adaptability of IPSCs.

In addition, research on the large-scale production of IPSCs and the toxicity of related solvents is relatively scarce. Future efforts should prioritize the development of eco-friendly, low-temperature, rapid-annealing, scalable deposition methods to realize high-efficiency devices compatible with industrial mass production. Despite the remaining formidable challenges, inorganic perovskites with low cost, exceptional photothermal stability, and favorable manufacturing scalability represent highly competitive candidates for next-generation photovoltaic technologies.

CONCLUSION AND OUTLOOK

This review systematically summarizes the research progress, core challenges, and prospective opportunities in all-inorganic perovskite photovoltaics, aiming to provide a comprehensive reference for advancing the commercialization of this promising photovoltaic technology. It elaborates on the fundamental properties of inorganic perovskites, mainstream film preparation techniques, and multiple performance optimization strategies, while analyzing their frontier applications in large-area modules, TSCs, and flexible devices. Furthermore, we deeply discuss the key bottlenecks restricting the commercialization of IPSCs, such as phase instability, efficiency ceiling, and large-scale manufacturing obstacles. With the continuous innovation of material modification, interface engineering, and low-cost large-area manufacturing technologies, all-inorganic perovskite photovoltaics are expected to break through current limitations, achieve stable, high-efficiency, and scalable industrial applications, and become a core component of next-generation renewable energy photovoltaic systems.

DECLARATIONS

Acknowledgements

The Graphical Abstract includes elements: Fundamental properties[57], permission from Ref.[57], Copyright © 2016 American Chemical Society. Preparation method[19,74,87], reprinted from Ref.[19] under the CC BY 4.0 license; permission from Ref.[74], Copyright © 2018 Elsevier; permission from Ref.[87], Copyright © 2022 Wiley-VCH. Improvement strategy[114,146], permission from Ref.[114], Copyright © 2020 The Royal Society of Chemistry; permission from Ref.[146], Copyright © 2020 American Chemical Society. Application filed[20,205,221], permission from Ref.[20], Copyright © 2025 Springer Nature; permission from Ref.[205], Copyright © 2021 Elsevier; Reprinted from Ref.[221] under the CC BY 4.0 license.

Authors' contributions

Conceptualization and manuscript design: Qu, Y.; Gao, K.; Zhu, Q.; Luo, H.
Figure preparation and manuscript writing: Qu, Y.; Xing, L.; Cui, Y.; Liu, M.
Manuscript discussion: Qu, Y.; Li, J.; Yan, K.; Duan. C.
Manuscript editing and polishing: Li, J.; Yan, K.; Duan. C.

Availability of data and materials

Not applicable.

AI and AI-assisted tools statement

Not applicable.

Financial support and sponsorship

This work was in part supported by the funds from the National Key Research and Development Program of China (2022YFB3803305), the National Natural Science Foundation of China (22578097), the Natural Science Foundation of Henan Province (262300421176), the Henan Provincial Selective Research Funding Program for Returned Scholars Studying Abroad (HNLX202644), and the Guangdong Science and Technology Program (2024A1515011154).

Conflict of interest

All authors declared that there are no conflicts of interest.

Ethical approval and consent to participate

Not applicable.

Consent for publication

Not applicable.

REFERENCES

1. Kojima, A.; Teshima, K.; Shirai, Y.; Miyasaka, T. Organometal halide perovskites as visible-light sensitizers for photovoltaic cells. *J. Am. Chem. Soc.* **2009**, *131*, 6050-1. DOI PubMed
2. National Laboratory of the Rockies. Best research-cell efficiency chart. Available online: https://www.nlr.gov/pv/cell-efficiency. (accessed 2026-07-01).
3. Eperon, G. E.; Stranks, S. D.; Menelaou, C.; Johnston, M. B.; Herz, L. M.; Snaith, H. J. Formamidinium lead trihalide: a broadly tunable perovskite for efficient planar heterojunction solar cells. *Energy. Environ. Sci.* **2014**, *7*, 982. DOI
4. Miyata, A.; Mitioglu, A.; Plochocka, P.; et al. Direct measurement of the exciton binding energy and effective masses for charge carriers in organic-inorganic tri-halide perovskites. *Nat. Phys.* **2015**, *11*, 582-7. DOI
5. Stranks, S. D.; Eperon, G. E.; Grancini, G.; et al. Electron-hole diffusion lengths exceeding 1 micrometer in an organometal trihalide perovskite absorber. *Science* **2013**, *342*, 341-4. DOI PubMed
6. Chen, Z.; Dong, Q.; Liu, Y.; et al. Thin single crystal perovskite solar cells to harvest below-bandgap light absorption. *Nat. Commun.* **2017**, *8*, 1890. DOI PubMed PMC
7. Zhang, Z.; Zhu, R.; Li, G.; et al. Photoswitchable isomers to improve grain boundary resilience and perovskite solar cells stability under light cycling. *Nat. Energy.* **2026**, *11*, 623-32. DOI PubMed PMC
8. Yang, Y.; Cheng, S.; Yang, X.; et al. Hafnium oxide interface stabilization for efficient, photothermally stable perovskite solar cells. *Science* **2026**, *391*, 926-30. DOI
9. Xiong, Z.; Zhang, Q.; Cai, K.; et al. Homogenized chlorine distribution for >27% power conversion efficiency in perovskite solar cells. *Science* **2025**, *390*, 638-42. DOI PubMed
10. Peng, Z.; Vincze, A.; Streller, F.; et al. Revealing degradation mechanisms in 3D/2D perovskite solar cells under photothermal accelerated ageing. *Energy. Environ. Sci.* **2024**, *17*, 8313-24. DOI
11. Luo, J.; Liu, B.; Yin, H.; et al. Polymer-acid-metal quasi-ohmic contact for stable perovskite solar cells beyond a 20,000-hour extrapolated lifetime. *Nat. Commun.* **2024**, *15*, 2002. DOI PubMed PMC
12. Zhang, W.; Guo, X.; Cui, Z.; et al. Strategies for improving efficiency and stability of inverted perovskite solar cells. *Adv. Mater.* **2024**, *36*, e2311025. DOI PubMed
13. Smecca, E.; Numata, Y.; Deretzis, I.; et al. Stability of solution-processed $MAPbI_3$ and $FAPbI_3$ layers. *Phys. Chem. Chem. Phys.* **2016**, *18*, 13413-22. DOI PubMed
14. Ruellou, J.; Courty, M.; Sauvage, F. Thermal and photo-degradation study of α-$FAPbI_3$-based perovskite using in situ X-ray diffraction. *Adv. Funct. Mater.* **2023**, *33*, 2300811. DOI
15. Di Girolamo, D.; Phung, N.; Kosasih, F. U.; et al. Ion migration-induced amorphization and phase segregation as a degradation mechanism in planar perovskite solar cells. *Adv. Energy. Mater.* **2020**, *10*, 2000310. DOI
16. Kim, T.; Park, S.; Iyer, V.; et al. Mapping the pathways of photo-induced ion migration in organic-inorganic hybrid halide perovskites. *Nat. Commun.* **2023**, *14*, 1846. DOI PubMed PMC

17. Zhao, X.; Liu, T.; Burlingame, Q. C.; et al. Accelerated aging of all-inorganic, interface-stabilized perovskite solar cells. *Science* **2022**, *377*, 307-10. DOI PubMed
18. Wu, L.; Li, G.; Prashanthan, K.; et al. Stabilization of inorganic perovskite solar cells with a 2D dion-jacobson passivating layer. *Adv. Mater.* **2023**, *35*, 2304150. DOI
19. Wang, P.; Zhang, X.; Zhou, Y.; et al. Solvent-controlled growth of inorganic perovskite films in dry environment for efficient and stable solar cells. *Nat. Commun.* **2018**, *9*, 2225. DOI PubMed PMC
20. Duan, C.; Zhang, K.; Peng, Z.; et al. Durable all-inorganic perovskite tandem photovoltaics. *Nature* **2024**, *637*, 1111-7. DOI PubMed
21. He, R.; Ren, S.; Chen, C.; et al. Wide-bandgap organic-inorganic hybrid and all-inorganic perovskite solar cells and their application in all-perovskite tandem solar cells. *Energy. Environ. Sci.* **2021**, *14*, 5723-59. DOI
22. Sutton, R. J.; Filip, M. R.; Haghighirad, A. A.; et al. Cubic or orthorhombic? Revealing the crystal structure of metastable black-phase $CsPbI_3$ by theory and experiment. *ACS. Energy. Lett.* **2018**, *3*, 1787-94. DOI
23. Tan, S.; Yu, B.; Cui, Y.; et al. Temperature-reliable low-dimensional perovskites passivated black-phase $CsPbI_3$ toward stable and efficient photovoltaics. *Angew. Chem. Int. Ed.* **2022**, *61*, e202201300. DOI PubMed
24. Kweon, K. E.; Varley, J.; Ogitsu, T.; et al. Influence of external conditions on the black-to-yellow phase transition of $CsPbI_3$ based on first-principles calculations: pressure and moisture. *Chem. Mater.* **2023**, *35*, 2321-9. DOI
25. Ding, Y.; Guo, Q.; Geng, Y.; et al. A low-cost hole transport layer enables $CsPbI_2Br$ single-junction and tandem perovskite solar cells with record efficiencies of 17.8 % and 21.4 %. *Nano. Today.* **2022**, *46*, 101586. DOI
26. Lim, E. L.; Yang, J.; Wei, Z. Inorganic $CsPbI_2Br$ halide perovskites: from fundamentals to solar cell optimizations. *Energy. Environ. Sci.* **2023**, *16*, 862-88. DOI
27. Park, J. H.; Yoon, Y. S.; Kim, J. Y. Fabrication processes for all-inorganic $_3$ perovskite solar cells. *EcoMat* **2023**, *5*, e12407. DOI
28. Yao, Z.; Xu, Z.; Zhao, W.; et al. Enhanced efficiency of inorganic $CsPbI_{3-x}Br_x$ perovskite solar cell via self-regulation of antisite defects. *Adv. Energy. Mater.* **2021**, *11*, 2100403. DOI
29. Yue, S.; Long, Q.; Li, T.; et al. Recent progress on mitigating open-circuit voltage loss in inorganic $CsPbX_3$ perovskite solar cells. *ChemSusChem* **2025**, *18*, e202500428. DOI
30. Ke, W.; Spanopoulos, I.; Stoumpos, C. C.; Kanatzidis, M. G. Myths and reality of $HPbI_3$ in halide perovskite solar cells. *Nat. Commun.* **2018**, *9*, 4785. DOI PubMed PMC
31. Wang, Y.; Dar, M. I.; Ono, L. K.; et al. Thermodynamically stabilized β-$CsPbI_3$-based perovskite solar cells with efficiencies >18%. *Science* **2019**, *365*, 591-5. DOI PubMed
32. Swarnkar, A.; Mir, W. J.; Nag, A. Can B-site doping or alloying improve thermal- and phase-stability of all-inorganic $CsPbX_3$ (X = Cl, Br, I) perovskites? *ACS. Energy. Lett.* **2018**, *3*, 286-9. DOI
33. Li, B.; Zhang, Y.; Fu, L.; et al. Surface passivation engineering strategy to fully-inorganic cubic CsPbI3 perovskites for high-performance solar cells. *Nat. Commun.* **2018**, *9*, 1076. DOI PubMed PMC
34. Xu, T.; Xiang, W.; Yang, J.; et al. Interface modification for efficient and stable inverted inorganic perovskite solar cells. *Adv. Mater.* **2023**, *35*, 2303346. DOI PubMed
35. Kulbak, M.; Cahen, D.; Hodes, G. How important is the organic part of lead halide perovskite photovoltaic cells? Efficient $CsPbBr_3$ cells. *J. Phys. Chem. Lett.* **2015**, *6*, 2452-6. DOI PubMed
36. Sanehira, E. M.; Marshall, A. R.; Christians, J. A.; et al. Enhanced mobility $CsPbI_3$ quantum dot arrays for record-efficiency, high-voltage photovoltaic cells. *Sci. Adv.* **2017**, *3*, eaao4204. DOI
37. Wang, Y.; Zhang, T.; Kan, M.; Zhao, Y. Bifunctional stabilization of all-inorganic α-$CsPbI_3$ perovskite for 17% efficiency photovoltaics. *J. Am. Chem. Soc.* **2018**, *140*, 12345-8. DOI
38. Gu, X.; Xiang, W.; Tian, Q.; Liu, S. Rational surface-defect control via designed passivation for high-efficiency inorganic perovskite solar cells. *Angew. Chem. Int. Ed.* **2021**, *60*, 23164-70. DOI PubMed
39. Zhang, H.; Xiang, W.; Zuo, X.; et al. Fluorine-containing passivation layer via surface chelation for inorganic perovskite solar cells. *Angew. Chem. Int. Ed.* **2022**, *62*, e202216634. DOI PubMed
40. Zhang, H.; Tian, Q.; Xiang, W.; et al. Tailored cysteine-derived molecular structures toward efficient and stable inorganic perovskite solar cells. *Adv. Mater.* **2023**, *35*, e2301140. DOI PubMed
41. Li, R.; Zhang, S.; Zhang, H.; et al. Customizing aniline-derived molecular structures to attain beyond 22 % efficient inorganic perovskite solar cells. *Angew. Chem. Int. Ed.* **2024**, e202410600. DOI PubMed
42. Li, R.; Chen, Q.; Zhang, H.; et al. Simultaneous charge extraction enhancement and defect passivation via a planar conjugated molecular interface enable 22.49%-efficient inorganic perovskite solar cells. *Angew. Chem. Int. Ed.* **2025**, *64*, e202510925. DOI

43. Yang, M.; Wang, H.; Cai, W.; Zang, Z. Mixed-halide inorganic perovskite solar cells: opportunities and challenges. *Adv. Opt. Mater.* **2023**, *11*, 2301052. DOI
44. Li, C.; Lu, X.; Ding, W.; et al. Formability of ABX3 (X= F, Cl, Br, I) halide perovskites. *Acta. Crystallogr. B.* **2008**, *64*, 702-7. DOI PubMed
45. Jena, A. K.; Kulkarni, A.; Miyasaka, T. Halide perovskite photovoltaics: background, status, and future prospects. *Chem. Rev.* **2019**, *119*, 3036-103. DOI PubMed
46. Goldschmidt, V. M. Die gesetze der krystallochemie. *Naturwissenschaften* **1926**, *14*, 477-85. DOI
47. Sun, Q.; Yin, W. Thermodynamic stability trend of cubic perovskites. *J. Am. Chem. Soc.* **2017**, *139*, 14905-8. DOI PubMed
48. Yang, R.; Yang, D.; Liu, S. F. High-performance all-inorganic cesium halide perovskite solar cells. *Chem. Rev.* **2026**, *126*, 1408-69. DOI PubMed
49. Zhang, J.; Jin, Z.; Liang, L.; et al. Iodine-optimized interface for inorganic $CsPbI_2Br$ perovskite solar cell to attain high stabilized efficiency exceeding 14%. *Adv. Sci.* **2018**, *5*, 1801123. DOI PubMed PMC
50. Wu, X.; Wang, S.; Zhang, J.; et al. Bypassing the non-perovskite yellow phase: revealing and regulating the crystallization pathways for efficient all-inorganic perovskite solar cells. *Nano. Energy.* **2023**, *117*, 108907. DOI
51. Zhang, X.; Zhang, D.; Wang, Z.; Zhao, Y.; Chen, H. All-inorganic tin-containing perovskite solar cells: an emerging eco-friendly photovoltaic technology. *Adv. Mater.* **2025**, *37*, 2505543. DOI PubMed
52. Duan, C.; Hu, M.; Zhu, Q.; et al. Tuning the crystallization and photothermal aging chemistry of $CsPb_{0.4}Sn_{0.6}I_3$ for inorganic perovskite tandem photovoltaics. *Angew. Chem. Int. Ed.* **2025**, *64*, e202507761. DOI PubMed
53. Jbara, A. S.; Munir, J.; Ul Haq, B.; Saeed, M. A. Density functional theory study of mixed halide influence on structures and optoelectronic attributes of $CsPb(I/Br)_3$. *Appl. Opt.* **2020**, *59*, 3751-9. DOI PubMed
54. Sutton, R. J.; Eperon, G. E.; Miranda, L.; et al. Bandgap-tunable cesium lead halide perovskites with high thermal stability for efficient solar cells. *Adv. Energy. Mater.* **2016**, *6*, 1502458. DOI
55. Ullah, S.; Khan, F.; Rasheed, J. F. Prospects for commercialization of $CsPbIBr_2$-based all-inorganic perovskite solar cells: fabrication, stability, and engineering strategies. *Adv. Funct. Mater.* **2025**, *35*, 2503508. DOI
56. Ghaithan, H. M.; Alahmed, Z. A.; Qaid, S. M.; Aldwayyan, A. S. First principle-based calculations of the optoelectronic features of 2 x 2 x 2 $CsPb(I_{1-x}Br_x)_3$ perovskite. *Superlattices. Microstruct.* **2020**, *140*, 106474. DOI
57. Ravi, V. K.; Markad, G. B.; Nag, A. Band edge energies and excitonic transition probabilities of colloidal $CsPbX_3$ (X = Cl, Br, I) perovskite nanocrystals. *ACS. Energy. Lett.* **2016**, *1*, 665-71. DOI
58. Chen, G.; Li, P.; Xue, T.; et al. Design of low bandgap $CsPb_{1-x}SnxI_2Br$ perovskite solar cells with excellent phase stability. *Small* **2021**, *17*, 2101380. DOI
59. Hu, S.; Thiesbrummel, J.; Pascual, J.; Stolterfoht, M.; Wakamiya, A.; Snaith, H. J. Narrow bandgap metal halide perovskites for all-perovskite tandem photovoltaics. *Chem. Rev.* **2024**, *124*, 4079-123. DOI PubMed PMC
60. Goyal, A.; Mckechnie, S.; Pashov, D.; Tumas, W.; Van Schilfgaarde, M.; Stevanović, V. Origin of pronounced nonlinear band gap behavior in lead-tin hybrid perovskite alloys. *Chem. Mater.* **2018**, *30*, 3920-8. DOI
61. Bandara, R. M. I.; Silva, S. M.; Underwood, C. C. L.; Jayawardena, K. D. G. I.; Sporea, R. A.; Silva, S. R. P. Progress of Pb-Sn mixed perovskites for photovoltaics: a review. *Energy. Environ. Mater.* **2021**, *5*, 370-400. DOI
62. Wen, Q.; Duan, C.; Zou, F.; et al. All-inorganic $CsPb_{1-x}Sn_xI_2Br$ perovskites mediated by dicyandiamide additive for efficient 4-terminal tandem solar cell. *Chem. Eng. J.* **2023**, *452*, 139697. DOI
63. Pai, N.; Angmo, D. Powering the future: opportunities and obstacles in lead-halide inorganic perovskite solar cells. *Advanced. Science.* **2025**, *12*, 2412666. DOI PubMed PMC
64. Liu, H.; Han, H.; Xu, J.; et al. A 0D additive for flexible all-inorganic perovskite solar cells to go beyond 60 000 flexible cycles. *Adv. Mater.* **2023**, *35*, e2300302. DOI PubMed
65. Liu, H.; Xu, J.; Han, H.; et al. Debridement strategy by pre-bending passivation for flexible all-inorganic perovskite solar cells beyond 70 000 bending cycles. *Adv. Funct. Mater.* **2024**, *34*, 2400975. DOI
66. Zhu, M.; Qin, L.; Xia, Y.; et al. Indium-doped $CsPbI_{2.5}Br_{0.5}$ with a tunable band structure and improved crystallinity for thermo-stable all-inorganic perovskite solar cells. *ACS. Appl. Energy. Mater.* **2023**, *6*, 8237-44. DOI
67. Li, X.; Wang, K.; Lgbari, F.; et al. Indium doped CsPbI3 films for inorganic perovskite solar cells with efficiency exceeding 17%. *Nano. Res.* **2020**, *13*, 2203-8. DOI
68. Singh, R. K.; Kumar, R.; Jain, N.; Dash, S. R.; Singh, J.; Srivastava, A. Investigation of optical and dielectric properties of $CsPbI_3$ inorganic lead iodide perovskite thin film. *J. Taiwan. Inst. Chem. Eng.* **2019**, *96*, 538-42. DOI
69. Maleka, P. M.; Dima, R. S.; Ntwaeaborwa, O. M.; et al. Density functional theory study of Br doped $CsPbI_3$ perovskite for photovoltaic and optoelectronic applications. *Phys. Scripta.* **2023**, *98*, 045505. DOI

70. Pintor Monroy, M. I.; Goldberg, I.; Elkhouly, K.; et al. All-evaporated, all-inorganic $CsPbI_3$ perovskite-based devices for broad-band photodetector and solar cell applications. *ACS. Appl. Electron. Mater.* **2021**, *3*, 3023-33. DOI PubMed PMC
71. Duan, C.; Li, J.; Liu, Z.; Wen, Q.; Tang, H.; Yan, K. Highly electroluminescent and stable inorganic $CsPbI_2Br$ perovskite solar cell enabled by balanced charge transfer. *Chem. Eng. J.* **2021**, *417*, 128053. DOI
72. Zhou, S.; Zhou, C.; Zhu, J.; et al. Enhanced field emission properties of $CsPbBr_3$ films by thermal annealing and surface functionalization with boron nitride. *Appl. Surf. Sci.* **2022**, *578*, 152116. DOI
73. Zhou, C.; Huang, Y.; Zhang, Y.; et al. $CsPbBr_3$ microarrays with tunable periodicity, optoelectronic and field emission properties using self-assembled polystyrene template and co-evaporation method. *Phys. Chem. Chem. Phys.* **2022**, *24*, 13210-6. DOI
74. Lei, J.; Gao, F.; Wang, H.; et al. Efficient planar $CsPbBr_3$ perovskite solar cells by dual-source vacuum evaporation. *Sol. Energy. Mater. Sol. Cells.* **2018**, *187*, 1-8. DOI
75. Lee, J. H.; Kim, B. S.; Park, J.; Lee, J. W.; Kim, K. Opportunities and challenges for perovskite solar cells based on vacuum thermal evaporation. *Adv. Mater. Technol.* **2022**, *8*, 2200928. DOI
76. Lau, C. F. J.; Deng, X.; Ma, Q.; et al. $CsPbIBr_2$ perovskite solar cell by spray-assisted deposition. *ACS. Energy. Lett.* **2016**, *1*, 573-7. DOI
77. Tai, Q.; Tang, K.; Yan, F. Recent progress of inorganic perovskite solar cells. *Energy. Environ. Sci.* **2019**, *12*, 2375-405. DOI
78. Mali, S. S.; Patil, J. V.; Hong, C. K. Hot-air-assisted fully air-processed barium incorporated $CsPbI_2Br$ perovskite thin films for highly efficient and stable all-inorganic perovskite solar cells. *Nano. Lett.* **2019**, *19*, 6213-20. DOI PubMed
79. Mali, S. S.; Patil, J. V.; Shinde, P. S.; De Miguel, G.; Hong, C. K. Fully air-processed dynamic hot-air-assisted M:$CsPbI_2Br$ (M: Eu^{2+}, In^{3+}) for stable inorganic perovskite solar cells. *Matter* **2021**, *4*, 635-53. DOI
80. Abate, S. Y.; Qi, Y.; Zhang, Q.; et al. Eco-friendly solvent engineered $CsPbI_{2.77}Br_{0.23}$ Ink for large-area and scalable high performance perovskite solar cells. *Adv. Mater.* **2023**, *36*, 2310279. DOI PubMed
81. Wang, J.; Che, Y.; Duan, Y.; et al. 21.15%-efficiency and stable γ -$CsPbI_3$ perovskite solar cells enabled by an acyloin ligand. *Adv. Mater.* **2023**, *35*, 2210223. DOI
82. Song, J.; Xie, H.; Lim, E. L.; Hagfeldt, A.; Bi, D. Progress and perspective on inorganic $CsPbI_2Br$ perovskite solar cells. *Adv. Energy. Mater.* **2022**, *12*, 2201854. DOI
83. Feng, J.; Han, X.; Huang, H.; et al. Curing the fundamental issue of impurity phases in two-step solution-processed $CsPbBr_3$ perovskite films. *Sci. Bull.* **2020**, *65*, 726-37. DOI PubMed
84. Zeng, Z.; Zhang, J.; Gan, X.; et al. In situ grain boundary functionalization for stable and efficient inorganic $CsPbI_2Br$ perovskite solar cells. *Adv. Energy. Mater.* **2018**, *8*, 1801050. DOI
85. Han, Y.; Xie, H.; Lim, E. L.; Bi, D. Review of two-step method for lead halide perovskite solar cells. *Solar. RRL.* **2022**, *6*, 2101007. DOI
86. Liu, X.; Tan, X.; Liu, Z.; et al. Boosting the efficiency of carbon-based planar $CsPbBr_3$ perovskite solar cells by a modified multistep spin-coating technique and interface engineering. *Nano. Energy.* **2019**, *56*, 184-95. DOI
87. Zhu, W.; Ma, J.; Chai, W.; et al. Intermediate phase-assisted sequential deposition toward 15.24%-efficiency carbon-electrode $cspbi_2br$ perovskite solar cells. *Solar. RRL.* **2022**, *6*, 2200020. DOI
88. Liu, Z.; Jung, H.; Sotome, M.; et al. Substrate temperature dependence of vapor-phase deposition of all-inorganic lead-free $CsSnBr_3$ perovskite thin films. *Jpn. J. Appl. Phys.* **2024**, *63*, 02SP23. DOI
89. Bai, T.; Wang, S.; Bai, L.; Zhang, K.; Chu, C.; Yi, L. Vacuum evaporation of high-quality $CsPbBr_3$ thin films for efficient light-emitting diodes. *Nanoscale. Res. Lett.* **2022**, *17*, 69. DOI PubMed PMC
90. Huang, J.; Yao, H.; You, F.; et al. Effects of post-annealing on the property of $CsPbBr_3$ films and the performance of relevant light-emitting diodes. *J. Lumin.* **2024**, *275*, 120771. DOI
91. Zhang, Y.; Huang, Y.; Zhou, C.; Xu, Y.; Zhong, J.; Mao, H. Crystalline structures and optoelectronic properties of orthorhombic $CsPbBr_3$ polycrystalline films grown by the Co-evaporation method. *Vacuum* **2022**, *202*, 111219. DOI
92. Li, J.; Gao, R.; Gao, F.; et al. Fabrication of efficient $CsPbBr_3$ perovskite solar cells by single-source thermal evaporation. *J. Alloys. Compd.* **2020**, *818*, 152903. DOI
93. Ullah, S.; Wang, J.; Yang, P.; et al. All-inorganic $CsPbBr_3$ perovskite: a promising choice for photovoltaics. *Mater. Adv.* **2021**, *2*, 646-83. DOI
94. He, Z.; Peng, C.; Guo, R.; et al. High-efficiency and emission-tunable inorganic blue perovskite light-emitting diodes based on vacuum deposition. *Small* **2023**, *20*, 2305379. DOI PubMed
95. Liu, X.; Tan, X.; Liu, Z.; et al. Sequentially vacuum evaporated high-quality $CsPbBr_3$ films for efficient carbon-based planar heterojunction perovskite solar cells. *J. Power. Sources.* **2019**, *443*, 227269. DOI

96. Abbasli, M.; Hieulle, J.; Schrage, J.; et al. Tin halide perovskite epitaxial films on gold surfaces: atomic structure and stability. *Adv. Funct. Mater.* **2024**, *34*, 2403680. DOI
97. Ritzer, D. B.; Abzieher, T.; Basibüyük, A.; et al. Upscaling of perovskite solar modules: the synergy of fully evaporated layer fabrication and all-laser-scribed interconnections. *Prog. Photovolt.* **2021**, *30*, 360-73. DOI
98. Liu, T.; Zhao, X.; Wang, P.; et al. Highly transparent, scalable, and stable perovskite solar cells with minimal aesthetic compromise. *Adv. Energy. Mater.* **2022**, *13*, 2200402. DOI
99. Piot, M.; Alonso, J. E. S.; Zanoni, K. P. S.; et al. Fast coevaporation of 1 µm thick perovskite solar cells. *ACS. Energy. Lett.* **2023**, *8*, 4711-3. DOI PubMed PMC
100. Kosasih, F. U.; Erdenebileg, E.; Mathews, N.; Mhaisalkar, S. G.; Bruno, A. Thermal evaporation and hybrid deposition of perovskite solar cells and mini-modules. *Joule* **2022**, *6*, 2692-734. DOI
101. Haruta, Y.; Ikenoue, T.; Miyake, M.; Hirato, T. One-step coating of full-coverage $CsPbBr_3$ thin films via mist deposition for all-inorganic perovskite solar cells. *ACS. Appl. Energy. Mater.* **2020**, *3*, 11523-8. DOI
102. Liu, X.; Li, J.; Liu, Z.; et al. Vapor-assisted deposition of $CsPbIBr_2$ films for highly efficient and stable carbon-based planar perovskite solar cells with superior V_{oc}. *Electrochim. Acta.* **2020**, *330*, 135266. DOI
103. Li, X.; Tan, Y.; Lai, H.; et al. All-inorganic $CsPbBr_3$ perovskite solar cells with 10.45% efficiency by evaporation-assisted deposition and setting intermediate energy levels. *ACS. Appl. Mater. Interfaces.* **2019**, *11*, 29746-52. DOI PubMed
104. Duan, J.; Dou, D.; Zhao, Y.; et al. Spray-assisted deposition of $CsPbBr_3$ films in ambient air for large-area inorganic perovskite solar cells. *Mater. Today. Energy.* **2018**, *10*, 146-52. DOI
105. Näsström, H.; Becker, P.; Márquez, J. A.; et al. Dependence of phase transitions on halide ratio in inorganic $CsPb(BrxIx)_3$ perovskite thin films obtained from high-throughput experimentation. *J. Mater. Chem. A.* **2020**, *8*, 22626-31. DOI
106. Ye, Q.; Zhao, Y.; Mu, S.; et al. Cesium lead inorganic solar cell with efficiency beyond 18% via reduced charge recombination. *Adv. Mater.* **2019**, *31*, 1905143. DOI
107. Cheng, J.; Mu, Y.; Wu, L.; et al. Acetate-assistant efficient cation-exchange of halide perovskite nanocrystals to boost the photocatalytic CO_2 reduction. *Nano. Res.* **2021**, *15*, 1845-52. DOI
108. Zhao, H.; Han, Y.; Xu, Z.; et al. A novel anion doping for stable $CsPbI_2Br$ perovskite solar cells with an efficiency of 15.56% and an open circuit voltage of 1.30 V. *Adv. Energy. Mater.* **2019**, *9*, 1902279. DOI
109. Lou, Y.; Niu, Y.; Yang, D.; et al. Rod-shaped thiocyanate-induced abnormal band gap broadening in SCN- doped CsPbBr3 perovskite nanocrystals. *Nano. Res.* **2018**, *11*, 2715-23. DOI
110. Zhang, Z.; Chen, W.; Jiang, X.; et al. Suppression of phase segregation in wide-bandgap perovskites with thiocyanate ions for perovskite/organic tandems with 25.06% efficiency. *Nat. Energy.* **2024**, *9*, 592-601. DOI
111. Wu, H.; Yang, Y.; Zhou, D.; et al. Rb^+ cations enable the change of luminescence properties in perovskite ($Rb_xCs_{1-x}PbBr_3$) quantum dots. *Nanoscale* **2018**, *10*, 3429-37. DOI
112. Nam, J. K.; Chai, S. U.; Cha, W.; et al. Potassium incorporation for enhanced performance and stability of fully inorganic cesium lead halide perovskite solar cells. *Nano. Lett.* **2017**, *17*, 2028-33. DOI PubMed
113. Lu, M.; Zhang, X.; Bai, X.; et al. Spontaneous silver doping and surface passivation of $CsPbI_3$ perovskite active layer enable light-emitting devices with an external quantum efficiency of 11.2%. *ACS. Energy. Lett.* **2018**, *3*, 1571-7. DOI PubMed PMC
114. Shi, J.; Li, F.; Yuan, J.; et al. Efficient and stable $CsPbI_3$ perovskite quantum dots enabled by *in situ* ytterbium doping for photovoltaic applications. *J. Mater. Chem. A.* **2019**, *7*, 20936-44. DOI
115. Karunakaran, S. K.; Arumugam, G. M.; Yang, W.; et al. Europium (II)-doped all-inorganic $CsPbBr_3$ perovskite solar cells with carbon electrodes. *Solar. RRL.* **2020**, *4*, 2000390. DOI
116. Zhao, Y.; Wang, Y.; Duan, J.; Yang, X.; Tang, Q. Divalent hard Lewis acid doped $CsPbBr_3$ films for 9.63%-efficiency and ultra-stable all-inorganic perovskite solar cells. *J. Mater. Chem. A.* **2019**, *7*, 6877-82. DOI
117. Lau, C. F. J.; Deng, X.; Zheng, J.; et al. Enhanced performance *via* partial lead replacement with calcium for a $CsPbI_3$ perovskite solar cell exceeding 13% power conversion efficiency. *J. Mater. Chem. A.* **2018**, *6*, 5580-6. DOI
118. Chen, J.; Ma, J.; Guo, S.; et al. High-efficiency violet-emitting all-inorganic perovskite nanocrystals enabled by alkaline-earth metal passivation. *Chem. Mater.* **2019**, *31*, 3974-83. DOI
119. Lau, C. F. J.; Zhang, M.; Deng, X.; et al. Strontium-doped low-temperature-processed $CsPbI_2Br$ perovskite solar cells. *ACS. Energy. Lett.* **2017**, *2*, 2319-25. DOI
120. Liu, F.; Ding, C.; Zhang, Y.; et al. Colloidal synthesis of air-stable alloyed $CsSnxPbxI_3$ perovskite nanocrystals for use in solar cells. *J. Am. Chem. Soc.* **2017**, *139*, 16708-19. DOI PubMed

121. Jin, H.; Zeng, Y.; Steele, J. A.; Roeffaers, M. B. J.; Hofkens, J.; Debroye, E. Phase stabilization of cesium lead iodide perovskites for use in efficient optoelectronic devices. *NPG. Asia. Mater.* **2024**, *16*, 24. DOI PubMed PMC
122. Liang, J.; Zhao, P.; Wang, C.; et al. $CsPb_{0.9}Sn_{0.1}IBr_2$ based all-inorganic perovskite solar cells with exceptional efficiency and stability. *J. Am. Chem. Soc.* **2017**, *139*, 14009-12. DOI PubMed
123. Tang, M.; He, B.; Dou, D.; et al. Toward efficient and air-stable carbon-based all-inorganic perovskite solar cells through substituting $CsPbBr_3$ films with transition metal ions. *Chem. Eng. J.* **2019**, *375*, 121930. DOI
124. Zhang, L.; Kang, C.; Zhang, G.; et al. All-inorganic $CsPbI_3$ quantum dot solar cells with efficiency over 16% by defect control. *Adv. Funct. Mater.* **2020**, *31*, 2005930. DOI
125. Liang, J.; Liu, Z.; Qiu, L.; et al. Enhancing optical, electronic, crystalline, and morphological properties of cesium lead halide by Mn substitution for high-stability all-inorganic perovskite solar cells with carbon electrodes. *Adv. Energy. Mater.* **2018**, *8*, 1800504. DOI
126. Öz, S.; Burschka, J.; Jung, E.; et al. Protic ionic liquid assisted solution processing of lead halide perovskites with water, alcohols and acetonitrile. *Nano. Energy.* **2018**, *51*, 632-8. DOI
127. Hamill, J. C.; Schwartz, J.; Loo, Y. Influence of solvent coordination on hybrid organic-inorganic perovskite formation. *ACS. Energy. Lett.* **2017**, *3*, 92-7. DOI
128. Zhang, X.; Yu, Z.; Zhang, D.; et al. Recent progress of carbon-based inorganic perovskite solar cells: from efficiency to stability. *Adv. Energy. Mater.* **2023**, *13*, 2201320. DOI
129. Jiang, Y.; Yuan, J.; Ni, Y.; et al. Reduced-dimensional α-$CsPbX_3$ perovskites for efficient and stable photovoltaics. *Joule* **2018**, *2*, 1356-68. DOI
130. Wang, H.; Sun, J.; Gu, Y.; et al. Solvent-engineering-processed $CsPbIBr_2$ inorganic perovskite solar cells with efficiency of ~11%. *Sol. Energy. Mater. Sol. Cells.* **2022**, *238*, 111640. DOI
131. Oh, J.; Kim, S. H.; Choi, S.; et al. Enhancing performance and stability of perovskite solar cells via $CsPbBr_3$ nanocrystal-assisted antisolvent engineering. *Curr. Appl. Phys.* **2025**, *71*, 37-45. DOI
132. Taylor, A. D.; Sun, Q.; Goetz, K. P.; et al. A general approach to high-efficiency perovskite solar cells by any antisolvent. *Nat. Commun.* **2021**, *12*, 1878. DOI PubMed PMC
133. Jeon, N. J.; Noh, J. H.; Kim, Y. C.; Yang, W. S.; Ryu, S.; Seok, S. I. Solvent engineering for high-performance inorganic-organic hybrid perovskite solar cells. *Nat. Mater.* **2014**, *13*, 897-903. DOI PubMed
134. Jiang, Y.; Deng, D.; Dong, J. Preparation of highly efficient and stable all-inorganic perovskite solar cells in atmosphere environment. *Energies*. **2025**, *18*, 2162. DOI
135. Dong, C.; Han, X.; Li, W.; Qiu, Q.; Wang, J. Anti-solvent assisted multi-step deposition for efficient and stable carbon-based $CsPbI_2Br$ all-inorganic perovskite solar cell. *Nano. Energy.* **2019**, *59*, 553-9. DOI
136. Chen, C.; Bala, H.; Yao, S.; et al. Enhanced efficiency and stability of perovskite solar cells based on carbon-counter-electrode via anti-solvent treatment. *J. Alloys. Compd.* **2022**, *920*, 165874. DOI
137. Zhang, N.; Zhang, Z.; Liu, T.; et al. Efficient and stable $MAPbI_3$ perovskite solar cells via green anti-solvent diethyl carbonate. *Org. Electron.* **2023**, *113*, 106709. DOI
138. Sanchez, S.; Christoph, N.; Grobety, B.; et al. Efficient and stable inorganic perovskite solar cells manufactured by pulsed flash infrared annealing. *Adv. Energy. Mater.* **2018**, *8*, 1802060. DOI
139. Zhang, B.; Bi, W.; Wu, Y.; et al. High-performance $CsPbIBr_2$ perovskite solar cells: effectively promoted crystal growth by antisolvent and organic ion strategies. *ACS. Appl. Mater. Interfaces.* **2019**, *11*, 33868-78. DOI
140. Hyun Park, S.; Su Jin, I.; Woong Jung, J. Green solvent engineering for environment-friendly fabrication of high-performance perovskite solar cells. *Chem. Eng. J.* **2021**, *425*, 131475. DOI
141. Moot, T.; Marshall, A. R.; Wheeler, L. M.; et al. CsI-antisolvent adduct formation in all-inorganic metal halide perovskites. *Adv. Energy. Mater.* **2020**, *10*, 1903365. DOI
142. Duan, C.; Wen, Q.; Fan, Y.; Li, J.; Liu, Z.; Yan, K. Improving the stability and scalability of all-inorganic inverted CsPbI2Br perovskite solar cell. *J. Energy. Chem.* **2022**, *68*, 176-83. DOI
143. Chen, W.; Chen, H.; Xu, G.; et al. Precise control of crystal growth for highly efficient $CsPbI_2Br$ perovskite solar cells. *Joule* **2019**, *3*, 191-204. DOI
144. Xia, J.; Liang, C.; Gu, H.; et al. Surface passivation toward efficient and stable perovskite solar cells. *Energy. Environ. Mater.* **2022**, *6*, e12296. DOI
145. Chung, Y.; Kim, K. S.; Jung, J. W. On the role of carboxylated polythiophene in defect passivation of $CsPbI_2$ Br surface for efficient and stableall-inorganic perovskite solar cells. *Intl. J. of. Energy. Research.* **2021**, *46*, 6012-21. DOI

146. Fu, S.; Wan, L.; Zhang, W.; Li, X.; Song, W.; Fang, J. Tailoring in situ healing and stabilizing post-treatment agent for high-performance inverted $CsPbI_3$ perovskite solar cells with efficiency of 16.67%. *ACS. Energy. Lett.* **2020**, *5*, 3314-21. DOI
147. Xiao, H.; Zuo, C.; Yan, K.; et al. Highly efficient and air-stable inorganic perovskite solar cells enabled by polylactic acid modification. *Adv. Energy. Mater.* **2023**, *13*, 2300738. DOI
148. Yoon, S. M.; Min, H.; Kim, J. B.; Kim, G.; Lee, K. S.; Seok, S. I. Surface engineering of ambient-air-processed cesium lead triiodide layers for efficient solar cells. *Joule* **2021**, *5*, 183-96. DOI
149. Wang, Y.; Zhang, T.; Kan, M.; Li, Y.; Wang, T.; Zhao, Y. Efficient α-$CsPbI_3$ photovoltaics with surface terminated organic cations. *Joule* **2018**, *2*, 2065-75. DOI
150. Yan, F.; Yang, P.; Li, J.; et al. Healing soft interface for stable and high-efficiency all-inorganic $CsPbIBr_2$ perovskite solar cells enabled by S-benzylisothiourea hydrochloride. *Chem. Eng. J.* **2022**, *430*, 132781. DOI
151. Fu, S.; Zhang, W.; Li, X.; et al. Dual-protection strategy for high-efficiency and stable $CsPbI_2Br$ inorganic perovskite solar cells. *ACS. Energy. Lett.* **2020**, *5*, 676-84. DOI
152. Wang, X.; Wang, Y.; Chen, Y.; Liu, X.; Zhao, Y. Efficient and stable $CsPbI_3$ inorganic perovskite photovoltaics enabled by crystal secondary growth. *Adv. Mater.* **2021**, *33*, 2103688. DOI PubMed
153. Bai, F.; Zhang, J.; Yuan, Y.; et al. A 0D/3D heterostructured all-inorganic halide perovskite solar cell with high performance and enhanced phase stability. *Adv. Mater.* **2019**, *31*, 1904735. DOI PubMed
154. Chen, Y.; Wang, X.; Wang, Y.; Liu, X.; Miao, Y.; Zhao, Y. Functional organic cation induced 3D-to-0D phase transformation and surface reconstruction of $CsPbI_3$ inorganic perovskite. *Sci. Bull.* **2023**, *68*, 706-12. DOI PubMed
155. Liu, X.; Wang, X.; Zhang, T.; et al. Organic tetrabutylammonium cation intercalation to heal inorganic $CsPbI_3$ perovskite. *Angew. Chem. Int. Ed.* **2021**, *60*, 12351-5. DOI PubMed
156. Kim, H.; Lee, S. U.; Lee, D. Y.; et al. Optimal interfacial engineering with different length of alkylammonium halide for efficient and stable perovskite solar cells. *Adv. Energy. Mater.* **2019**, *9*, 1902740. DOI
157. Zhang, T.; Dar, M. I.; Li, G.; et al. Bication lead iodide 2D perovskite component to stabilize inorganic α-$CsPbI_3$ perovskite phase for high-efficiency solar cells. *Sci. Adv.* **2017**, *3*, e1700841. DOI PubMed PMC
158. Zhang, S.; Zhang, L.; Tian, Q.; et al. Spontaneous construction of multidimensional heterostructure enables enhanced hole extraction for inorganic perovskite solar cells to exceed 20% efficiency. *Adv. Energy. Mater.* **2021**, *12*, 2103007. DOI
159. Li, J.; Shan, X.; Bade, S. G. R.; et al. Single-layer halide perovskite light-emitting diodes with sub-band gap turn-on voltage and high brightness. *J. Phys. Chem. Lett.* **2016**, *7*, 4059-66. DOI
160. Chen, H.; Zhang, T.; Wang, F.; et al. Efficient stabilization and passivation for low-temperature-processed γ-$CsPbI_3$ solar cells. *ACS. Appl. Mater. Interfaces.* **2021**, *13*, 18784-91. DOI
161. Zhang, L.; Guo, T.; Liu, B.; et al. Intermediate-phase-modified crystallization for stable and efficient $CsPbI_3$ perovskite solar cells. *ACS. Appl. Mater. Interfaces.* **2022**, *14*, 19614-22. DOI
162. Du, Y.; Tian, Q.; Chang, X.; et al. Ionic liquid treatment for highest-efficiency ambient printed stable all-inorganic $CsPbI_3$ perovskite solar cells. *Adv. Mater.* **2022**, *34*, 2106750. DOI PubMed
163. Wang, Q.; Zheng, X.; Deng, Y.; Zhao, J.; Chen, Z.; Huang, J. Stabilizing the α-Phase of $CsPbI_3$ perovskite by sulfobetaine zwitterions in one-step spin-coating films. *Joule* **2017**, *1*, 371-82. DOI
164. Wu, T.; Wang, Y.; Dai, Z.; et al. Efficient and stable $CsPbI_3$ solar cells via regulating lattice distortion with surface organic terminal groups. *Adv. Mater.* **2019**, *31*, 1900605. DOI
165. Zhang, J.; Fang, Y.; Zhao, W.; Han, R.; Wen, J.; Liu, S. Molten-salt-assisted $CsPbI_3$ perovskite crystallization for nearly 20%-efficiency solar cells. *Adv. Mater.* **2021**, *33*, e2103770. DOI PubMed
166. Wang, Y.; Liu, X.; Zhang, T.; et al. The role of dimethylammonium iodide in $CsPbI_3$ perovskite fabrication: additive or dopant? *Angew. Chem. Int. Ed.* **2019**, *58*, 16691-6. DOI PubMed
167. Meng, H.; Shao, Z.; Wang, L.; et al. Chemical composition and phase evolution in DMAI-derived inorganic perovskite solar cells. *ACS. Energy. Lett.* **2019**, *5*, 263-70. DOI
168. Sun, X.; Shao, Z.; Li, Z.; et al. Highly efficient $CsPbI_3/Cs_{1-x}DMA_xPbI_3$ bulk heterojunction perovskite solar cell. *Joule* **2022**, *6*, 850-60. DOI
169. Cui, Y.; Shi, J.; Meng, F.; et al. A versatile molten-salt induction strategy to achieve efficient $CsPbI_3$ perovskite solar cells with a high open-circuit voltage >1.2 V. *Adv. Mater.* **2022**, *34*, e2205028. DOI PubMed
170. Yu, G. Jiang, K.-J.; Gu, W.-M.; et al. Vacuum-assisted thermal annealing of $CsPbI_3$ for highly stable and efficient inorganic perovskite solar cells. *Angew. Chem. Int. Ed.* **2022**, *61*, e202203778. DOI PubMed

171. Eperon, G. E.; Paternò, G. M.; Sutton, R. J.; et al. Inorganic caesium lead iodide perovskite solar cells. *J. Mater. Chem. A.* **2015**, *3*, 19688-95. DOI
172. Luo, P.; Xia, W.; Zhou, S.; et al. Solvent engineering for ambient-air-processed, phase-stable $CsPbI_3$ in perovskite solar cells. *J. Phys. Chem. Lett.* **2016**, *7*, 3603-8. DOI PubMed
173. Wang, K.; Jin, Z.; Liang, L.; et al. All-inorganic cesium lead iodide perovskite solar cells with stabilized efficiency beyond 15%. *Nat. Commun.* **2018**, *9*, 4544. DOI PubMed PMC
174. Pei, Y.; Liu, Y.; Li, F.; Bai, S.; Jian, X.; Liu, M. Unveiling property of hydrolysis-derived $DMAPbI_3$ for perovskite devices: composition engineering, defect mitigation, and stability optimization. *iScience* **2019**, *15*, 165-72. DOI PubMed PMC
175. Yang, F.; Ruan, Y.; Li, S.; et al. A flowing liquid phase induces the crystallization processes of cesium lead triiodide for 21.85%-efficiency solar cells and low-energy loss. *Energy. Environ. Sci.* **2025**, *18*, 1232-40. DOI
176. Wang, G.Q.; Wang, D.S.; Bi, J.Y.; et al. Tailoring the crystallization of $CsPbIBr_2$ perovskite via phenylthiourea for stable and efficient perovskite solar cells. *Acta Phys. Sin.* **2023**, *72*, 158801. DOI
177. Zhu, J.; He, B.; Gong, Z.; et al. Grain enlargement and defect passivation with melamine additives for high efficiency and stable $CsPbBr_3$ perovskite solar cells. *ChemSusChem* **2020**, *13*, 1834-43. DOI PubMed
178. Wang, X.; Ran, X.; Liu, X.; et al. Tailoring component interaction for air-processed efficient and stable all-inorganic perovskite photovoltaic. *Angew. Chem. Int. Ed.* **2020**, *59*, 13354-61. DOI PubMed
179. Zhao, H.; Fu, Y.; Li, Z.; et al. High-efficiency and thermal/moisture stable $CsPbI_{2.84}Br_{0.16}$ inorganic perovskite solar cells enabled by a multifunctional cesium trimethylacetate organic additive. *J. Mater. Chem. A.* **2021**, *9*, 4922-32. DOI
180. Zhang, Z.; Ji, R.; Hofstetter, Y. J.; et al. Towards low-temperature processing of efficient γ-$CsPbI_3$ perovskite solar cells. *J. Mater. Chem. A.* **2023**, *11*, 16115-26. DOI
181. Ling, Y.; Tian, Y.; Wang, X.; et al. Enhanced optical and electrical properties of polymer-assisted all-inorganic perovskites for light-emitting diodes. *Adv. Mater.* **2016**, *28*, 8983-9. DOI PubMed
182. Zhang, L.; Mei, L.; Wang, K.; et al. Advances in the application of perovskite materials. *Nano-Micro. Lett.* **2023**, *15*, 177. DOI PubMed PMC
183. Tan, J.; Tong, S.; Zhou, T.; Lin, J.; Liu, Y. Research and development of modification strategies based on all inorganic perovskite solar cells. *Nano. Energy.* **2025**, *138*, 110815. DOI
184. Sosa Acosta, A.; Angel, F. A. Thermally evaporated $CsPbBr_3$ for green perovskite light-emitting diodes: challenges and perspectives. *ACS. Appl. Electron. Mater.* **2025**, *7*, 1361-76. DOI
185. Li, X.; Gao, X.; Zhang, X.; et al. Lead-free halide perovskites for light emission: recent advances and perspectives. *Adv. Sci.* **2021**, *8*, 2003334. DOI PubMed PMC
186. Luo, M.; Wei, C.; Wu, Y.; Lei, W.; Zhang, X.; Zeng, H. All-inorganic perovskite film photodetectors with tailored deposition techniques and component engineering. *J. Mater. Chem. C.* **2024**, *12*, 11675-711. DOI
187. Xu, R.; Chin, X. Y.; White, L. R. W.; Mhaisalkar, S. G.; Bruno, A. Transforming near-infrared photodetectors with perovskites: materials, strategies, and future outlook. *Energy. Fuels.* **2025**, *39*, 10744-67. DOI
188. Chen, R.; Wang, C.; Zhang, X.; et al. Recent advancements in all-inorganic and organic-inorganic hybrid metal halide materials for photocatalytic CO_2 reduction reaction. *Front. Energy.* **2025**, *19*, 450-70. DOI
189. De Giorgi, M. L.; Perulli, A.; Yantara, N.; Boix, P. P.; Anni, M. Amplified spontaneous emission properties of solution processed $CsPbBr_3$ perovskite thin films. *J. Phys. Chem. C.* **2017**, *121*, 14772-8. DOI
190. Zhang, L.; Yuan, F.; Dong, H.; et al. One-step co-evaporation of all-inorganic perovskite thin films with room-temperature ultralow amplified spontaneous emission threshold and air stability. *ACS. Appl. Mater. Interfaces.* **2018**, *10*, 40661-71. DOI PubMed
191. Li, G.; Cheng, S.; Chen, X.; et al. Erbium-induced boost in self-trapped exciton emission of double perovskites for highly sensitive multimodal and multiplexed optical thermography. *Adv. Funct. Mater.* **2024**, *34*, 2403073. DOI
192. Chang, X.; Fang, J.; Fan, Y.; et al. Printable $CsPbI_3$ perovskite solar cells with PCE of 19% via an additive strategy. *Adv. Mater.* **2020**, *32*, 2001243. DOI PubMed
193. Xiao, H.; Zuo, C.; Liu, F.; Ding, L. Drop-coating produces efficient $CsPbI_2Br$ solar cells. *J. Semicond.* **2021**, *42*, 050502. DOI
194. Zhang, L.; Chen, S.; Zeng, J.; et al. Inkjet-printing controlled phase evolution boosts the efficiency of hole transport material free and carbon-based $CsPbBr_3$ perovskite solar cells exceeding 9%. *Energy. Environ. Mater.* **2023**, *7*, e12543. DOI
195. Ma, Q.; Huang, S.; Chen, S.; et al. The effect of stoichiometry on the stability of inorganic cesium lead mixed-halide perovskites solar cells. *J. Phys. Chem. C.* **2017**, *121*, 19642-9. DOI
196. Li, Y.; Xu, J.; Shen, H.; et al. Morphology, luminescence and the gravity sedimentation effect of flexible and highly stable $CsPbBr_3$ nanocrystal patterns by the inkjet printing method. *CrystEngComm* **2024**, *26*, 5046-58. DOI

197. Parida, B.; Singh, A.; Kalathil Soopy, A. K.; et al. Recent developments in upscalable printing techniques for perovskite solar cells. *Adv. Sci.* **2022**, *9*, 2200308. DOI PubMed PMC
198. Liu, C.; Yang, Y.; Zhang, C.; et al. Tailoring C_{60} for efficient inorganic $CsPbI_2Br$ perovskite solar cells and modules. *Adv. Mater.* **2020**, *32*, e1907361. DOI PubMed
199. Chen, R.; Hui, Y.; Wu, B.; et al. Moisture-tolerant and high-quality α-$CsPbI_3$ films for efficient and stable perovskite solar modules. *J. Mater. Chem. A.* **2020**, *8*, 9597-606. DOI
200. Mali, S. S.; Patil, J. V.; Shao, J.; et al. Phase-heterojunction all-inorganic perovskite solar cells surpassing 21.5% efficiency. *Nat. Energy.* **2023**, *8*, 989-1001. DOI
201. Yu, X.; Li, J.; Mo, Y.; et al. "Coffee ring" controlment in spray prepared >19% efficiency $Cs_{0.19}FA_{0.81}PbI_{2.5}Br_{0.5}$ perovskite solar cells. *J. Energy. Chem.* **2022**, *67*, 201-8. DOI
202. Zhang, Q.; Liu, H.; Tan, X.; et al. Suppressing "Coffee ring effect" to deposit high-quality $CsPbI_3$ perovskite films by drop casting. *Chem. Eng. J.* **2023**, *454*, 140147. DOI
203. Xiao, H.; Zuo, C.; Zhang, L.; et al. Efficient inorganic perovskite solar cells made by drop-coating in ambient air. *Nano. Energy.* **2023**, *106*, 108061. DOI
204. Tan, S.; Tan, C.; Cui, Y.; et al. Constructing an interfacial gradient heterostructure enables efficient $CsPbI_3$ perovskite solar cells and printed minimodules. *Adv. Mater.* **2023**, *35*, e2301879. DOI PubMed
205. Heo, J. H.; Zhang, F.; Xiao, C.; et al. Efficient and stable graded $CsPbI_{3-x}Br_x$ perovskite solar cells and submodules by orthogonal processable spray coating. *Joule* **2021**, *5*, 481-94. DOI
206. Heo, J. H.; Zhang, F.; Park, J. K.; et al. Surface engineering with oxidized $Ti_3C_2T_x$ MXene enables efficient and stable p-i-n-structured $CsPbI_3$ perovskite solar cells. *Joule* **2022**, *6*, 1672-88. DOI
207. Li, H.; Zhang, W. Perovskite tandem solar cells: from fundamentals to commercial deployment. *Chem. Rev.* **2020**, *120*, 9835-950. DOI PubMed
208. Wang, J.; Zhao, P.; Hu, Y.; et al. An exploration of all-inorganic perovskite/gallium arsenide tandem solar cells. *Solar. RRL.* **2021**, *5*, 2100121. DOI
209. Li, T.; Xu, J.; Lin, R.; et al. Inorganic wide-bandgap perovskite subcells with dipole bridge for all-perovskite tandems. *Nat. Energy.* **2023**, *8*, 610-20. DOI
210. Sun, Q.; Zhang, Z.; Zhang, T.; et al. Integrated 4-terminal all-inorganic perovskite tandem solar cell with open-circuit voltage exceeding 2.1 V for water splitting. *ACS. Energy. Lett.* **2022**, *7*, 4215-23. DOI
211. Wang, P.; Li, W.; Sandberg, O. J.; et al. Tuning of the interconnecting layer for monolithic perovskite/organic tandem solar cells with record efficiency exceeding 21%. *Nano. Lett.* **2021**, *21*, 7845-54. DOI
212. Lang, K.; Xu, J.; Zhang, X.; et al. Ionic liquid-driven intermediate phase engineering for surface-reconstruction of $CsPbI_2$ Br toward high-efficiency perovskite/organic tandem solar cells. *Adv. Funct. Mater.* **2026**, *36*, e75071. DOI
213. Han, Y.; Fu, J.; Ren, Z.; et al. Inorganic perovskite/organic tandem solar cells with 25.1% certified efficiency via bottom contact modulation. *Nat. Energy.* **2025**, *10*, 513-25. DOI
214. Huang, J.; Han, Y.; Ren, Z.; et al. Perovskite-organic tandem solar cells with superior reverse-bias stability. *Nat. Mater.* **2026**, *Epub ahead of print*. DOI PubMed
215. Wu, H.; Sun, Z.; Li, H.; et al. Review of all-inorganic perovskites and their tandem solar cells with crystalline silicon. *Energy. Mater. Devices.* **2024**, *2*, 9370045. DOI
216. Yu, Z.; Leilaeioun, M.; Holman, Z. Selecting tandem partners for silicon solar cells. *Nat. Energy.* **2016**, *1*, 16137. DOI
217. Wang, S.; Wang, P.; Chen, B.; et al. Suppressed recombination for monolithic inorganic perovskite/silicon tandem solar cells with an approximate efficiency of 23%. *eScience* **2022**, *2*, 339-46. DOI
218. Wang, S.; Wang, P.; Shi, B.; et al. Inorganic perovskite surface reconfiguration for stable inverted solar cells with 20.38% efficiency and its application in tandem devices. *Adv. Mater.* **2023**, *35*, 2300581. DOI
219. Wang, Z.; Liu, X.; Lin, Y.; et al. Hot-substrate deposition of all-inorganic perovskite films for low-temperature processed high-efficiency solar cells. *J. Mater. Chem. A.* **2019**, *7*, 2773-9. DOI
220. Rao, H.; Ye, S.; Gu, F.; et al. Morphology controlling of all-inorganic perovskite at low temperature for efficient rigid and flexible solar cells. *Adv. Energy. Mater.* **2018**, *8*, 1800758. DOI
221. Jiang, H.; Feng, J.; Zhao, H.; et al. Low temperature fabrication for high performance flexible $CsPbI_2Br$ perovskite solar cells. *Adv. Sci.* **2018**, *5*, 1801117. DOI
222. Liu, D.; Yang, C.; Bates, M.; Lunt, R. R. Room temperature processing of inorganic perovskite films to enable flexible solar cells. *iScience* **2018**, *6*, 272-9. DOI PubMed PMC

223. Yang, X.; Yang, H.; Hu, X.; et al. Low-temperature interfacial engineering for flexible $CsPbI_2Br$ perovskite solar cells with high performance beyond 15%. *J. Mater. Chem. A.* **2020**, *8*, 5308-14. DOI
224. Hu, L.; Zhao, Q.; Huang, S.; et al. Flexible and efficient perovskite quantum dot solar cells via hybrid interfacial architecture. *Nat. Commun.* **2021**, *12*, 466. DOI PubMed PMC
225. Liu, H.; Zhang, Z.; Han, H.; et al. CaF_2 nanoparticle-induced γ-$CsPbI_{2.81}Br_{0.19}$ heterogeneous crystallization for high-efficiency flexible all-inorganic perovskite solar cells. *J. Phys. Chem. Lett.* **2024**, *15*, 10514-24. DOI PubMed
226. Beal, R. E.; Slotcavage, D. J.; Leijtens, T.; et al. Cesium lead halide perovskites with improved stability for tandem solar cells. *J. Phys. Chem. Lett.* **2016**, *7*, 746-51. DOI
227. Draguta, S.; Sharia, O.; Yoon, S. J.; et al. Rationalizing the light-induced phase separation of mixed halide organic-inorganic perovskites. *Nat. Commun.* **2017**, *8*, 200. DOI PubMed PMC
228. Duong, T.; Mulmudi, H. K.; Wu, Y.; et al. Light and electrically induced phase segregation and its impact on the stability of quadruple cation high bandgap perovskite solar cells. *ACS. Appl. Mater. Interfaces.* **2017**, *9*, 26859-66. DOI PubMed
229. Xiao, Z.; Zhao, L.; Tran, N. L.; et al. Mixed-halide perovskites with stabilized bandgaps. *Nano. Lett.* **2017**, *17*, 6863-9. DOI PubMed
230. Balakrishna, R. G.; Kobosko, S. M.; Kamat, P. V. Mixed halide perovskite solar cells. Consequence of iodide treatment on phase segregation recovery. *ACS. Energy. Lett.* **2018**, *3*, 2267-72. DOI
231. Chen, W.; Mao, W.; Bach, U.; Jia, B.; Wen, X. Tracking dynamic phase segregation in mixed-halide perovskite single crystals under two-photon scanning laser illumination. *Small. Methods.* **2019**, *3*, 1900273. DOI
232. Belisle, R. A.; Bush, K. A.; Bertoluzzi, L.; Gold-parker, A.; Toney, M. F.; Mcgehee, M. D. Impact of surfaces on photoinduced halide segregation in mixed-halide perovskites. *ACS. Energy. Lett.* **2018**, *3*, 2694-700. DOI
233. Abdi-jalebi, M.; Andaji-garmaroudi, Z.; Cacovich, S.; et al. Maximizing and stabilizing luminescence from halide perovskites with potassium passivation. *Nature* **2018**, *555*, 497-501. DOI PubMed
234. Yang, J.; Song, Y.; Yao, J.; et al. Potassium bromide surface passivation on $CsPbI_{3-x}Br_x$ nanocrystals for efficient and stable pure red perovskite light-emitting diodes. *J. Am. Chem. Soc.* **2020**, *142*, 2956-67. DOI PubMed
235. Yang, Z.; Rajagopal, A.; Jo, S. B.; et al. Stabilized wide bandgap perovskite solar cells by tin substitution. *Nano. Lett.* **2016**, *16*, 7739-47. DOI PubMed
236. Li, N.; Zhu, Z.; Li, J.; Jen, A. K. Y.; Wang, L. Inorganic $CsPb_{1-x}Sn_xIBr_2$ for efficient wide-bandgap perovskite solar cells. *Adv. Energy. Mater.* **2018**, *8*, 1800525. DOI
237. Wang, Z.; Wang, Y.; Nie, Z.; et al. Laser induced ion migration in all-inorganic mixed halide perovskite micro-platelets. *Nanoscale. Adv.* **2019**, *1*, 4459-65. DOI PubMed PMC
238. Yang, Z.; Rajagopal, A.; Jen, A. K. Y. Ideal bandgap organic-inorganic hybrid perovskite solar cells. *Adv. Mater.* **2017**, *29*, 1704418. DOI PubMed
239. Yao, X.; He, B.; Zhu, J.; et al. Tailoring type-II all-in-one buried interface for 1.635V-voltage, all-inorganic $CsPbBr_3$ perovskite solar cells. *Nano. Energy.* **2022**, *96*, 107138. DOI
240. Duan, C.; Zou, F.; Wen, Q.; et al. A bifunctional carbazide additive for durable $CsSnI_3$ perovskite solar cells. *Adv. Mater.* **2023**, *35*, e2300503. DOI PubMed
241. Wang, K.; Yue, S.; Li, T.; et al. Synergistic in situ hydrolysis polymerization for efficient air-fabricated inorganic perovskite solar cells. *SusMat* **2025**, *5*, e70032. DOI